PSEUDO-RANDOM SINGLE PHOTON COUNTING FOR TIME-RESOLVED OPTICAL MEASUREMENTS

ZHANG QIANG

(B. Eng, Xi'an Jiaotong University, P. R. China)

A THESIS SUBMITTED
FOR THE DEGREE OF DOCTOR OF
PHYLOSOPHY
DIVISION OF BIOENGINEERING
NATIONAL UNIVERSITY OF SINGAPORE

2011

Dedication

To my family and friends, for their care, love and support.

Acknowledgements

I could not have finished my PhD study without the help and support of many people. First of all, I would like to express my sincere gratitude to my advisor, Dr. Chen Nanguang for all the support he has provided with me. His constant encouragement, patient guidance and constructive advice have been valuable throughout my PhD research, and will always be my treasure in my future life.

Dr. Chen has been providing me with the big picture and encouraging me to be a confident and independent researcher. His marvelous breadth of scientific knowledge and way of analytical thinking have inspired me to develop my own scientific insights. His scrupulous and conscientious working style has directed me to strive for academic integrity. He has guided me on how to deal with tough problems even they seem to be insoluble. He has taught me how to deliver presentations with clarity and how to write scientific papers. Every time I have questions or problems, he is always there with such patience explaining the key concepts and helping figure out the problems in a systematic manner. Sometimes he even demonstrates the experimental issues in person.

Besides my supervisor, I am also grateful to the other two principal investigators in the Optical Bioimaging Lab: Professor Colin Sheppard and Dr. Huang Zhiwei. I thank them for their helpful advice throughout my research and I appreciate their efforts in building up the wonderful working atmosphere in the lab.

I would like to acknowledge my group members as they helped me a lot in my research. Dr. Gao Guangjun, I thank him as he provided me with kind encouragement and technical help in optical alignments during the last few months of my research. I am also grateful to my colleague and friend Chen Ling, who dedicated herself to the image reconstruction work which was an important part of our collaborated work and publication. In my last year of PhD research, Wang Wenduo has been working with me on the in vivo human blood glucose study. She helped me a lot in the recruitment and measurements of human subjects in this study. Her initiative in this study and constructive suggestions are greatly appreciated. I won't forget Hsien Li Quan, Dr. Tian Haiting and Soon Hock Wei, who have been working with me during my 2nd and/or 3rd year. I thank them for their contribution to my project.

I also want to thank my friends and other colleagues in the Optical Bioimaging Lab. I have been really fortunate to be able to work with such a wonderful ensemble of people. As the first PhD student under Dr. Chen, Dr. Liu Linbo has provided me with so much refreshing encouragement and kind guidance, a truly brother of mine. Dr. Wong Chee Howe and Dr. Mo Weirong, who were also under Dr. Chen, provided me with numerous technical help. Without the help of these 3 senior groupmates, I would not even survive in my 1st year. I am also grateful to Chong Shau Poh, Ali Hasnain, Mehta Kalpesh Badreshkumar and Dr. Sun Meixiu, who are my current/former groupmates, for the productive discussions and their helpful suggestions. Besides my groupmates, I am so lucky to have a bunch of friends in the Optical Bioimaging Lab: Kou Shanshan is a considerate, generous and warm-hearted person, who has offered me valuable advice and enlightened me when I was low; Mo Jianhua, Lu Fake, Shao Xiaozhuo and Lin Kan, who are all fantastic persons, have been helping me a lot throughout my study; Dr. Yuen Clement, Dr. Li Hao and Dr. Zheng Wei, who were former/current colleagues in the Optical Bioimaging Lab, I thank them for their kind help in my study. It is my great pleasure to acknowledge all of them who have at some extent enriched both academic and personal aspects of my life.

I have obtained a lot of help from my friends in the Supramolecular Biomaterials Lab, especially from Ping Yuan and Liu Chengde. It is so nice of them to sometimes go out of their way to help me with great patience. Without them, my experiments wouldn’t be as smooth as it has been.

Mr. Ni Jianhuang who is a mechanical engineer has provided me with invaluable advice and design & fabrication service which constitutes essential parts of my experimental setup. Thanks to his work which is almost always in a prompt and accurate fashion.

Lastly, I’d like to thank all my family and friends who have shaped who I am now. My greatest thank goes to my Mom, who was, is and will always be my firm back. Her constant care, love and support mean a lot in building up my self-esteem and confidence. I would also like to take the opportunity to thank my other family members: my granny, aunts and cousins, for their love and support. My friends Yang Xiao, Wang Wei, Yingfang, Wang Qiang, Gao Xia, Siqi, Yanyan, Hanzi, Zhang Peng and Khanh were there with me during the toughest days, kept offering me with hope restoring encouragement and care. I

want to give my special thanks to Xiaobo, who has been the one to raise me up, the one to keep inspiring me with her optimism, tolerance and love for life. I will always be indebted to Jidan, who has been by my side for the past 2 and half years. My gratitude for her care, tolerance and love and my prayers for her happiness will never end.

“Those who would give up essential liberty to purchase a little temporary safety deserve neither liberty nor safety,” I would like to end the acknowledgement with this one of my favorite quotes, as a reminder for my future career and life.

Contents

Abstract

In time-resolved optical instrumentations, an ultra-short light pulse is used to illuminate the subject of interest, while the time-dependent transmittance, reflectance and fluorescence in response to the illumination are measured. By taking advantage of the high information content of the time-dependent measurements, researchers can uncover the structure and dynamics of the sample under investigation.

Currently, time-correlated single photon counting (TCSPC) is the most widely used method for acquiring the temporal profile of the response to an ultra-short light pulse. Despite its various striking benefits, TCSPC has a problem of limited photon count rate which usually results in low data acquisition speed. In addition, a typical TCSPC system would require a pulsed laser, which is of high cost and renders the system bulky. In this thesis, a new time-resolved optical measurement method termed as pseudo-random single photon counting (PRSPC) was developed to provide a valuable alternative approach of conducting time-resolved optical measurements. The new method combines the spread spectrum time-resolved (SSTR) method with single photon counting. A pseudo-random bit sequence is used to modulate a continuous wave laser diode, while single photon counting is used to build up the optical signal in response to the modulated excitation. Periodic cross-correlation is performed to obtain the temporal profile of the subject of interest. Compared with conventional TCSPC, PRSPC enjoys many advantages such as low cost and high count rate without compromising much on the sensitivity and time-

resolution. The PRSPC system reported in this thesis can reach a temporal resolution of 130 ps and a photon count rate as high as 3 Mcps (counts per second). In addition, considering that the PRSPC system uses a continuous wave laser instead of a pulsed laser, it has high potential to be easily integrated into a portable device.

To explore the potential application of the PRSPC method, the PRSPC system was integrated into a time-resolved diffuse optical imaging (DOI) experimental system for phantom studies. The lipofundin phantom based experiments demonstrated that the PRSPC system is capable of fast acquisition of temporal profile of diffuse photons and has high potential in time-domain DOI systems.

The PRSPC system was also integrated into a time-resolved spectroscopic system for human blood glucose testing studies. By analyzing the temporal profiles of the photons diffused through human finger, the connection between the human blood glucose level and the blood transparency in the near infrared was explored. The preliminary results from this study may shed light on the topic of non-invasive human blood sugar monitoring and further the development of truly non-invasive blood sugar testing devices.

List of Tables

List of Figures

List of Symbols and Acronyms

D	photon diffusion coefficient
g	isotropic factor
ltr	mean free path
μ_s’	reduced scattering coefficient
μ_a	absorption coefficient
$\Phi(r; t)$	photon fluence rate
S(r; t)	isotropic light source
τ	fluorescence lifetime
Δn	refractive index mismatch

ADC	analog-to-digital converter
APD	avalanche photodiode
CFD	constant fraction discriminator
CP	calculated parameter
cps	counts per second
CT	x-ray computed tomography
CW	continuous-wave
DOI	diffuse optical imaging
DOT	diffuse optical tomography
FCS	fluorescence correlation spectroscopy
FD	frequency-domain
FLIM	fluorescence lifetime imaging microscopy
PS	parametric slope
FRET	fluorescence resonance energy transfer
FWHM	full width at half maximum
GUI	graphic user interface

Hb	deoxygenated hemoglobin
HbO_2	oxygenated hemoglobin
IRF	instrument response function
MCP	micro-channel plate
MM	multimode
MRI	magnetic resonance imaging
NI	non-invasive
NIR	near-infrared
OCT	optical coherent tomography
PAS	photoaccoustic spectroscopy
PDDL	programmable digital delay line
PMT	photomultiplier tube
PRBS	pseudo-random bit sequence
PRSPC	pseudo-random single photon counting
RBC	red blood cell
SNR	signal to noise ratio
SPC	single photon counting
SSTR	spread spectrum time-resolved method
TAC	time-to-amplitude converter
TCSPC	time-correlated single photon counting
TD	time-domain
TPSF	temporal point spread function
TR	time-resolved
TTS	transit time spread
VISA	virtual instrument software architecture

Chapter 1 Introduction

With the rapidly increasing use of light in biomedical research, time-resolved optical techniques have been widely explored in the past few decades. By utilizing ultra-short light pulse based time-dependent measurements, researchers can study dynamic processes in biological or human tissue, materials or chemical compounds that occur on time scales as short as 10^{-14} seconds. Time-resolved optical spectroscopy, fluorescence lifetime imaging microscopy (FLIM) and time-resolved optical mammography are among the various applications of time-resolved techniques.

1.1 Motivation

In time-resolved optical techniques, the subject under investigation is illuminated by an ultra-short light pulse, while the temporal profile of the response is measured. This measurement is fundamental and crucial for the follow-up imaging process or spectroscopy analysis. Currently the most commonly used instruments are streak cameras and time-correlated single photon counting (TCSPC) systems. A streak camera operates by transforming the temporal profile of a light pulse into a spatial profile on a detector. It can reach a time resolution of down to 200 femtoseconds. TCSPC is based on the detection of single photons of a periodical light signal and the measurement of the arriving times of the individual photons. Although streak camera offers higher time resolution, TCSPC is the preferred and more widely used method because of its better dynamic range and temporal linearity. Thus a majority of the reported time-resolved studies utilized the TCSPC method.

Nevertheless, TCSPC also has its disadvantages. A typical TCSPC system requires a pulsed laser, which is of high cost and renders the system bulky. In addition, the measurement time of TCSPC tends to be long due to the low photon count rate caused by the pile-up error intrinsic in TCSPC. For example, if TCSPC is used for FLIM, then for each pixel it needs about 1ms to collect enough photons. For an image size of 512×512 pixels, it will take more than 250 seconds to acquire one frame. For real-time or near-real-time imaging, a faster time-resolved method is desirable.

1.2 Objective

The objective of this research was to develop a new time-resolved optical measurement method which was termed pseudo-random single photon counting (PRSPC). The PRSPC method aimed for faster data acquisition, system portability and comparable performance as to the conventional TCSPC. In this new approach, the light beam is modulated by a train of high speed pseudo-random bit sequence (PRBS). The modulated light transports through phantom or tissue. A single photon counting (SPC) detector is used to collect photon pulses and form the histogram standing for the optical signals emitted from the sample. This histogram is then demodulated by cross-correlating with the original PRBS. In this way the time-resolved signals, i.e., the temporal profile of the sample can be retrieved. The performance of the system would be assessed by conducting phantom experiments. To investigate the potential of this method in time-resolved techniques, time-resolved diffuse optical imaging and time-resolved spectroscopic experiments would be conducted. The specific objectives of this research were to:

- Validate the PRSPC method theoretically by conducting computer based simulations and experimentally by building up a prototype PRSPC system and conducting phantom based experiments.

- Design, implement, optimize and evaluate a high speed PRSPC system. Emphasis was placed on achieving optimal temporal resolution and fast data acquisition speed.

- Explore the potential of the PRSPC method in time-resolved diffuse optical imaging system. Phantom based diffuse optical imaging experiments would be conducted in which the PRSPC method is used for acquisition of temporal point spread function (TPSF) of diffuse photons.

- Explore the potential of the PRSPC method in time-resolved spectroscopic applications. Human blood glucose testing would be studied. By analyzing the temporal profiles of the photons diffused through human finger, the PRSPC method would be used to investigate the connection between the blood glucose level and the blood transparency in the near infrared.

The results of this study should provide a valuable alternative method in time resolved optical measurements, since the pseudo-random single photon counting method should offer a faster data acquisition speed without sacrificing much on key performances such as temporal resolution and sensitivity. In addition, the PRSPC system is expected to be compact and readily available to be integrated into a comprehensive optical system, e.g., a time-resolved diffuse optical imaging system. The method should be very competitive in terms of performance to cost ratio.

The time-resolved diffuse optical imaging and time-resolved spectroscopic experiments using PRSPC should demonstrate the potential of the method in time-resolved techniques. The approach of combining occlusion spectroscopy with the PRSPC method may shed light on the topic of non-invasive human blood glucose monitoring and further the development of truly non-invasive blood glucose testing devices.

1.3 Organization of this thesis

This thesis is composed of three parts: the first part reviews the time-resolved measurement methods and their applications in time-resolved optical systems. This part forms the base of the whole study. The second part describes the novel PRSPC measurement method, including theoretical and experimental validation and detailed descriptions of a high speed implementation. The last part explores two potential applications of the new method. Specifically, each part is organized as follows:

Part I:

Chapter 2 is an introductory chapter. It briefly reviews two time-resolved optical measurement methods that have been frequently employed by researchers nowadays. The more popular TCSPC method is given more detailed illustration. Despite the striking advantages, the disadvantages of TCSPC are pointed out to be its low data acquisition speed and bulky system. In addition, a recently developed spread spectrum time-resolved (SSTR) method which aims for faster data acquisition is also introduced in this chapter. The high temporal resolution and sensitivity achievable with the single photon counting technique and the high data acquisition speed afforded by SSTR inspired us to combine the two methods together and develop a novel method that offers merits of both.

Part II:

Chapter 3 is about the validation of the PRSPC method. It consists of the mathematical theory and validation of the PRSPC method, which includes the simulation work and experimental work involved in building up of a prototype PRSPC system.

Chapter 4 systematically describes the working principle of a high speed implementation of the PRSPC method, including the system working flow block diagram and configurations of key components. The characterization of system performance is also included in this chapter.

Part III:

In Chapter 5, the PRSPC system is integrated into a time-resolved diffuse optical imaging system while liquid phantom experiments are conducted to demonstrate the potential of the PRSPC system. The detailed image reconstruction process is beyond the scope of this study and only the basic procedure is included.

In Chapter 6, the PRSPC system is integrated into a time-resolved spectroscopic system to explore its potential application. In vivo human blood glucose testing experiments are conducted using the system. Qualitative relationship between the experimental data and the glucose meter readings is demonstrated. The quantitative relationship, however, would demand for extensive follow-up clinical research and thus is recommended for future studies.

Chapter 7 summarizes the entire thesis and proposes possible directions for future studies.

Chapter 2 Time-resolved optical techniques and instrumentations

Time-resolved techniques are important in optical instrumentation. Measurements of time-dependent transmittance, reflectance and fluorescence in response to illumination by an ultra-short light pulse always contain rich information which researchers can use to retrieve important properties of the sample under investigation [1-10]. Two good examples are time-resolved diffuse optical tomography and fluorescence lifetime imaging microscopy. Time-resolved diffuse optical tomography measures temporal point spread functions (TPSF) which can be used for quantitative reconstruction of distributions of scattering and absorption coefficients [11-16]. Fluorescence lifetime imaging measures the mean fluorescence lifetime of a fluorophore at each spatially resolvable element of a microscope image [2,3]. This chapter will briefly review several time-resolved techniques to showcase their general concepts and significance.

In time-resolved techniques, the temporal profiles of the response to an ultra-short light pulse are most commonly measured with either a streak camera [17,18] or a time-correlated single photon counting (TCSPC) system [19-46]. In this chapter, the principles of the two methods will be discussed. A recently developed method termed as spread spectrum time-resolved (SSTR) optical measurement method, which forms the foundation of the method developed in this study, will also be introduced.

2.1 Time-resolved optical techniques

2.1.1 Time-resolved diffuse optical tomography

Diffuse optical tomography (DOT) is a non-invasive technique used to measure the optical properties of physiological tissue. This technique offers several unique advantages including nonionizing radiation, relatively inexpensive instrumentation and the potential for functional imaging of tissue optical properties. These advantages are generally not available with established imaging modalities, such as ultrasound, x-ray computed tomography (CT) and magnetic resonance imaging (MRI). Although the spatial resolution is limited when compared with other imaging modalities, DOT provides access to a variety of physiological parameters that are not accessible by other techniques, including sub-second imaging of hemodynamics and other fast-changing processes. Up to date, DOT has generated a lot of scientific interests and has been applied in various applications including breast cancer imaging [47-55,100-107], brain functional imaging [56], muscle functional studies [57-59], photodynamic therapy [60,61] and radiation therapy monitoring [62].

2.1.1.1 The NIR window

The use of light for diagnostics of deep tissue presents great challenges. Electromagnetic radiation in the UV and visible wavelength range is strongly absorbed by biological species in tissue. Due to absorption by chromophores in tissue, such as water, oxygenated hemoglobin (HbO_2) and deoxygenated hemoglobin (Hb), the intensity of UV and visible light decreases rapidly as it penetrates deep inside tissue. Thus, the traditional methodologies typically require optically thin samples.

To reach tissue located centimeters below the surface, light penetration must be large within tissue. Fortunately, a spectral window exists in the near-infrared (NIR) from 700 nm to 900 nm (Figure 2.1), wherein photon transport is dominated by scattering rather than absorption. The absorption of hemoglobin and water is small in the near-infrared, but elastic scattering from organelles and other microscopic interfaces is large. The penetration depth thus can reach 5 cm or more.

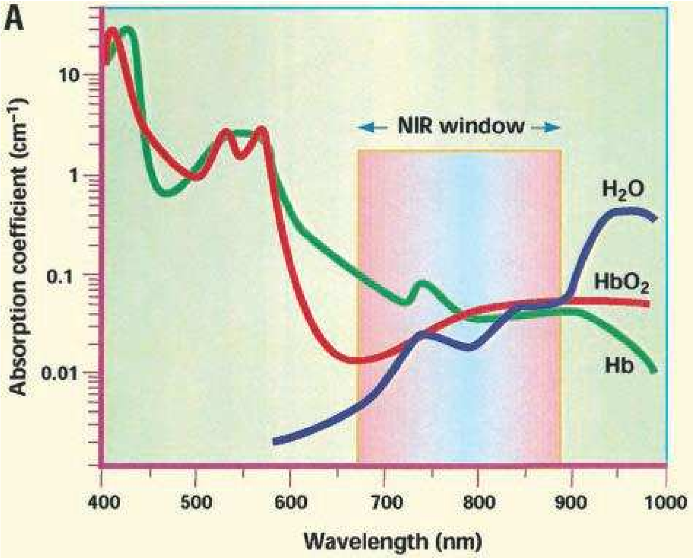

Figure 2.1 Absorption spectrum in the red and near infrared

The weak absorption and strong scattering are precisely the conditions required for application of the diffusion model. Using this physical model it is possible to quantitatively separate tissue scattering from tissue absorption, and to accurately incorporate the influence of boundaries, such as the air-tissue interface, into the transport theory. The diffusion approximation also provides a tractable basis for tomographic approaches to image reconstruction using highly scattered light.

2.1.1.2 NIR Light transport in tissue

In diffuse optical imaging and spectroscopy applications in biomedical system, a collimated NIR beam is used to illuminate the biological tissue from the surface, while some photons will be reflected back into the air and the remaining will go through the tissue. These photons may be absorbed, keep propagating in its original direction, or be elastic-scattered and change propagating direction.

The interaction between photon and the biological cell membrane changes the photon propagation direction unpredictably. However, the behavior of vast photons passing through a scattering tissue largely follows an underlying statistic.

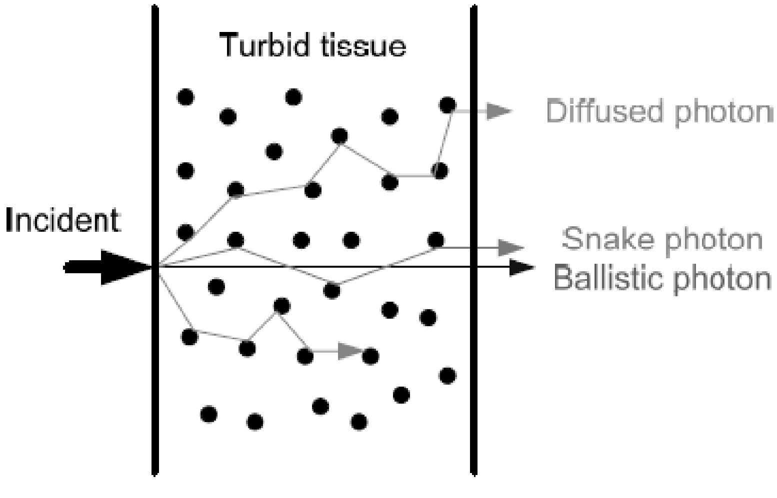

Figure 2.2 Schematic diagram of various photon trajectories in tissue medium

As shown in Figure 2.2, the photon propagation tracks within the tissue can be classified into 3 components [100], including:

- Ballistic component

The forward scattered and the coherent photons constitute the group of ballistic photons. These photons travel straight along the direction of the incident laser beam.

- “Snake” component

The group of “snake” photons is composed of photons that undergo a few elastic scattering events when travelling through the tissue.

- Diffuse component

The majority of the incident photons undergo multiple scattering events within tissue. These photons constitute the diffuse component. This component carries valuable information regarding the scattering properties of the tissue.

2.1.1.3 The diffusion equation

The propagation of photons through a turbid medium is described by the Boltzman transport equation [63]. Although solutions of the Boltzman equation are computationally intensive, fortunately, it can be well approximated by the photon diffusion equation for most DOT applications wherein the following two presumptions are satisfied [64]:

- The scattering effect is dominant over the absorption effect.

- The distance between source and detector is sufficiently large.

The photon diffusion equation which is essentially an energy conservation equation has the following form:

$$\nabla \cdot (D(\mathbf{r})\nabla\Phi(\mathbf{r},t)) - \mu_a(\mathbf{r})\Phi(\mathbf{r},t) - \frac{1}{v}\frac{\partial\Phi(\mathbf{r},t)}{\partial t} = -S(\mathbf{r},t).$$

$$D = \frac{1}{3(1-g)\mu_s} = \frac{1}{3\mu_{st}} = \frac{l_{tr}}{3},$$

where D is the photon diffusion coefficient [65,66], g is the isotropic factor, l_{tr} is the mean free path, $\mu_s{}'=\mu_{st}$ is the reduced scattering coefficient, and μ_a is the absorption coefficient. Φ(r; t) is the photon fluence rate and S(r; t) is the isotropic light source.

In DOT, the optical properties commonly in interest are absorption coefficient (μ_a) and reduced scattering coefficients ($\mu_s{}'$). Chromophores in human tissue at different concentration have corresponding characteristic absorption spectra and scattering spectra. Concentrations of these chromophores in normal and cancerous tissues will be different. Quantifying these differences among chromophores could help to understand the physiological status of the human tissue.

2.1.1.4 The time-domain measurement scheme

Three types of measuring systems capable of detecting faint diffused light are used widely in the community: continuous-wave (CW), frequency-domain (FD) and time-domain (TD). The frequency-domain methods employ harmonically modulated photon density waves and phase-resolved detection, which measures the phase shift of the photon density waves [67-80]. The continuous-wave approach may also be classified as frequency-domain since it employs steady-state illumination which is corresponding to the zero frequency [81,82]. The time-domain or time-resolved (TR) system utilizes ultra-short pulsed lasers and detects transient light signals with picosecond time resolution [83,123-126].

In time-resolved methods, the entire temporal response (rather than merely the ballistic photons) is examined and employed to fit to a model based on the time-dependent diffusion equation. By making use of the full time spectra, scattered photons are also accounted for, thus the absorption and scattering properties can be more accurately reconstructed. Therefore, the time-domain DOT can discriminate smaller variations of the optical properties inside tissue by image reconstruction [123,124]. In addition, time-domain methods that are capable of rapid averaging of the transient signals can achieve signal-to-noise ratios (SNR) competitive with frequency-domain methods.

Due to the lowest measurement rate among the three measurement types, the most likely application areas for the TR DOT would be in imaging of the long-term changes in tissue physiology and pathology, such as breast cancer diagnosis [84-86] and neonatal brain oxygenation monitoring [87,88]. In all these applications, the image showing the anatomical information about the tissue is necessary for identification and localization of cancerous, bleeding or hematomas tissue.

Figure 2.3 [89] illustrates the schematic diagram of the time-domain diffuse optical tomography. An ultra-short light pulse is used to illuminate the tissue.

After transmitting through or reflecting back from the tissue, the photons will become spatially and temporally dispersed with time. The temporal profile of the dispersed photons, i.e. the temporal point spread function can be measured by a time-correlated single photon counting module or a streak camera, which will be introduced in sub-section 2.2.

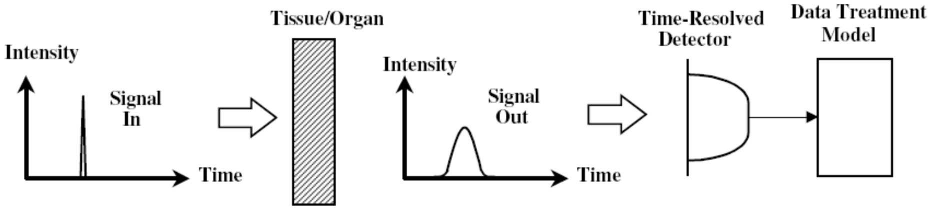

Figure 2.3 Schematic diagram of the time-resolved DOT technique

2.1.2 Fluorescence lifetime imaging microscopy

Fluorescence lifetime imaging microscopy (FLIM) measures the mean fluorescence lifetime of a chromophore at each spatially resolvable element of a microscope image [2,3]. By taking advantage of the high information content of the time-dependent fluorescence decays, one can uncover the structure and dynamics of macromolecules. The lifetime measurement is dependent on excited-state reactions such as fluorescence resonance energy transfer (FRET) rather than probe concentration or light path length. This property allows exploration into the interior of cells for the molecular environment of labeled macromolecules. Image contrast formed based on fluorescence lifetime measurements enables observation of biochemical reactions at each microscopically resolvable location within the cell.

2.1.2.1 Fluorescence light

The phenomenon of fluorescence is widely utilized for research in bioscience. Fluorescence is suited for observing the dynamics of molecules in cells since it is non-invasive and can be detected with high sensitivity and signal specificity. In addition, the multitude of spectroscopic properties of fluorescence can be further exploited to obtain information on the whereabouts of labeled macromolecules on the micron scale as well as on the immediate molecular environment. Fluorescent labeling of proteins is required in the study of protein reactions in in-vivo signal transduction. Generally, it can be achieved by either chemical modification of a purified protein [90], or site-specific covalent labeling of recombinant protein molecules [91] or the construction of fusion proteins with one of the green fluorescent protein mutants [92]. The labeled proteins are then expressed or microinjected into cells and microspectroscopy applied to image the site of cellular reactions.

2.1.2.2 Fluorescence lifetimes

In time-resolved fluorescence measurement, a fluorophore is excited by a short pulse of light and the resulting fluorescence response is recorded. The rate of photoemission is proportional to the number of excited fluorophores. The fluorescence intensity decay *I(t)* is typically a multiexponential function:

$$I(t) = \sum_i a_i \cdot e^{-t/\tau_i} ,$$

where τ_i are lifetimes and a_i are the corresponding amplitudes. For a mixture of fluorophores, the decay times will be those of the individual fluorophores and the amplitudes will be related to the intensity and concentration of each species.

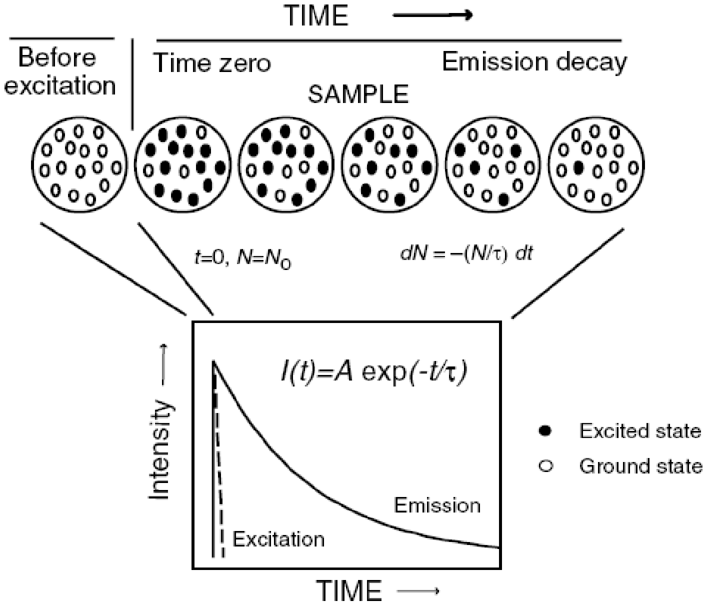

Figure 2.4 Concept of the fluorescence lifetime.
N=number of molecules in the excited state; τ =emission lifetime [93].

Several time domain approaches have been used to measure fluorescence decays, including single-shot experiments when the full fluorescence decay is acquired from a single-excitation pulse with streak cameras, repetitive stroboscopic sampling and the widely used time-correlated single photon counting. A number of these methods have been adopted for fluorescence lifetime imaging in a wide variety of instrumental implementations.

2.1.2.3 Fluorescence lifetime imaging microscopy

The concept of fluorescence lifetime imaging microscopy is illustrated in Figure 2.5.

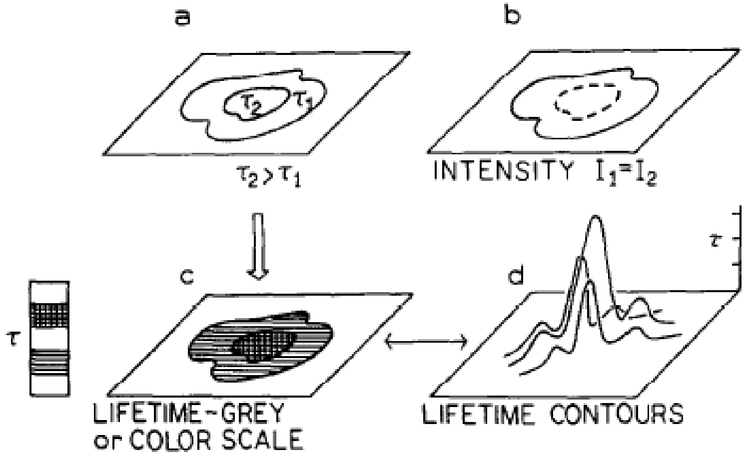

Figure 2.5 Concept of fluorescence lifetime imaging [2]

Assuming we have a sample that is composed of two regions, each with an equal intensity of the steady-state fluorescence (Figure 2.5b). In Figure 2.5a, it is also assumed that the central region of the object has a longer lifetime (τ_2) than that of the outer region (τ_1). The longer lifetime in the central region could be caused by the presence of a chemical species or other environmental factors. The intensities of the central and outer regions could be equally caused by dye exclusion or other mechanisms. It is clear that merely observing the intensity image (Figure 2.5b) will not reveal the different environments in the two regions. However, if the different lifetimes in these regions can be measured and the decay times are used to form image contrast, the distinct environments can be detected. The image contrast can be presented either on a gray or color scale (Figure 2.5c) or as a 3D surface in which the height represents the local decay times (Figure 2.5d).

Time-resolved fluorescence imaging microscopy can now be used to image biochemical reactions in living cells. By providing an extra spectroscopic dimension on top of the steady-state fluorescence image, the nanosecond fluorescence lifetimes enable the resolution of parameters reporting on the activation state(s) of proteins or protein systems in situ without disrupting the cellular architecture. FLIM is important in fundamental cell-biology research but also in the pharmacological and medical industry. The parallel readout, non-invasiveness and independence of fluorescence lifetimes on probe concentration, make FLIM an ideal detection platform for ultra-high-throughput screening of drug libraries on live cells. Moreover, FLIM is a powerful medical diagnostic tool as it can help monitor the earlier functional state of proteins implicated in the pathology of diseased tissue. The current development of FLIM using multiple harmonic modulation frequencies (mfFLIM) will enable the simultaneous detection of several tagged biomolecules and make their interactions resolvable. This, in combination with novel optical-sectioning methods [94] and improved modulatable detectors, may further enhance the spatio-temporal resolution and therefore improve the evaluation of cellar level biochemical reactivity.

2.2 Instrumentations for time-resolved measurements

2.2.1 Streak camera

A streak camera is an instrument which can be used for measuring the temporal variation of a light pulse’s intensity [95]. As shown in Figure 2.6, the light beam, which contains rich temporal information, enters the streak camera through a slit. At the photocathode, the photons are converted into electrons whose number is proportional to the intensity of the light beam. The electrons are accelerated by a pair of accelerating electrodes and then bombarded against a phosphor screen. Before hitting the phosphor screen, the electrons pass through a pair of sweep electrodes, where a high voltage synchronized to the incident light is applied. The electrons will be vertically deflected by the high voltage and the timing of the electrons will decide the deflection angle. The deflected electrons will then enter the micro-channel plate (MCP), where they are multiplied thousands of times, and then converted back to light at the phosphor screen. On the phosphor screen, the vertical direction serves as the time axis, while the horizontal direction corresponds to the horizontal location of the incident light beam. The brightness of a phosphor image is proportionate to the intensity of the corresponding incident light pulse. In this way, the phosphor images can be used to characterize the temporal profiles of the incident light pulses.

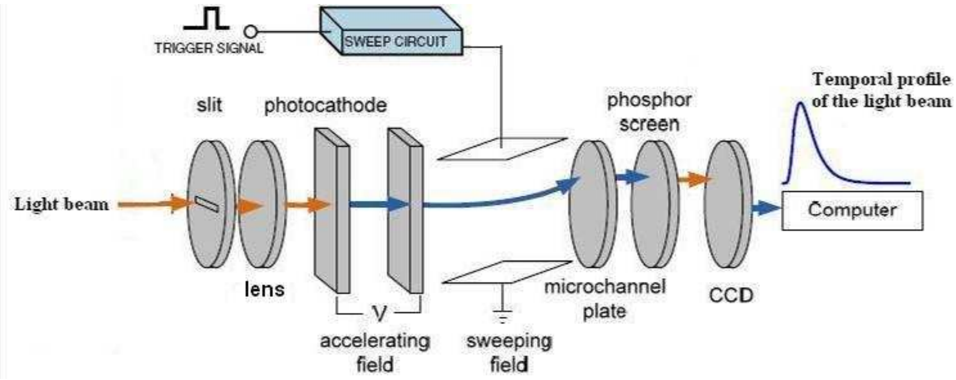

Figure 2.6 Operating principle of streak camera

Streak camera offers excellent temporal resolution (down to the ps scale), ultra-high sensitivity (single photoelectron can be detected) and fast data acquisition (real time). However, one limitation is high system cost. The Hamamatsu Streak Camera C5680 series would cost around $200k. In addition, the dynamic range of streak camera is normally limited (approximately 10^4). Finally, the temporal nonlinearity is inherently subject to the ramp voltage. For these reasons the streak camera has limited applications in time resolved optical measurements.

2.2.2 Time-correlated single photon counting

Time-correlated single photon counting is a technique to record low level light signals with picosecond time resolution. It has become increasingly popular among time-resolved optical measurement methods because of better dynamic range and temporal linearity. Typical applications include ultra-fast recording of optical waveforms, fluorescence lifetime measurements [29-33], detection and identification of single molecules [34-36], fluorescence correlation spectroscopy (FCS) [37], DNA sequencing [38,39], optical tomography [22,25,28,40-44] and fluorescence resonance energy transfer (FRET) [45,46]. The method has some striking benefits, such as ultra-high time resolution, ultra-high sensitivity which is down to the single photon level, high dynamic range which is limited by photon statistics only, high linearity, excellent signal-to-noise ratio and high gain stability.

2.2.2.1 Basic principle

Time-correlated single photon counting is based on the detection of single photons of a periodical light signal, the measurement of the detection times of the individual photons and the reconstruction of the waveform from the individual time measurements [20,96]. The method makes use of the fact that for low level, high repetition rate signals the light intensity is usually so low that the probability to detect one photon in one signal period is much less than one. Therefore, the detection of several photons can be neglected and the principle shown in Figure 2.7 is used.

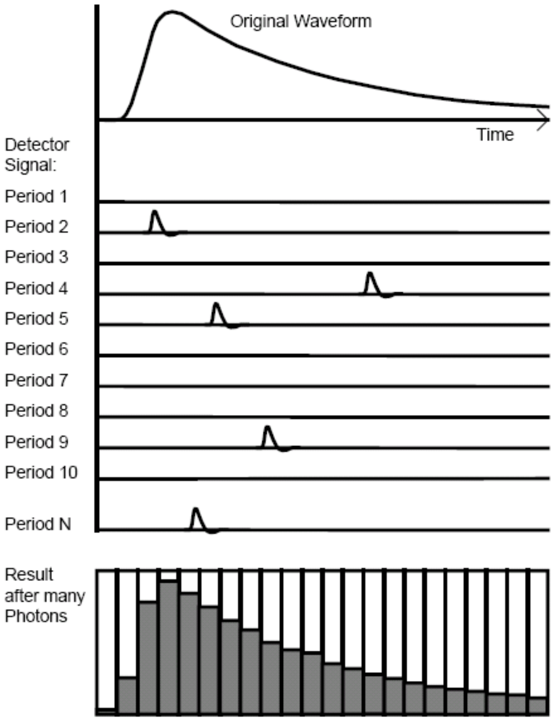

Figure 2.7 TCSPC measurement principle [97]

The detector signal consists of a train of many signal periods without photons, while other signal periods contain one photon pulse. When a photon is detected, the time of the corresponding detector pulse is measured. The events are collected in the memory by adding a ‘1’ in a memory location with an address proportional to the detection time. After many photons, in the memory the histogram of the detection times, i.e. the waveform of the optical pulse builds up.

2.2.2.2 The classic TCSPC architecture

The architecture of a classic TCSPC device [20,98] is shown in Figure 2.8.

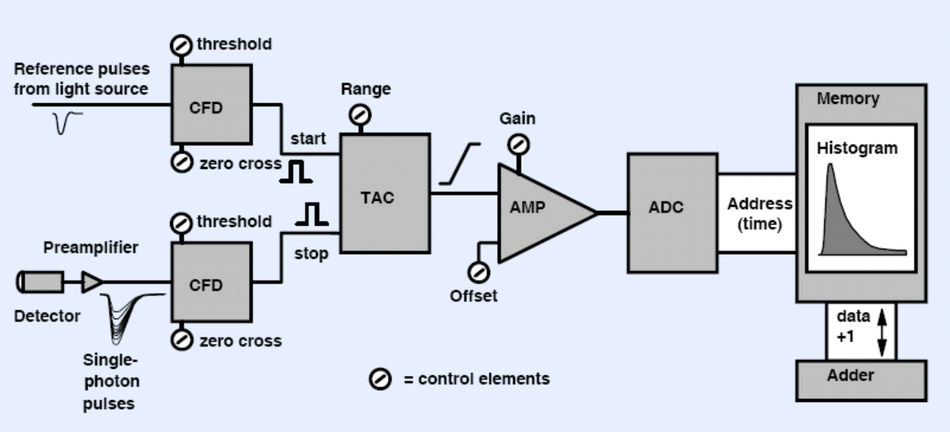

Figure 2.8 Architecture of a classic TCSPC device

The detector, usually a photomultiplier tube (PMT), and also can be an avalanche photodiode, generates electrical pulses for individual photons of the repetitive light signal. The electrical pulses, which are detected by a fast discriminator, have a considerable amplitude jitter due to the random amplification mechanism in the detector. A constant fraction discriminator (CFD) is used to trigger on the PMT pulses. The CFD triggers at a constant fraction of the pulse amplitude, avoiding pulse-height induced timing jitter.

A second CFD is used to obtain a timing reference pulse which is usually generated by a photodiode or a PMT. In this case, the reference pulses may also have some amplitude fluctuation or drift. The use of a CFD in the reference channel prevents the introduction of timing jitter or timing drift.

The output pulses of the CFDs enter a time-to-amplitude converter (TAC), which outputs a signal whose amplitude is proportional to the time between the start and the stop pulse. The TAC output voltage is sent through a biased amplifier, which has a variable gain and a variable offset. It is used to select a smaller time window within the full-scale conversion range of the TAC.

The amplified TAC signal is fed to an analog-to-digital converter (ADC). When a photon is detected, the ADC output word addresses a memory location which corresponds to the detection time of the photon. By repeating the process, as more and more photons are collected and addressed, the photon distribution, which is proportional to the original repetitive light signal, can be built up.

2.2.2.3 System performance highlights

As aforementioned, TCSPC has many striking benefits among which are the ultra-high time resolution and sensitivity.

1） Ultra-high time resolution:

The TCSPC method differs from methods involving analog signal processing as the time resolution is not limited by the width of the detector impulse response but rather the transit time spread (TTS) of the single photon pulses in the detector and the timing jitter in the electronic system [97]. The time resolution can be up to 10 times better than the half width of the detector impulse response. Some typical values for different detector types are given in Table 2.1.

Table 2.1Time resolutions of TCSPC systems featuring different detector types

Detector type		Time resolution
Conventional photomultipliers	Standard types	0.6~1 ns
	High speed (XP2020)	0.35 ns
Avalanche photodiodes		60~500 ps
Hamamatsu TO8 photomultipliers	R5600, R5783	140~220 ps
Micro channel plate photomultipliers	Hamamatsu R3809	25~30 ps

2) Ultra-high sensitivity:

The sensitivity of the TCSPC method is limited mainly by the dark count rate of the detector. Defining the sensitivity as the intensity at which the signal is equal to the noise of the dark signal, the following equation [97] applies:

$$S = \frac{(R_d * N / T)^{1/2}}{Q},$$

where R_d is the dark count rate, N is the number of time channels, Q is the quantum efficiency of the detector and T is the overall measurement time. Typical values (uncooled PMT with multi-alkali cathode) are R_d =300/s, N=256, Q=0.1 and T=100s. This yields a sensitivity of S=280 photons/second. This value is by a factor of 10^{-15} smaller than the intensity of a typical laser (10^{18} photons/second). Thus, when a sample is excited by the laser and the emitted light is measured, the emission is still detectable for a conversion efficiency of 10^{-15}.

2.2.2.4 Drawbacks

In spite of the remarkable performances of TCSPC mentioned above, it has certain disadvantages. Most of all, the principle of TCSPC requires that no more than one photon is detected in each cycle, otherwise the pile-up error will occur [97]. This limitation causes a big problem in the data acquisition speed. The maximal count rate is limited by the repetition rate of laser pulses, the processing speed of electronic devices and the time span of the impulse response. A typical photon count rate is below 1Mcps (counts per second), though the state-of-the-art TCSPC modules can achieve a count rate as high as 10M cps by correcting the pile-up error. The low count rate is a bottle neck to achieve faster acquisition speed. In some applications, when multiple detection channels are necessary, the measurement speed will be critical. For example, F. E. W. Schmidt et al. reported a 32-channel time-resolved instrument, which needs 10-20 minutes for a complete scan [99]. It is worthwhile to mention that far more photon counts are needed for accurate measurement of the intensity of early-arriving photons [100-102].

Besides, a high standard optical system is needed for TCSPC to achieve high detection efficiency and reduce typical error sources, such as signal distortion by reflections, pulse dispersion, instability or wavelength-dependence of the instrument response function (IRF) and leakage of excitation light or daylight. Thus a typical TCSPC optical system involves a detector of high quantum efficiency, a strong picosecond or femtosecond pulse laser and also high quality optical components. This kind of system is of high cost, and also lack portability.

2.2.3 Spread spectrum time-resolved optical measurement method

To achieve a higher measurement speed, the spread spectrum time-resolved optical measurement method that borrows ideas from spread spectrum communications was developed [103-105]. Its implementations in time-domain diffusive optical tomography have also been reported [106,107].

2.2.3.1 Basic Principle

The basic principle of this method is simple and straightforward. It is well known that a spread spectrum communication system possesses many desirable properties, such as selective addressing capability, low error rate, and interference rejection [108, 109]. A broadband pseudo-random bit sequence has only a weak cross correlation with other codes and an auto-correlation function that is analogous to a delta function (Figure 2.9). Consequently, a receiving system can pick up the correct code sequence, addressing it from environmental noise and interference, and is able to distinguish the same sequence that arrives at different times from multiple paths.

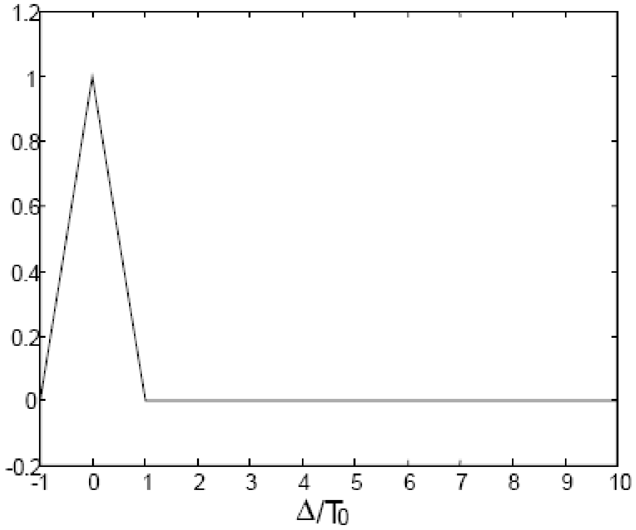

Figure 2.9 Auto-correlation of a PRBS

We denote *I(t)* as the time-dependent response of a sample to the excitation of an ultra short pulse. A light source continuously modulated with a PRBS is used to illuminate the sample. So the detected signal is proportional to the convolution of the impulse response with the excitation sequence:

$$R(t) = AI(t) * (P(t)+1)$$

where *A* is a constant representing the system gain and *P(t)* is an N-bit long PRBS with binary values +1 and -1. It has a circular auto-correlation function similar to a delta function:

$$g(\tau) = \langle P(t)P(t-\tau)\rangle$$

$$= \begin{cases} 1, \tau / T_0 = 0 \\ -1/N, \tau / T_0 = \pm 1, \pm 2, \ldots \end{cases},$$

where τ is the time delay and T_o is the bit period. By correlating the ac component of *R(t)* with *P(t)* we will have

$$f(t) = \langle (R(t') - \langle R(t') \rangle) P(t'-t) \rangle = AI(t) * g(t),$$

which is proportional to the original time spectrum *I(t)* except a slight temporal spread determined by the bit period T_0. Thus the original impulse response can be retrieved.

2.2.3.2 System architecture

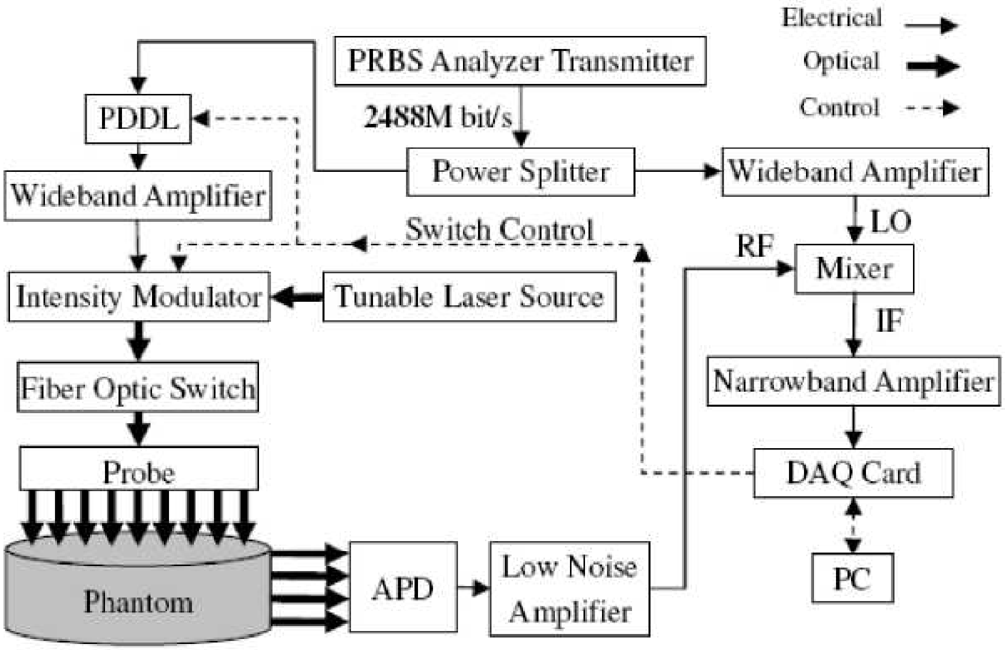

Figure 2.10 Schematic of a time-resolved diffusive optical tomography system based on SSTR

Figure 2.10 illustrates the schematic of a recently reported time-resolved DOT system based on SSTR [106]. A network analyzer transmitter continuously generates a 511-bit long PRBS at a bit rate of 2488 Mbps. A three-port wide band power splitter splits the PRBS signal into two branches of the same power. One is used for laser modulation and the other is for demodulation. The demodulation PRBS signal is further split to feed four detection channels, each of which involves a broad band amplifier for multiplication operation. The modulated PRBS signal sequentially goes through a programmable digital delay line (PDDL), a wide band amplifier and the modulation port of an intensity modulator. The PDDL has accurate time delay control (step equal 40 ps) allowing for sufficient high temporal resolution for TPSF recording. A tunable laser source with an output power of 5 mW at 780 nm continuously feeds to the intensity modulator where it is modulated by the high speed PRBS. The modulated laser beam is multiplexed into nine independent optical fibers via a low insertion loss optical switch. These nine fibers together with four light guides are distributed on a handheld probe in a specified pattern as shown in Figure 2.11. The probe has an overall dimension of 80 mm (length) x 60 mm (width) while the diameter of the light guide is 3 mm.

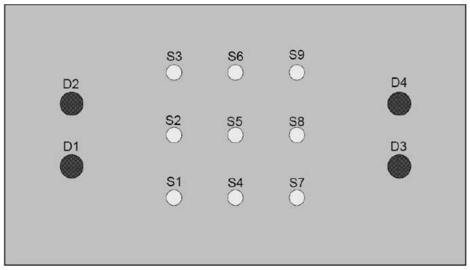

Figure 2.11 Arrangement of light sources and light guides on the handheld probe. The black circles indicate the positions of the light guides and the white circles indicate those of the light sources

The distance between light guide and light source ranges from 15 mm to 35 mm. The contacting surface of the probe is polished to increase the robustness of the reflectance signal. The reflectance signal is directed to a high speed silicon avalanche photodiode by the light guides. The low noise level amplifiers provide a total gain of +37.0 dB. Upon amplification, the signal injects into the RF port of a high performance mixer where it is demodulated with the reference PRBS arrived at the LO port. The lower frequency signal is further amplified by +60 dB. The total effective gain imposed on the electrical signal is about +90 dB taking into account the insertion loss of individual components. A 16-bit DAQ card samples the TPSF and transfers the readings to a PC. The time span of one TPSF is equal to 5.120 ns.

2.2.3.3 System performance highlights

1) Multi-channel and multi-detector capability

The DOT system which is depicted above features multiple-source (9 channels), multiple-detector (4 channels) and tunable wavelength (755-787 nm).

2) Fast data-acquisition and imaging

The data acquisition time for a complete scan for a single wavelength is less than 10 seconds. The total imaging time, inclusive of the data acquisition time and the image reconstruction time has been reported to be 10-20 seconds.

Other advantages include better signal-to-noise ratio, high sensitivity and low system cost. These, together with the fast imaging speed, provide high potential for functional imaging in clinical application.

2.2.3.4 Drawbacks

Unlike the TCSPC method, whose time resolution is determined by the transit time spread of the single photon pulses in the detector and the trigger accuracy in the electronic system, the time resolution of the SSTR method is limited by the impulse response of detectors and is about one order lower than that of

TCSPC. A time resolution around 0.5 ns has been achieved by the above system.

Chapter 3 Pseudo-random single photon counting: the method

This chapter describes a novel time-resolved optical measurement method, termed as pseudo-random single photon counting (PRSPC), which aims for high photon count rate and fast data acquisition, low system cost and portability. The theory of the PRSPC method will be illustrated. Simulation results and phantom experimental results of a prototype system will be shown to validate the method.

3.1 The PRSPC theory

In chapter 2, it has been mentioned that a spread spectrum system possesses many desirable properties, such as selective addressing capability, low error rate and interference rejection which make it extremely useful in communication industry. A fraction of a pseudo-random bit sequence with a pattern length of 1023 (2^{10}-1) is shown in Figure 3.1. It has only a weak cross-correlation with other codes, while the auto-correlation function is delta-function alike (shown in Figure 3.2 and Figure 3.3).

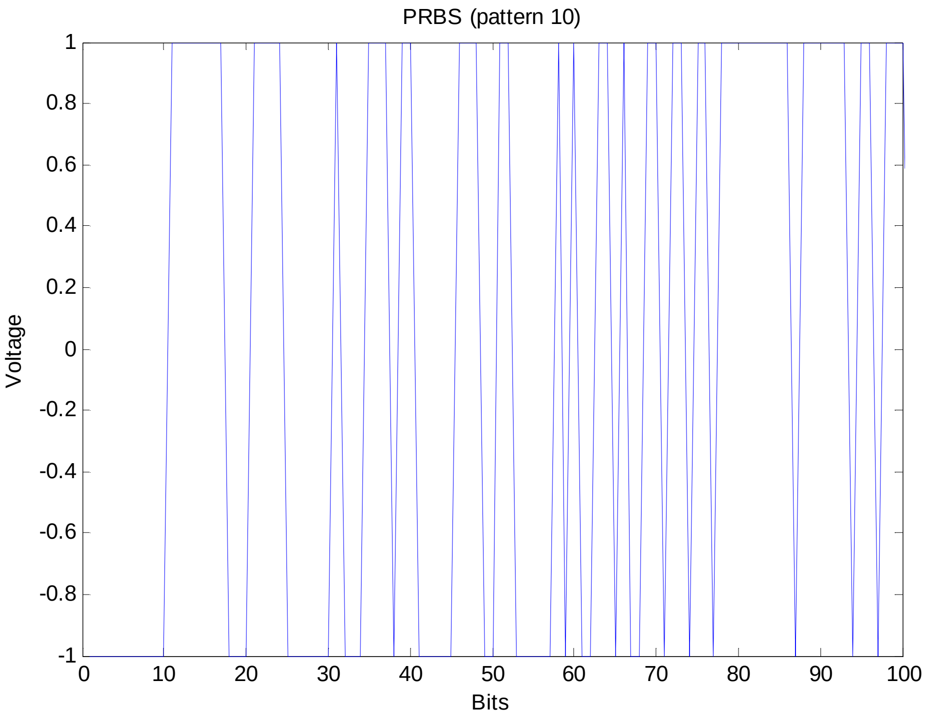

Figure 3.1 A fraction of a PRBS

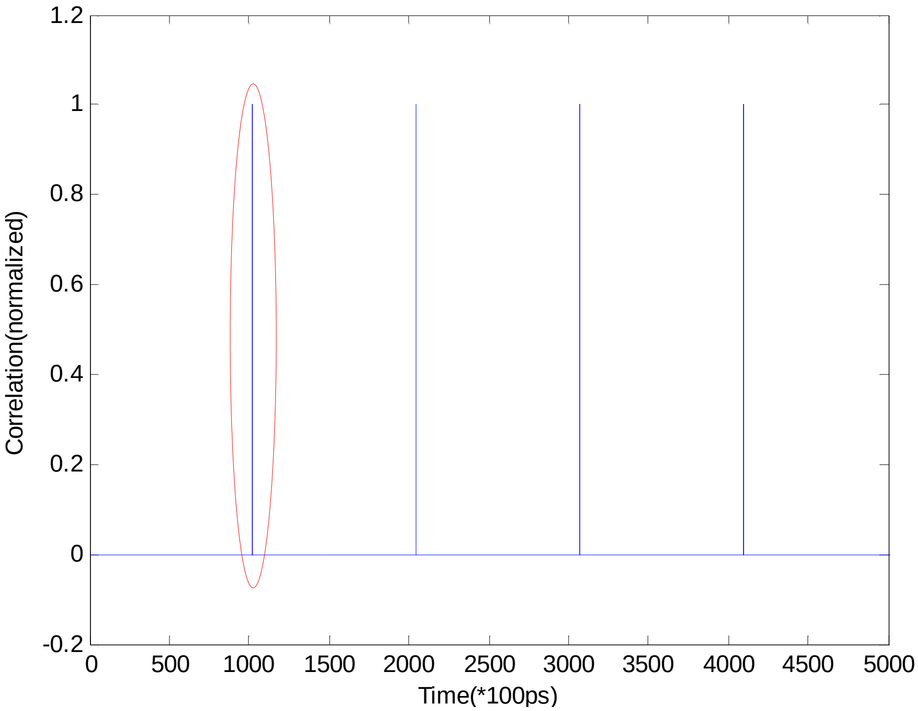

Figure 3.2. Circular correlation of a pattern 10, 10Gbps PRBS

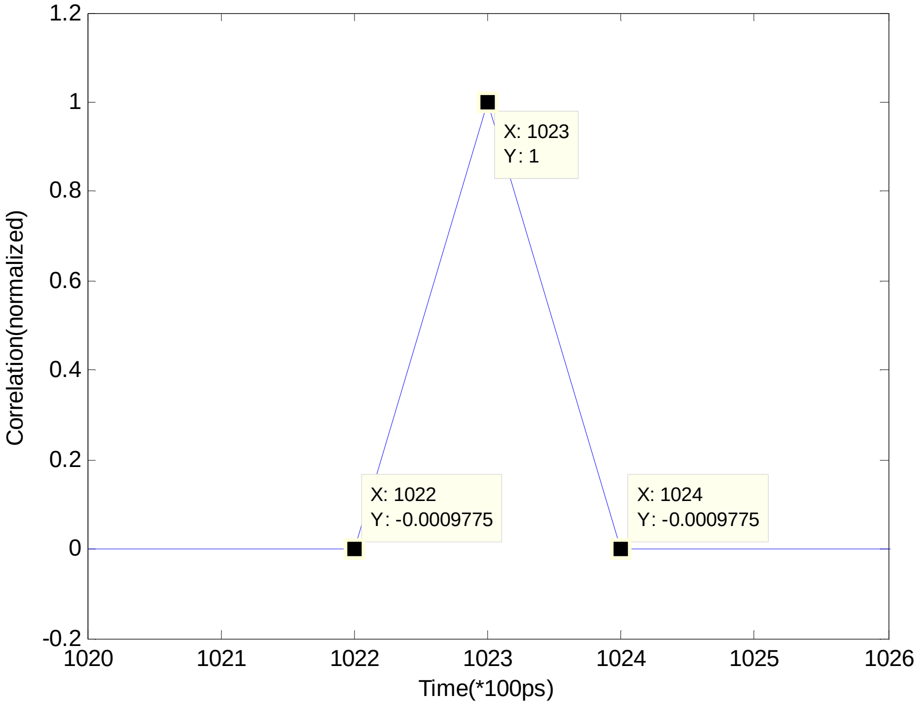

Figure 3.3 Circular correlation of a pattern 10, 10Gbps PRBS (zoom-in view of Figure 3.2)

The PRSPC method is a combination of the SSTR method and single photon counting. Recall the principle of SSTR in sub-section 2.2.3, a light source continuously modulated with a PRBS is used to illuminate the sample. The detected signal *R(t)* is proportional to the convolution of the impulse response with the excitation sequence. By correlating the ac component of *R(t)* with the PRBS sequence *P(t)*, the original impulse response *I(t)* can be retrieved. In SSTR, the detected response *R(t)* is acquired directly from the linear output of a photodetector, while the PRSPC method utilizes single photon counting to accumulate the photon numbers in various time slots. The total number of time slots is the number of bits in the excitation sequence, and the width of each slot is identical to the bit period. The excitation sequence and pulse detection are synchronized with a universal clock signal.

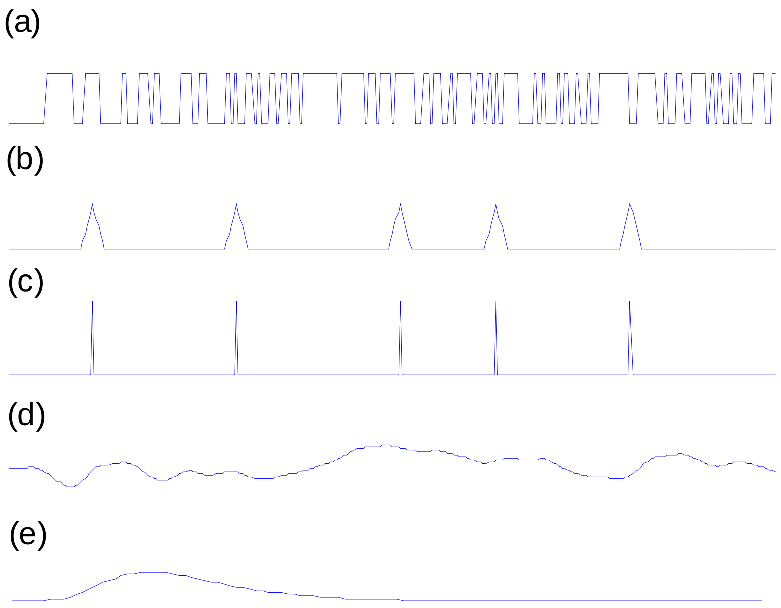

Figure 3.4 Principle of the PRSPC method

The principle of PRSPC is illustrated in Figure 3.4. Figure 3.4(a) is the output of a transmitter which is intensity modulated with a PRBS; Figure 3.4(b) is the detected pulses by the single photon detector in response to the excitation. The pulse width is determined by the type of single photon detector used. Figure 3.4(c) is the pulse sequence after post-processing, which can be performed with a circuit board or on a personal computer after digitizing. Each pulse is identified with its peak position in the time domain and has a much reduced pulse width. Then the photons are added to corresponding time slots. Repeating the process for a certain period of time, the detected signal *R(t)* builds up (Figure 3.4(d)). By cross-correlating *R(t)* with the original PRBS used for modulation, the original time spectrum *I(t)* can be retrieved (Figure 3.4 (e)).

Figure 3.5 shows an implementation scheme of the PRSPC system. The system consists of a PRBS generator, a continuous light source, a modulator, a SPC module, a receiving system and a personal computer. The modulator will modulate the input light source with the PRBS from the PRBS generator, after which, this modulated source will be directed to the subject of interest. The response signal of the sample to the excitation sequence will be captured by the SPC module, which will indicate the presence of a photon by outputting a pulse. Then, this series of randomly distributed pulses will be received by a receiving system, and later sent to a PC for data processing to build up the histogram standing for detected signal *R(t)* and finally retrieve the temporal profile of the sample.

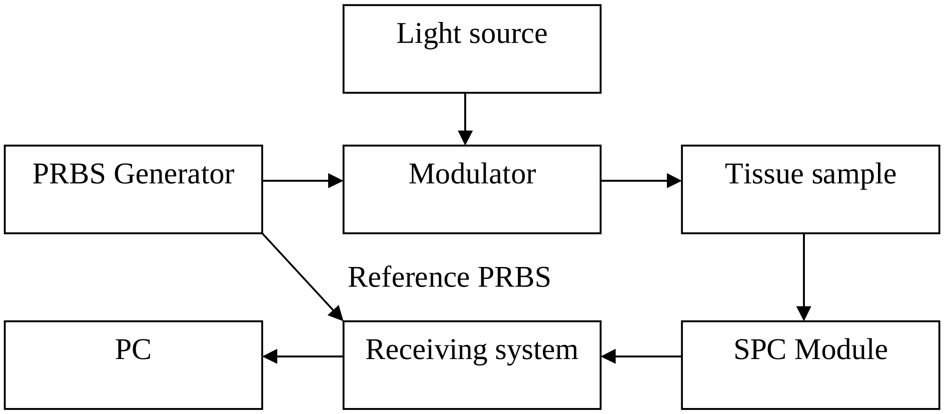

Figure 3.5 An implementation scheme of PRSPC

3.2 Validation of the PRSPC method

To validate the PRSPC method, time-resolved measurements of diffusive photon density waves using the PRSPC approach were simulated in MATLAB environment (see Appendix A.1.1). A prototype PRSPC experimental system was also built up to experimentally validate the method.

3.2.1 Simulation

As shown in Figure 3.6, the simulated PRSPC system virtually consists of a 5 Gbps pattern generator, a 10 Gbps transmitter, a single photon counting detector, a 10 Gbps digital transceiver and a computer for data processing. A 5 Gbps 1023-bit long PRBS generated by the pattern generator is used to directly modulate the transmitter to generate an optical pulse sequence. The optical fibers coupled to the transmitter and the receiver are embedded in an infinite homogeneous turbid medium and separated by $6\,cm$. The reduced scattering coefficient of the medium is $8\,cm^{-1}$, while the absorption coefficient is chosen to be $0.05\,cm^{-1}$.

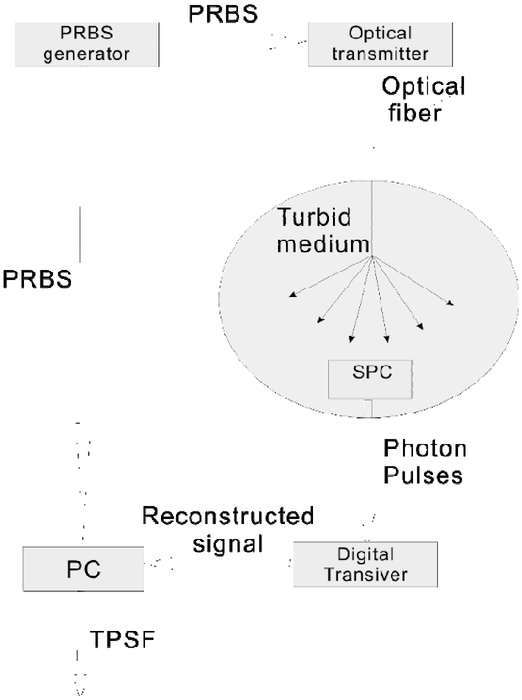

Figure 3.6 Schematic diagram of the PRSPC simulation model

The optical transmitter emits photons at a rate resulting in an average of 10 million photons arriving at the SPC detector. The SPC output signal consists of a train of randomly distributed pulses due to the detection of the individual photons. It is assumed that the single photon counting detector outputs ideal digital pulses, which are sampled by the digital transceiver at a sampling rate of 10G and the photons are added to corresponding time slots. Repeating the process for 1 second, the detected signal builds up. Finally the cross-correlation operation is used to retrieve the original time spectrum. As shown in Figure 3.7, the reconstructed TPSF with PRSPC method agrees well with the original one.

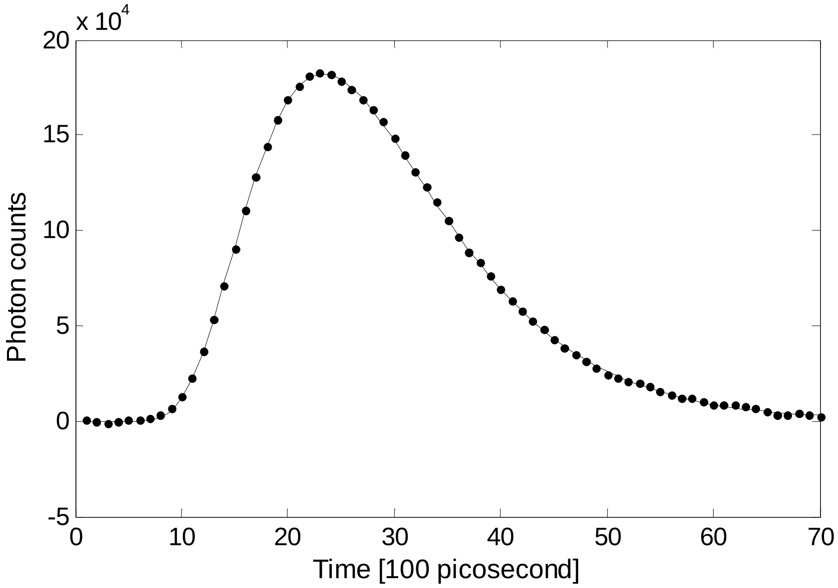

Figure 3.7 Impulse response representing the TPSF of a diffusive photon density wave. Thin curve, theoretical prediction; Black dots, reconstruction using PRSPC approach

3.2.2 Experimental validation by a prototype PRSPC system

To experimentally validate the PRSPC method, a prototype PRSPC system was built to conduct time-resolved measurements.

3.2.2.1 System setup

Figure 3.8 Configuration of the PRSPC prototype system

As shown in Figure 3.8, the PRSPC prototype system consists of:

1) A 10 Gbps pattern generator (PPG-E135, Lecroy);

The PPG-E135 is a pulse pattern generator that plugs into any available module slot in a Lecroy WaveExpert Oscilloscope mainframe. The module is capable of generating clock and data signals ranging in frequency from 50 Mb/s to 13.5 Gb/s, using an external clock. The PPG also features an internal clock, which operates in three bands centered at 2.6625 Gb/s, 5.325 Gb/s, and 10.65 Gb/s, adjustable within +/-12.5%. The differential data outputs are at a fixed level of $500\,mv_{p-p}$, and data patterns of PRBS 7, 10, 15, 23 and 31 are selectable. A variable mark/space ratio is also available.

2) A three-port wide band power splitter (ZFRSC-42, mini-circuits);

The ZFRSC-42 has a very wide band (from DC to 4200 MHz), a low insertion loss (typically 0.1 dB) and an excellent amplitude unbalance (typically 0.02 dB).

3) A 10 Gb/s 850 nm VCSEL transmitter (V-126);

The V-126 is a self-contained VCSEL source optimized for high-speed modulation up to 10 Gbps. The unit is intended to be modulated by a pattern generator for testing the performance of optoelectronic components such as photodetectors and receivers. V-126 is powered by a wall plug unit. Data input is through an SMA connector, and the optical port is an FC multimode connector. There is a control knob for choosing the optimum bias point of the VCSEL.

4) A cuvette holder (CUV-VAR Variable Pathlength Cuvette Holder, Ocean Optics);

The CUV-VAR Variable Pathlength Cuvette Holder has three functions: use its cuvette holder insert to create a 1-10 cm pathlength cuvette holder, create a 2-mm pathlength filter holder, or position its two 74-UV collimating lenses to accept a flow cell for low-concentration absorbance measurements. The included collimators are screwed into fixtures that slide along the base and can be set to create path lengths up to 10 cm.

5) A single photon counting detector (PCDMicro, SensL);

SensL’s PCDMicro is an actively quenched Geiger mode photodiode in a miniature package, requiring external voltage and giving a TTL pulse to indicate each photon detected. The PCDMicro sensing performance exceeds typical photomultiplier tubes values for key photon counting parameters such as photon detection efficiency (> 40% at blue/red wavelengths), dark count, timing-jitter (< 100ps) and after-pulsing. The miniature size of the PCDMicro is an optimal solution for applications where portability, power supply and power consumption are critical. The new quenching architecture enables state-of-the-art timing-jitter and makes it ideal for applications where timing resolution is important. The USB interface board, integrated counter, available DLLs and SensL's Integrated Environment software simplify system integration. On-board unique identifier chip allows multiple devices to be deployed and managed in large scale systems.

6) A high speed oscilloscope (54852A, Agilent) which has a 2GHz bandwidth and up to 10GHz sampling rate;

The 54852A is a 2 GHz bandwidth real-time oscilloscope with maximal 10 GS/s sampling rate available on all 4 channels simultaneously. This industry-leading sample rate produces more accurate and repeatable measurements, avoiding measurement error and signal aliasing due to under sampling of the waveform.

7) A personal computer (GX280, Dell);

8) Optical fibers and other electronic accessories.

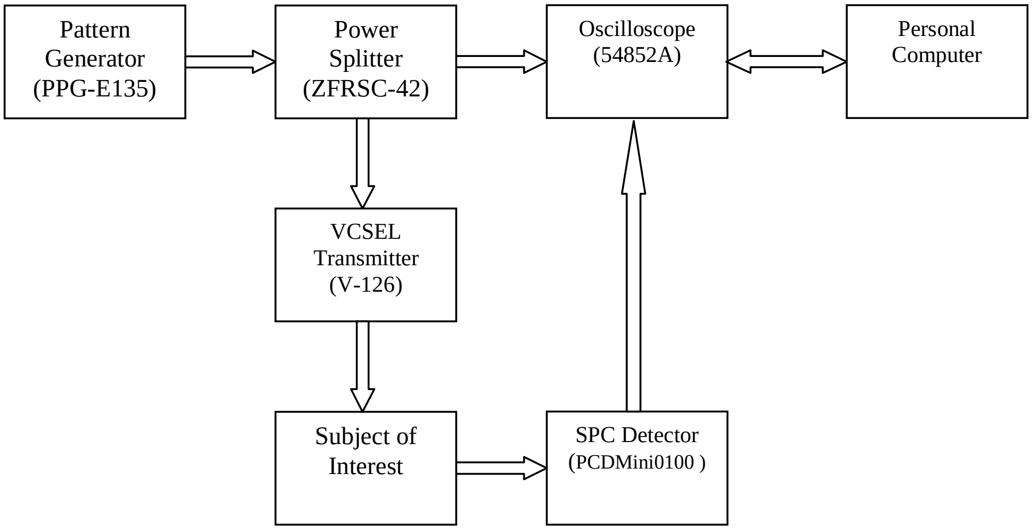

Figure 3.9 Flowchart of the PRSPC prototype

Figure 3.9 shows the flowchart of the PRSPC prototype. A 5 Gb/s 1023-bit long PRBS generated by the pattern generator is split by the power splitter into two branches: one is used to modulate the transmitter to generate an optical pulse sequence and the other is a reference PRBS. The optical fibers of the transmitter and the SPC detector are aligned in a line and separated by 5 cm. During experiments, they will be covered by a lightproof box to prevent ambient light from entering into the SPC detector. The SPC detector converts the detected optical signal into electrical signal which is acquired by the oscilloscope. The sampling rate of the oscilloscope is set to its maximal value 10 GHz, corresponding to a time resolution of 100 picoseconds. The acquired data is then transferred to the PC through local area network. The PC is responsible for further processing the received data and performing cross-correlation to retrieve the TPSF, as well as controlling the data acquisition of the oscilloscope. The interaction between the PC and the oscilloscope is realized in the MATLAB environment, which is detailed in the following paragraphs.

3.2.2.2 Remote control of oscilloscope as the receiving system

The Agilent 54852A oscilloscope is a high performance device capable of providing full 2 GHz real-time bandwidth, and can reach up to 10 GHz sampling rate. It is used as the receiving system to receive both the reference PRBS directly from the PRBS generator and the photon pulse signal from the SPC module.

The oscilloscope has a limited memory depth (the maximal value is 262144 points), while for experimental purpose, typically 1 second length data is needed, corresponding to 10^{10} points if a 10GHz sampling rate is used. To get enough data, one needs to repeatedly acquire, store, and process the data. Before we realized remote control of the receiving system, the data acquisition and post processing were tedious and laborious. Manual operation of the oscilloscope is time-consuming and even impractical considering the data length. Hence, a method to remote control the oscilloscope for the data acquisition was proposed and implemented to resolve the problem.

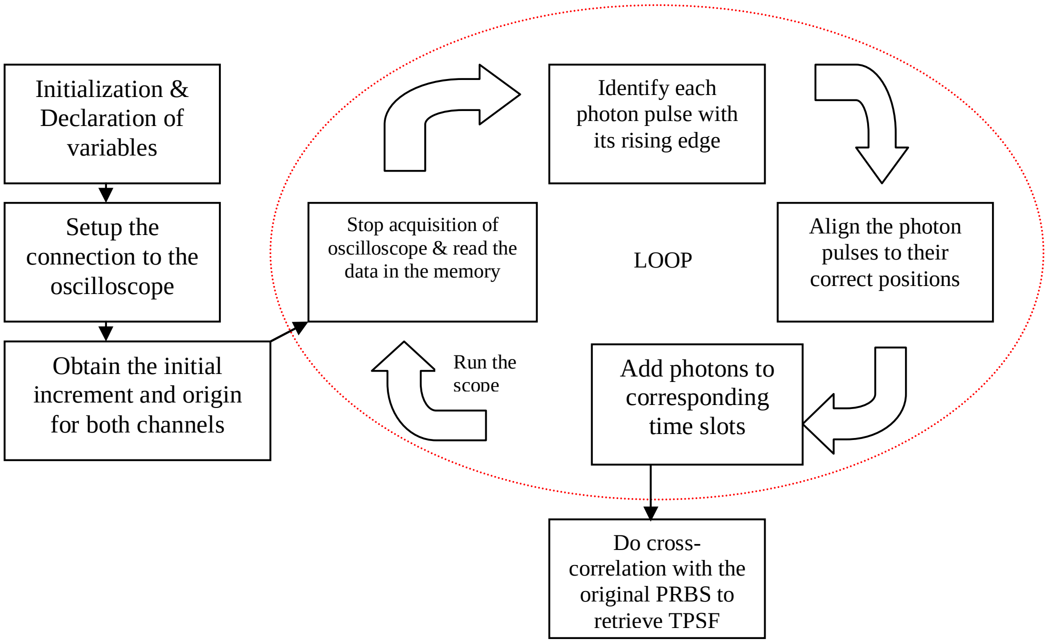

Figure 3.10 Flowchart of the oscilloscope remote control program

Figure 3.10 shows the flowchart of the oscilloscope remote control program. The oscilloscope and the PC are connected via the local area network. A few necessary configurations have been done before the execution of the program. The program begins with the initialization and declaration of the variables for the subsequent part of the program. Next, a virtual instrument software architecture (VISA) object is created to set up the communication with the oscilloscope. The Agilent VISA is part of the input/output (IO) libraries suite product. After the VISA object is created, some parameters of the oscilloscope such as input buffer size and acquisition rate are configured accordingly.

Then, the origins and initial increments for both channel 1 and 2 are acquired before the program goes into a loop. The number of iteration is dictated by the pre-determined acquisition time, which is typically set to 1 second. The program will end and jump out of the loop when the pre-determined time has been reached.

In the loop, the program executes these 4 main steps repeatedly: (1) Stop acquisition of oscilloscope & read the data in the memory; reading data from the oscilloscope memory results in a dead time around 0.5 second; (2) Identify each photon pulse with its rising edge; (3) Align the photon pulses to their correct positions; (4) Add photons to corresponding time slots. Finally, the detected signal is built up, and then correlated with the original PRBS to retrieve the desired TPSF. Each loop typically takes about 0.6 second to finish.

3.2.2.3 Conducting experiments with the PRSPC prototype

1) Calibration experiment

This experiment is to measure the impulse response of the PRSPC system, which is an indication of the system time resolution. The beam emitted by the transmitter is attenuated by a neutral density filter (20% transmission), and then collected by the SPC detector. The optical fibers of the transmitter and the SPC detector are aligned in a line and separated by 5 cm. The acquisition time is set to be 1 second. As shown in Figure 3.11(b), the rise time (20%-80%) is measured to be about 150 picoseconds.

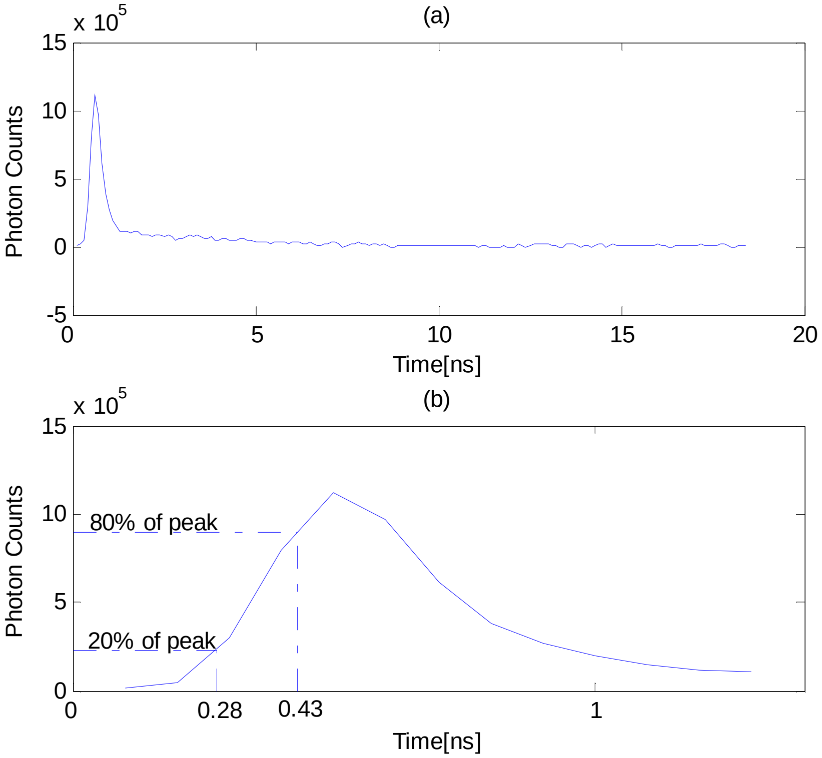

Figure 3.11 Calibration result. (b) is the zoom-in view of (a).

2) Phantom experiments

In order to mimic the real human breast tissue, tissue-like solid phantom slabs [110,111] are utilized. The fabrication process is detailed in Appendix A.3.2. The phantom mainly includes two parts:

Part 1: Bulk phantom (Figure 3.12(a)) which has similar optical properties as human breast tissue [112]:

- Solid epoxy resin phantom (permanent, easy to be machined into shape and for inclusions);
- Cylindrical stacked-up design (more flexible positioning of inclusions);
- μ_s'~6 cm^{-1} , due to scatters (titanium dioxide);
- μ_a~0.02 cm^{-1}, due to chromophores;
- Diameter~7.5 cm;

- Thickness~0.5 cm;

Part 2: Phantom lesions (Figure 3.12(b)) to mimic tumor in human breast:

- Cylindrical stacked-up design;
- μ_s'~6 cm^{-1} , similar to that of part 1;
- 4~5 times μ_a of part 1;
- Diameter~0.7 cm;
- Thickness~0.5 cm;

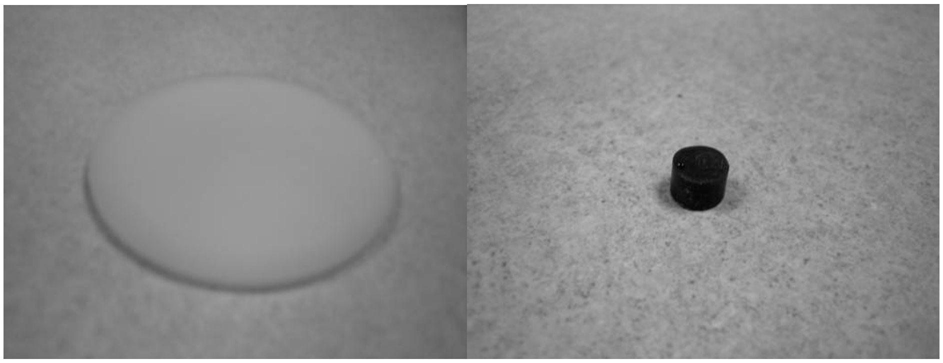

(a) (b)

Figure 3.12 Illustration of tissue phantom and lesion phantom

Phantom lesion is embedded into tissue phantom as indicated in Figure 3.13.

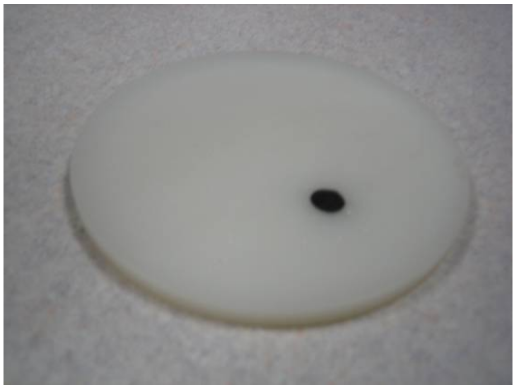

Figure 3.13 Phantom with lesion embedded

During experiments, the solid tissue phantom slabs of various thicknesses were inserted between the transmitter and the single photon detector, while the optical fibers of the transmitter and the SPC detector were aligned in a line and separated by 5 cm. The temporal point spread function of light diffusing through the phantom sample was measured.

Shown in Figure 3.14 are TPSFs for tissue phantom slabs with a thickness of 1 cm (thin curve marked with dots) and 2 cm (thick curve), respectively. The acquisition time is set to be 1 second. The intensity decrease and temporal shift of the TPSF amplitude accompanying the increase of phantom thickness complies with the diffusion theory [113-115].

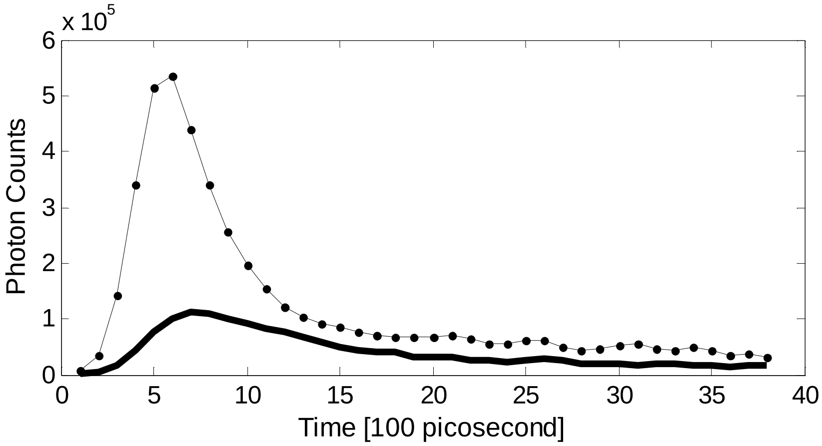

Figure 3.14 TPSFs of light diffusing through solid breast tissue phantom.

Shown in Figure 3.15 are TPSFs for tissue phantom slabs with a thickness of 3 cm. The acquisition time is set to be 1 second. When acquiring the black dots curve, a phantom lesion shown in Figure 3.12(b) was embedded in the centre of the slabs, while the thin curve involved no phantom lesions. The strong absorption of the phantom lesion has caused the temporal shift and the amplitude change of the TPSF, and also the reduced early arriving photons [113-115].

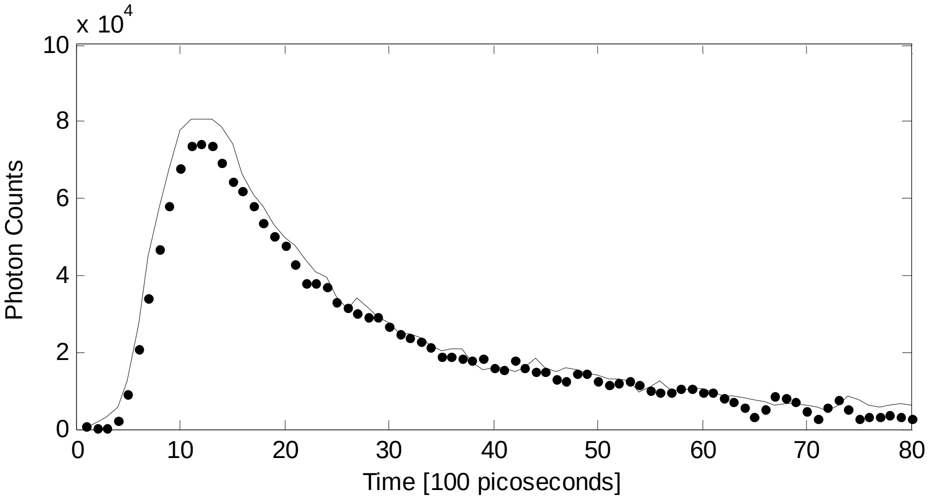

Figure 3.15 TPSFs of light diffusing through solid breast tissue phantom. Black dots, phantom lesion embedded.

Chapter 4 Pseudo-random single photon counting: a high speed implementation

In Chapter 3, a prototype PRSPC system was built. Although the phantom experiments results demonstrated the validity of the method, such a system is not suitable for real time time-resolved measurements due to the long overhead time spent on reading data from the oscilloscope memory.

This chapter systematically describes the design and implementation of a high speed pseudo-random single photon counting system which is based on the spread spectrum time-resolved method combined with single photon counting. The first part of this chapter illustrates the configuration of this PRSPC system including an overview of the system diagram and the configurations of some key components and modules. Then, the system performance is characterized and evaluated. At the end of the chapter, a short summary is made to compare the performance of this system to the TCSPC and the SSTR methods.

4.1 General objectives

It has been mentioned in 3.2.2.2 that for the PRSPC prototype system, only a limited length of pulse sequence can be read from the oscilloscope each time due to its limited memory. Reading data from the oscilloscope memory results in a dead time around 0.5 second. The data transferring and processing would take another 0.1 second. If a 10G sampling rate is used, a pulse sequence over a 26.2 μs time span can be recorded at once and transferred to the PC through local area network. For diffuse photon measurements, a pulse sequence over a time span of 1 second is typically necessary given a photon count rate around 1M cps. In the case of the PRSPC prototype, it would take hours to acquire such a sequence! It is clear that such a system is not suitable for real time measurements.

This part of work aims to build a high speed PRSPC system which can be used for real time measurements, specifically:

- The system initially involves 1 light source and 1 SPC detector but is ready for upgrading to multiple light sources (multiple wavelengths) and detectors.
- The system should balance cost with performance. For example, to achieve a high temporal resolution, a high data rate PRBS source should be used. A 10 Gbps PRBS generator is chosen, because the slight improvement of temporal resolution brought by a higher data rate PRBS generator, e.g. a 40 Gbps generator, does not justify the additional cost.
- The system should be capable of real time or near real time data acquisition. To achieve this, reading photon pulses output from the SPC detector and processing them should be conducted simultaneously or near simultaneously. A high resolution timing module which can continuously time-tag the photon pulses and transfer data to a PC is employed to perform the function.
- The temporal resolution is a key system specification. Theoretically, the full width at half maximum (FWHM) of the measured system response

should be equal to the time span of one bit of PRBS. If a 10G bps PRBS is used for modulation of the transmitter, the theoretical FWHM is 100 ps. However, due to the limited bandwidths of the optical transmitter and the electrical components, the real temporal resolution is usually worse than the theoretical value.

- The system should be automatically controlled by a computer in LabVIEW and MATLAB environments.

- The system should be compact and of low cost, compared with the conventional TCSPC method. It should be convenient to be integrated into a time-resolved optical measurement system, such as a time-resolved DOT system or a FLIM system.

4.2 System overview

Figure 4.1 shows the system schematic diagram. A broadband PRBS source is used to generate a high data rate PRBS with an adjustable pattern length. An optical transmitter which is capable of high speed modulation is modulated by the PRBS, and its output is coupled to a multimode optical fiber. This multimode fiber directs the laser beam to the sample under investigation and the diffuse photons are collected by a SPC module. The blue box in the figure indicates where proper optical alignment is needed to cater specific experimental aims as well as to ensure optimal photon detection efficiency. The electrical pulses output by the detector representing the photon events are amplified and collected by a timing module which can continuously time-tag the rising edge of each single pulse. A trigger signal from the PRBS generator is offset by a certain level and then collected by the timing module as a reference signal for synchronization. The time tags for both the photon pulses and the reference signal are continuously transferred to the PC. The data transferring process is controlled by LabVIEW programs, which also accumulate the recorded photons to build up the histogram representing the signal arriving at the SPC detector and perform the cross-correlation to retrieve the time spectrum of the detected photons.

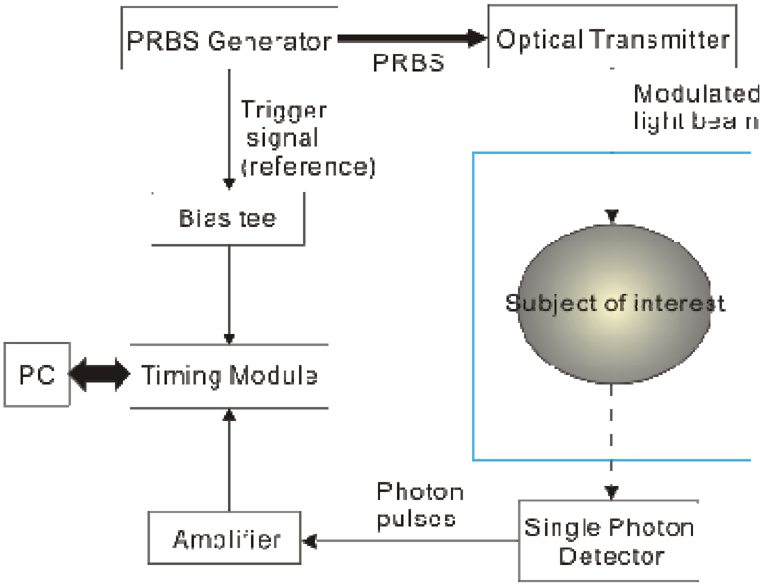

Figure 4.1 Schematic diagram of the high speed PRSPC system

4.3 Key components

4.3.1 Optical modules

The key issues for optical modules are modulation depth at high data rate, the coupling efficiency among optical modules and the detecting efficiency of the detector at extreme weak light condition.

4.3.1.1 Transmitter

The V-226 model (Figure 4.2) from California Scientific is used as the optical transmitter.

Figure 4.2 V-226, CSI

V-226 is a VCSEL transmitter which is capable of high speed modulation up to 12.5 Gbps. The module has a data input with an SMA connector (the rightmost in above figure) and optical output with an FC multimode connector (middle connector). The modulation depth is adjustable through the control knob on the left. Some of the key specifications of V-226 are shown in Table 4.1 and the typical eye diagram is shown in Figure 4.3.

Table 4.1 V-226 specifications

	Min	Nominal	Max
Wavelength (nm)	840	850	860
Bit Rate (Gbps)	0.001		12.5
Output Power at max setting (mW)	1.5		2.2
Rise / Fall Time (ps)		25/35	
RMS jitter (ps)			3.0
Modulating Amplitude (mV)	100	300	500
Extinction Ratio (dB)			6

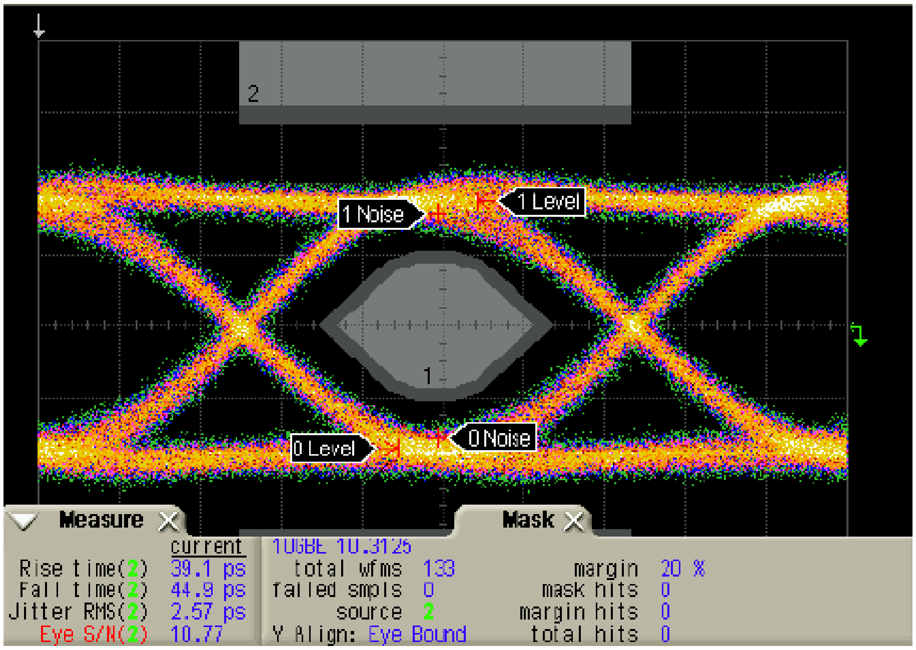

```
                 current      10GBE 10.3125
   Rise time(2)  39.1 ps       total wfms  133              margin  20 %
   Fall time(2)  44.9 ps      failed smpls 0              mask hits  0
 Jitter RMS(2)   2.57 ps            source 2            margin hits  0
    Eye S/N(2)   10.77        Y Align: Eye Bound         total hits  0
```

Figure 4.3 Typical 10G loop eye diagram of the V-226 VCSEL source

4.3.1.2 Fibers

The fibers utilized in the system are multimode (MM) fibers with a core/cladding of 62.5/125 microns. The MM fiber directs the modulated light beam from the transmitter to the subject under investigation. It can also be used to collect the light beam containing the subject’s information and direct it to the detector.

The 62.5/125 multimode optical fiber is widely used in optical measurements. 62.5 refers to the outer diameter of the multimode optical fiberglass core while 125 refers to the outer diameter of the cladding, and the measurement unit is micron. The structure of the basic type 62.5/125 multimode fibers is shown in the below figure.

Figure 4.4 62.5/125 multimode optical fiber

The 62.5/125 multimode fiber cable assemblies can be with various kinds of jacket, like OFNR, OFNP, LSZH, etc and the connector types are optional like SC, FC, LC, ST and MTRJ. For the PRSPC system, the OFNR jacket and FC connector are chosen.

4.3.1.3 Single photon counting detector

ID Quantique's id100-20 (Figure 4.5) is used as the single photon counting detector in the PRSPC system. Id100-20 is a compact free-space module with an active area diameter of 20 micron. It offers ultra-high timing resolution and state-of-the-art dark count rate based on a reliable silicon avalanche photodiode sensitive in the visible spectral range. In the PRSPC system, this SPC detector is mounted with a standard optical post holder using the M4 thread located on the bottom side.

Figure 4.5 Id 100-20 SPC detector

The operating principle of id100-20 is shown in Figure 4.6. An avalanche photodiode (APD) and an active quenching circuit are integrated on one silicon chip. The chip is mounted on a thermo-electric cooler and packaged in a standard TO5 header with a transparent window cap. The temperature can be measured by a thermistor. The APD is operated in Geiger mode, i.e. biased above breakdown voltage. A high voltage supply used to bias the diode is provided by a DC/DC converter. The quenching circuit is supplied with +5V. The module output pulse indicates the arrival of a photon with high timing resolution. The pulse is shaped using a hold-off time circuit and sent to a 50W output driver. All internal settings are preset for optimal operation at room temperature.

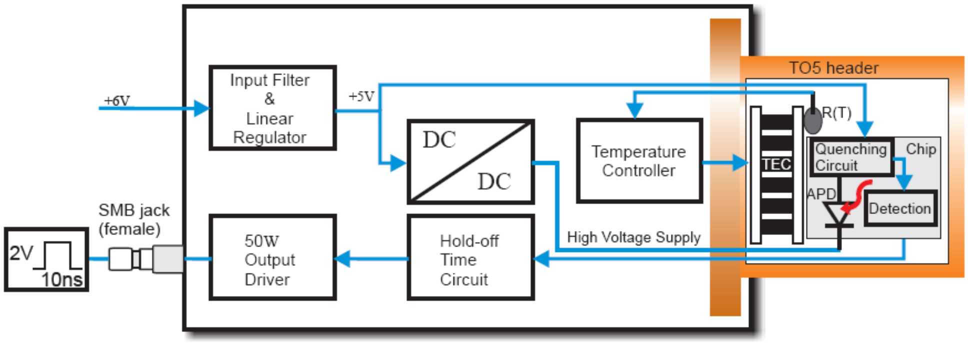

Figure 4.6 Block diagram of the id100-20 SPC detector

Some key specifications of the id 100-20 are shown in Table 4.2.

Table 4.2 Operating performance of id100-20

Parameter	**Min**	**Typical**	**Max**	**Units**
Wavelength range	350		900	nm
Timing resolution [FWHM]		40	60	ps
Single-photon detection probability*				%

at 400nm		18		%
at 500nm		35		%
at 600nm		25		%
at 700nm		18		%
at 800nm		7		%
at 900nm		4		%
Afterpulsing probability			3	%
Output pulse width	9	10	15	ns
Output pulse amplitude	1.5	2	2.5	V
Deadtime		45	50	ns
Maximum count rate (pulsed light)		20		MHz

* As the wavelength of light source in the PRSPC system is 850 nm, the actual photon detection probability is around 5%.

4.3.2 Electrical modules

4.3.2.1 PRBS generator

The TG2P1A wideband pseudo-random bit sequence generator (Figure 4.7) from Centellax is used. A customized pattern trigger signal with a period of 32 times of the PRBS repetition time is used as the reference signal for synchronization purpose. The TG2P1A is capable of operating from 0.05 to 12.5 Gbps and 10 Gbps is used in the PRSPC system.

Figure 4.7 TG2P1A pattern generator

The pattern generator can be programmed to generate five PRBS pattern lengths and three mark/space densities. Patterns 7, 10, 15, 23 and 31 correspond pattern lengths of 2^7-1, 2^{10}-1, 2^{15}-1, 2^{23}-1 and 2^{31}-1, respectively. For the PRSPC system, a pattern 10 PRBS with mark/space density of ½ is used for modulation. Some operating specifications of the pattern generator are shown in the following table.

Table 4.3 Specifications of the TG2P1A pattern generator

Parameters	**Minimum**	**Typical**	**Maximum**
Ext. Clock Speed	0.05 GHz		12.5 GHz
Output Bit Rate	0.05 Gbps		12.5 Gbps
RMS Jitter (Data)		0.9 ps	
RMS Jitter (Int. Clock)		1.0 ps	
20-80 Rise/Fall Times		23 ps	25 ps
Eye Height	200 mV(p-p)	250 mV(p-p)	
Eye Amplitude	250 mV(p-p)	300 mV(p-p)	
OPT008 Eye Amplitude	700 mV(p-p)	800 mV(p-p)	
Eye SNR	18	22	
Output Voltage Low		- 150 mV	
Output Voltage High		+150 mV	
Clock Power	-1 dBm	+ 2 dBm	+ 3 dBm

4.3.2.2 Timing module

4.3.2.2.1 Overview

SensL's HRMTime module (Figure 4.8) is the first portable USB high resolution timing module on the market. It is a highly functional system incorporating high end timing functions in an easy-to-use, flexible and high performance module. Most importantly, its timing circuitry enables time bins down to 27 ps and is available in one, two or four channels. The system is compatible with any photon counting sensor with TTL output. The DLL libraries and LabVIEW drivers simplify the integration of the HRMTime into any timing instrument or application.

Figure 4.8 HRMTime Timing module from Sensl. A-H, Channel 0-3 Start&Stop Input (SMA TTL); I, USB connector; J, power supply connector; K, 16-way I/O port connector; L, Programmable Clock output (SMA TTL 50 ohm)

The input/output specifications of the HRMTime are shown in the below table.

Table 4.4 Specifications of the input/output of HRMTime

Start and Stop	TTL - SMA connector x 2 (per channel)
I/O Ports	16 general purpose I/Os, User configurable LVTTL (3.3V)
USB	High speed USB 2.0 (miniature connector)
Programmable Clock	TTL 50Ω SMA output up to 100MHz

4.3.2.2.2 System architecture

As shown in Figure 4.9, the HRMTime system combines a high performance time-to-digital converter with a high end FPGA, on-board memory and a high speed USB 2.0 interface. The FPGA is the heart of the system and controls all aspects of operation in addition to performing commands from the external host computer. It uses a proprietary communication protocol for communication with the host PC running the SensL Integrated Environment over the high speed USB 2.0 connection.

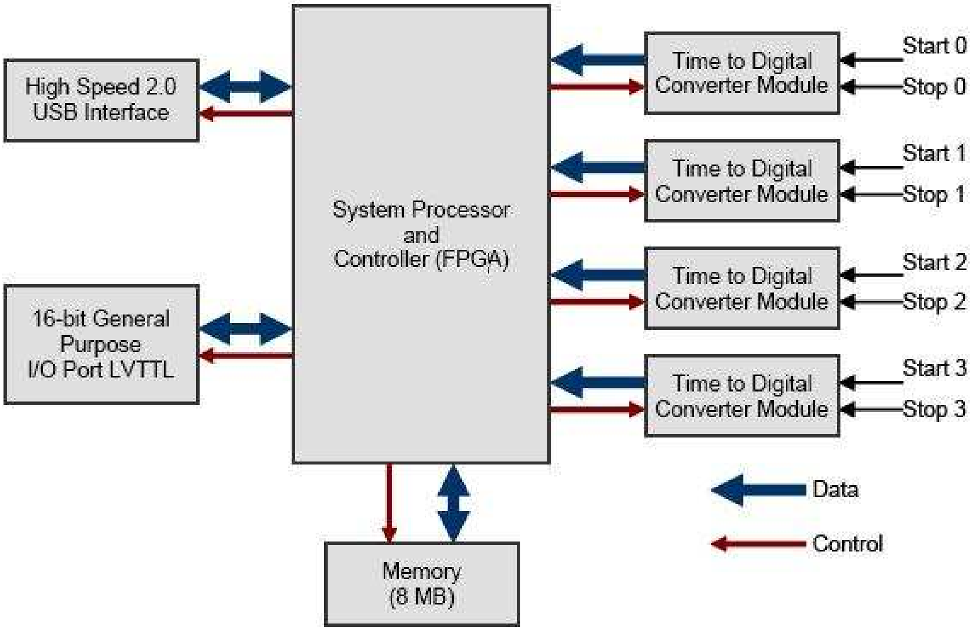

Figure 4.9 System architecture of HRMTime

In the PRSPC system, only two channels, i.e. Channel 0 and 1 are used for data input. Channel 0 collects the reference signal from the PRBS generator (TG2P1A) which is to be used as synchronization signal in data processing, while Channel 1 records the single photon counting signal from the SPC detector (id100-20).

4.3.2.2.3 The FIFO time-tagging functionality

HRMTime comes with five optional functionalities, namely multi-channel scaler/counter, multi-dimensional time correlated single photon counting, time-binning, time-tagging (micro and macro) and auto/cross correlation. For the PRSPC system, only the time-tagging function is utilized to record the arriving time of every single photon pulse.

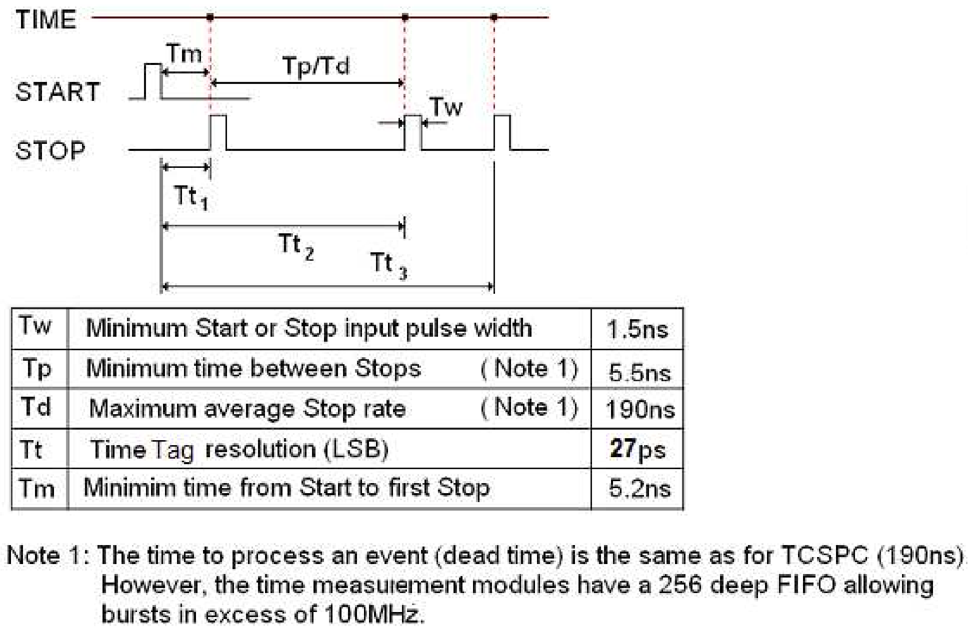

Tw	Minimum Start or Stop input pulse width	1.5ns
Tp	Minimum time between Stops (Note 1)	5.5ns
Td	Maximum average Stop rate (Note 1)	190ns
Tt	Time Tag resolution (LSB)	**27**ps
Tm	Minimim time from Start to first Stop	5.2ns

Note 1: The time to process an event (dead time) is the same as for TCSPC (190ns). However, the time measurement modules have a 256 deep FIFO allowing bursts in excess of 100MHz.

Figure 4.10 Time-tagging principle of the HRMTime timing module

As shown in Figure 4.10, in the time-tagging mode a single start pulse will be applied to all channels. For this study, the programmable clock output is applied to both Channel 0 and Channel 1. Once the start pulse is detected the module time-stamps the event and stores the data in the module memory. Another process takes the data out of the memory and passes it to the PC through the USB, i.e. the data is being uploaded in real-time. The speed of the USB limits the maximum event rate that can be recorded. In addition the maximum event rate and maximum recording period will be limited by the PC specification (i.e., whether the data is being stored in the PC’s memory or directly onto the hard disk) as well as the memory and hard disk size. Changing the timing resolution does not impact the performance or number of data points that can be collected. Some of the performance parameters of the HRMTime under the time-tagging mode are shown in the below table.

Table 4.5 Time-tagging specifications

Parameter	Min	Max	Note
Time Resolution	27ps		Multiples of 27ps
Maximum Sustained Count Rate		4.5Mcps	PC Hardware dependent
Max Recording Time		Infinite	PC Hardware dependent

Data collected in this time-tagging mode can be displayed, analyzed and manipulated via the specific tools in the SensL Integrated Environment software. The data, including the time stamps, are available to the user for export as data files.

4.3.2.2.4 The user interface

The Sensl Integrated Environment (Figure 4.11) is capable of streaming the recorded data from the HRMTime to a PC and saving into a text file. The text file can be then loaded into MATLAB program for data processing.

Nevertheless, to realize real time measurement of temporal profiles for the PRSPC system, a single program which can perform the data streaming and processing simultaneously is highly in need. Hence, the DLL library and LabVIEW drivers are utilized to develop a customized interface in LabVIEW environment. This will be detailed in 4.3.4.

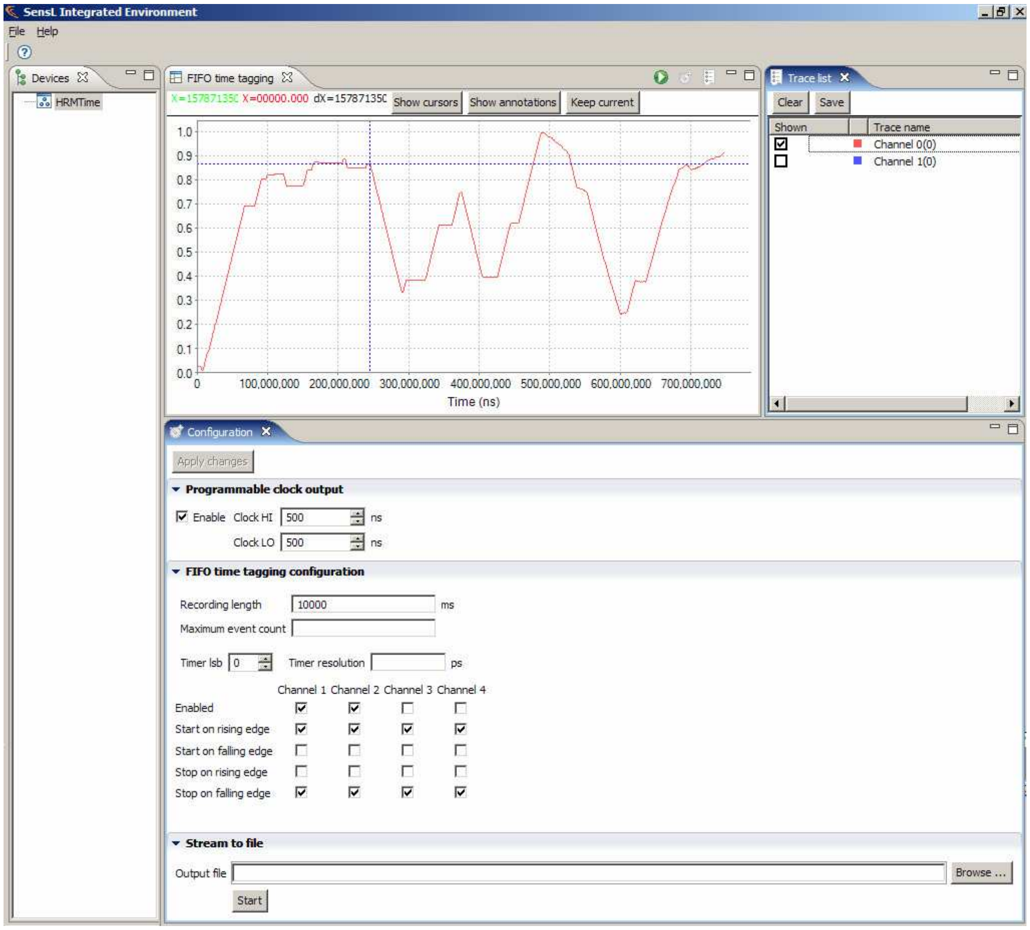

Shown		Trace name
☑	🟥	Channel 0(0)
☐	🟦	Channel 1(0)

Programmable clock output

☑ Enable Clock HI 500 ns

Clock LO 500 ns

FIFO time tagging configuration

Recording length 10000 ms

Maximum event count

Timer lsb 0 Timer resolution ps

	Channel 1	Channel 2	Channel 3	Channel 4
Enabled	☑	☑	☐	☐
Start on rising edge	☑	☑	☑	☑
Start on falling edge	☐	☐	☐	☐
Stop on rising edge	☐	☐	☐	☐
Stop on falling edge	☑	☑	☑	☑

Stream to file

Output file

Figure 4.11 Sensl Integrated Environment

4.3.2.3 Bias tee

Table 4.4 indicates that the timing module requires an input voltage of TTL level (around 2.5 V under 50Ω load) while Table 4.2 indicates the output pulse amplitude from the SPC detector (id100-20) is only 2V. Thus, a bias tee from Mini-Cricuits (Figure 4.12) was used to raise the voltage level of the output pulses of the id100-20 by 0.5V so that it can be recognized as a ‘Stop’ signal by the HRMTime.

Figure 4.12 Coaxial bias tee

4.3.2.4 Amplifier

Similar as the use of bias tee, the use of amplifier is to amplify the voltage level of the reference signal from the PRBS generator so that it reaches TTL level and can be recognized by the HRMTime as a ‘Stop’ signal. A low distortion, high slew-rate current feedback amplifier from Texas Instruments, THS3061 (Figure 4.13) was selected and its gain was modified to realize the proper amplification.

Figure 4.13 THS3061 evaluation module

4.3.3 Auxiliary modules

In this part, the modules introduced are not directly involved in the PRSPC system yet essential to ensure normal operation of the system.

- A digital storage oscilloscopes (54852A, Agilent) and a serial data analyzer (SDA100G, LeCroy) intensively used for signal integrity analyzing and circuitry trouble-shooting. The 54852A has 2 GHz bandwidth and a maximum sampling rate of 10 GS/s while the SDA 100G can be used for signal with data rate up to 100G. The SDA 100G also has a complimentary module PPG-E135, which can generate high speed PRBS up to 12Gbps.

- Two linear power supplies. EX752M from TTI used for DC offset of the bias tee (4.3.2.3) and BPS4000 from Calex used for voltage supply of the amplifier (4.3.2.4).

- A high speed 850nm photodetector (P-101, CSI), used to check the modulation of the output from the optical transmitter.

- RG-58U coaxial cables to connect different electrical components. RG-58U coaxial cables keep uniform characteristic impedance of 50 Ω up to a few GHz in room temperature which minimizes the reflectance effect of the high data rate PRBS signals in transmission paths due to the impedance mismatch.

- A small optical table (PBH11105, Thorlabs) used as base for necessary optical alignment.

- A lightproof cabinet (Figure 4.14), used to prevent the room light from entering the SPC detector. The cabinet is placed on top of the optical table.

Figure 4.14 Lightproof cabinet

4.3.4 Human-machine interface

The PRSPC system uses the LabVIEW based graphic user interface (GUI) as the human-machine interface. In addition, the MATLAB program maybe called in the LabVIEW GUI to perform necessary operation.

4.3.4.1 User console GUI

The LabVIEW and MATLAB based GUI user console offers a user friendly human-machine interface to control the systems hardware, modify/monitor operation parameters, conduct data acquisition, display time-resolved measurements and report system failure. It also facilitates convenient integration of the data acquisition program into a comprehensive program for future time-resolved spectroscopy measurements or diffuse optical imaging experiments.

LabVIEW (version 8.2) and MATLAB (version 7.1) were utilized to build the user console GUI on MS windows XP Professional SP3 operation system. Real-time data acquisition and preliminary data processing of the recorded data from the HRMTime was carried in LabVIEW, while the post data processing, which mainly includes the cross-correlation operation, was carried by calling MATLAB in LabVIEW using MS windows ActiveX technique.

Figure 4.15 shows the screenshot of the PRSPC user GUI. Appendix A.2 shows the detailed block diagram structure of the LabVIEW program.

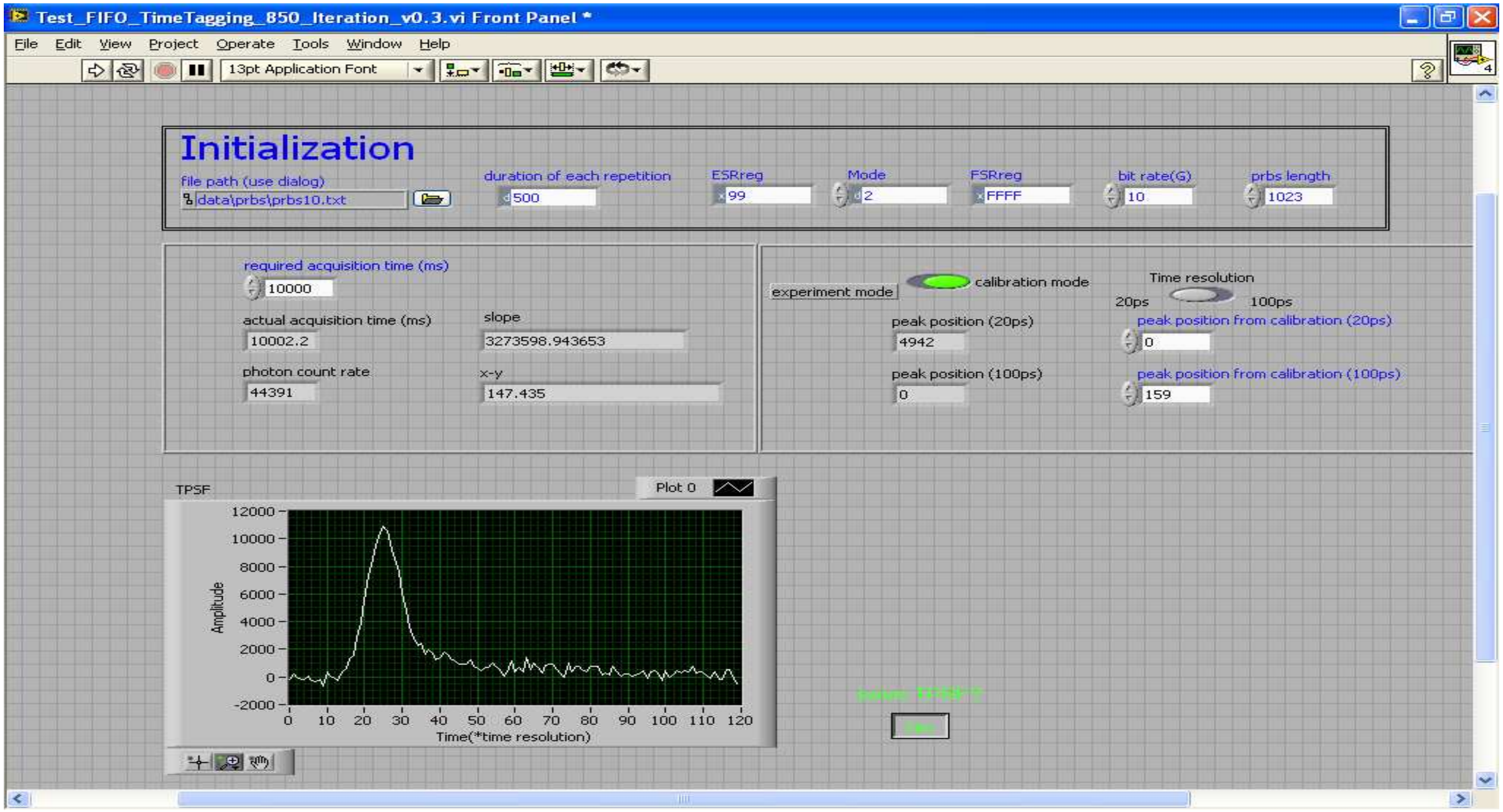

file path (use dialog): data\prbs\prbs10.txt
duration of each repetition: 500
ESRreg: 99
Mode: 2
FSRreg: FFFF
bit rate(G): 10
prbs length: 1023

required acquisition time (ms): 10000
actual acquisition time (ms): 10002.2
slope: 3273598.943653
photon count rate: 44391
x-y: 147.435

experiment mode / calibration mode
Time resolution: 20ps / 100ps
peak position (20ps): 4942
peak position from calibration (20ps): 0
peak position (100ps): 0
peak position from calibration (100ps): 159

Figure 4.15 PRSPC system user console GUI for temporal profile measurement

4.3.4.2 Data format

The time resolution of the PRSPC system is selectable between 20ps and 100ps. The amplitudes of the recorded temporal profile can be saved to a single column text file. The value of each element in the column represents the photon counts, which proportionately reflects the optical intensity of the temporal profile.

4.4 System performance characterization

4.4.1 Data acquisition speed

In this part, the PRSPC system will be compared to TCSPC in terms of photon count rate which is a key parameter determining data acquisition speed. Unlike the TCSPC method, the pile-up error only imposes minor limitation on the photon count rate in the PRSPC system. The main limitation in the PRSPC system comes from the HRMTime module and the software processing time.

It has been mentioned in 2.2.2.4, that the principle of TCSPC requires that no more than one photon is detected in each cycle; otherwise the pile-up error will occur. This limitation causes a big problem in the data acquisition speed of TCSPC due to low photon count rate.

There are two types of pile-up error in TCSPC. The type E (E for electrical) error is caused by overlapping of two-photons that cannot be distinguished by electronics. The type S (S for statistical) pile-up error, which dominates in TCSPC, results from the fact that a TCSPC device can detect only one photon per excitation period. If the detection rate is so high that the detection of a second photon within the recorded time interval becomes likely, the temporal profile is distorted. It is commonly believed that the pile-up becomes a problem if the photon count rate exceeds 0.1% to 1% of the pulse repetition rate. The typical repetition rate of pulsed lasers is about 100 MHz, which means a maximal photon count rate of 1 MHz. In PRSPC, however, the sample is excited continuously and every photon event is recorded. Thus there is no type S pile-up error. The only pile-up error is of type E, which is more tolerant of high count rate.

A modified state-of-the-art TCSPC system would be type S pile-up error free if it has multi-stop capability. However, this function is usually available for a low excitation repetition rate for commercial TCSPC modules. Even compared with modified TCSPC without type S pile-up error, the PRSPC approach has another advantage in terms of type E pile-up error. The photon detection probability in a TCSPC setup is usually concentrated within a time window much smaller than the excitation period. For example, in fluorescence decay measurement, most photons tend to arrive at the detector immediately after the excitation pulse. In case of PRSPC, the excitation is close to continuous wave and the photon detection probability is more uniformly distributed in the time domain (Figure 3.4(d)). As a result, there will be less type E pile-up error in PRSPC compared to TCSPC given the same count rate. Generally speaking, the maximal photon count rate of PRSPC limited by pile-up error is about two orders higher than TCSPC, which implies a potential faster data acquisition.

The count rate of the PRSPC system is limited by the HRMTime timing module, which is 4.5Mcps (Table 4.5). It is also limited by the data processing time taken by the LabVIEW program. The finalized PRSPC system can reach a photon count rate of 3 Mcps. A 4 Mcps count rate is possible if the data processing time taken by the LabVIEW program can be further reduced.

4.4.2 System calibration

In order to characterize the system's impulse response, the emitted laser beam was attenuated by appropriate neutral density filters and then directly collected by the SPC detector. In Figure 4.16, the rise time (20%-80%) of the impulse response is measured to be around 130 ps, while the full width at half maximum (FWHM) is about 260ps.

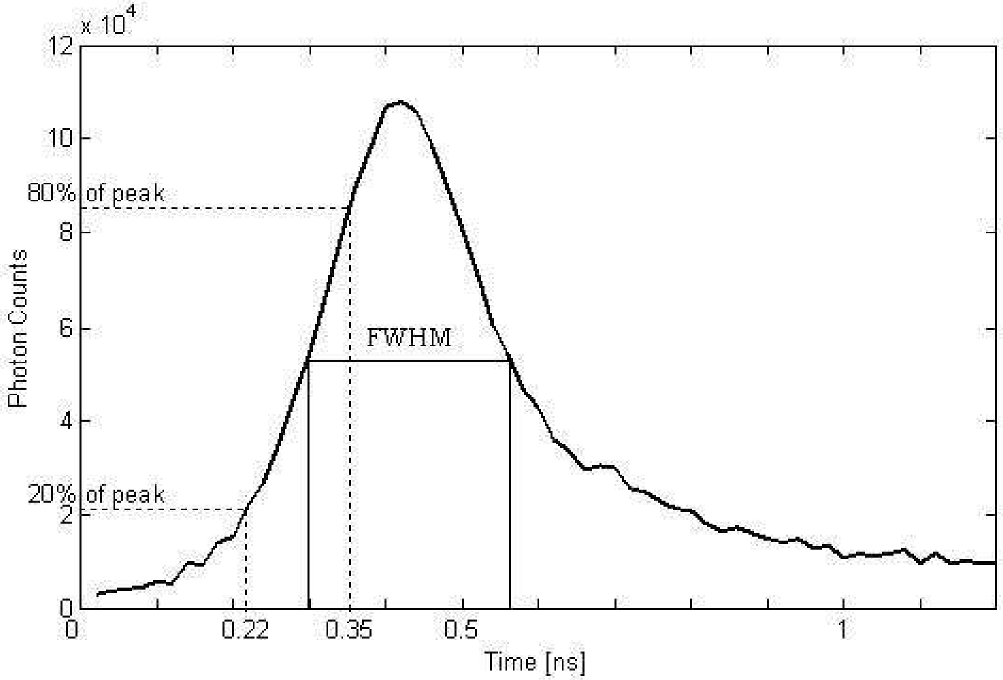

Figure 4.16 Calibration result of the PRSPC system

According to the auto-correlation property of PRBS (Figure 3.3), the FWHM of the PRSPC system response should be equal to the time span of 1 PRBS bit, which is 100 ps given a 10 Gbps PRBS bit rate. The rise time (20-80%) should be close to the smallest time bin size that the HRMTime timing module can reach, which is 27 ps. A few factors have contributed to the spread timing performance of the PRSPC system. The timing jitter of the id100-20 SPC detector resulted from the transit time spread is 40 ps. Besides, the system response can also be spread due to the use of other components such as multi-mode fibers.

4.4.3 System noise

4.4.3.1 Time-domain

To characterize the system noise, system calibration experiments were conducted while the system impulse response shown in Figure 4.16 was repeatedly measured under the identical settings. The variation of the measured calibration results was then tested.

In total, 20 impulse responses were measured, each of which took exactly 3 seconds to accumulate around 1.5 M photons. The average of the 20 impulse responses is shown in Figure 4.17 (a) and the standard deviation of amplitude at each time delay is shown in Figure 4.17 (b). It can be seen that except the peak area, the noise is at the similar level for all time delays. This is due to the cross-correlation operation.

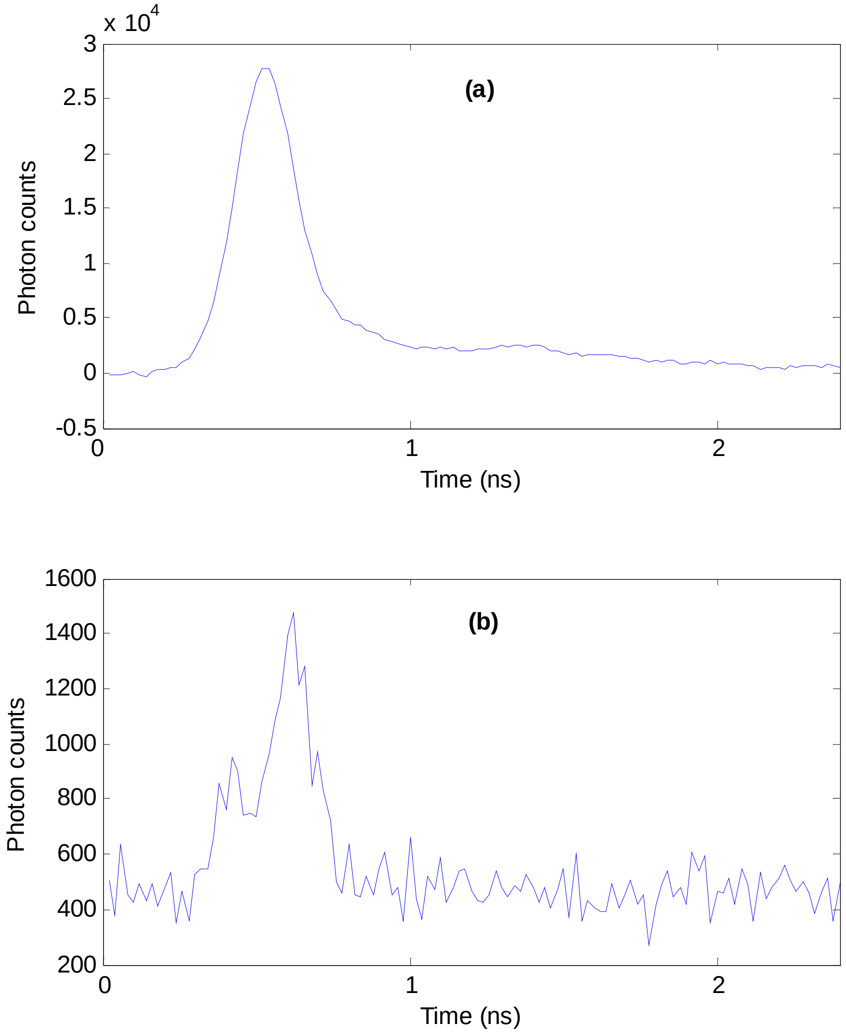

Figure 4.17 System noise characterization

4.4.3.2 Laplace-domain

In Chapter 5 and Chapter 6, in order to utilize feature data, e.g. early arriving photons or late arriving photons instead of full time spectra, Laplace transformed TPSFs will be used for image reconstruction or spectroscopic analysis. For noise level characterization, Laplace transformed system impulse response was also tested.

The measured 20 profiles were transformed into Laplace domain according to the below equation:

$$F_i(S_j) = \int_0^\infty I_i(t)e^{-S_j t}dt\,,$$

where $I_i(t)$ is one of the measured system response profiles, S_j is the Laplace parameter and t stands for time. 9 values were chosen for S_j ranging from -2 Gs^{-1} to +2 Gs^{-1} at a step of 5 Ms^{-1}. When S_j is positive, the front part of the time spectra will be given more weight and the Laplace transformed intensity features early arriving photons; when S_j is negative, the back part of the time spectra will be given more weight and the Laplace transformed intensity features late arriving photons. The bigger the absolute value of the Laplace parameter, the more weight the feature data gains. For each S_j, 20 profiles of the system response generated 20 Laplace transformed intensity, which were then averaged with their standard deviation measured.

The results for system noise characterization in Laplace-domain are shown in Figure 4.18 and Figure 4.19. It can be seen that the noise level is higher for negative than for positive Laplace parameters, corresponding to lower system noise level for early arriving photons measurement.

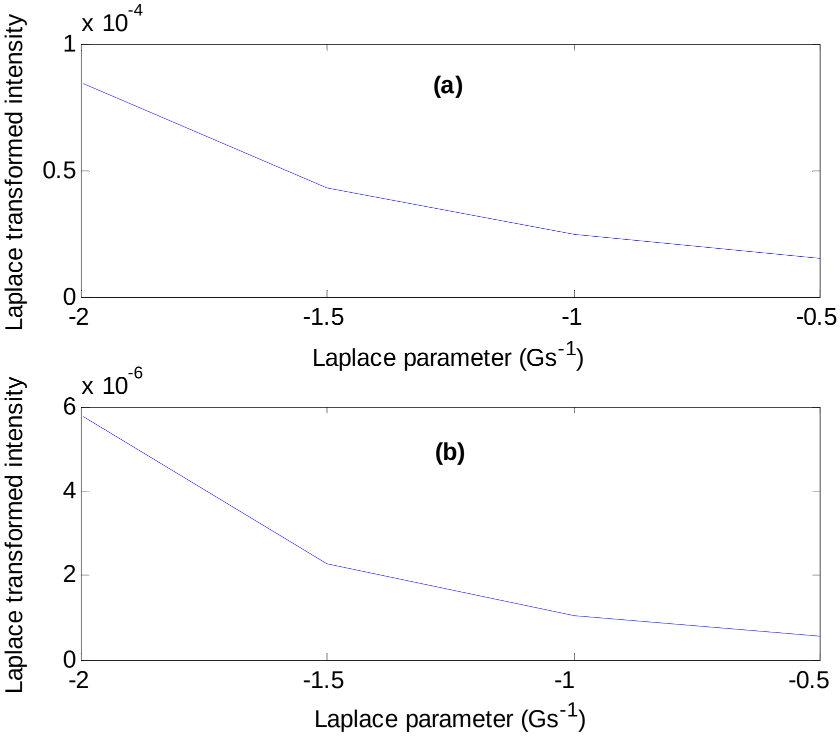

Figure 4.18 Laplace domain noise characterization for negative Laplace parameters. (a) for average intensity, (b) for standard deviation.

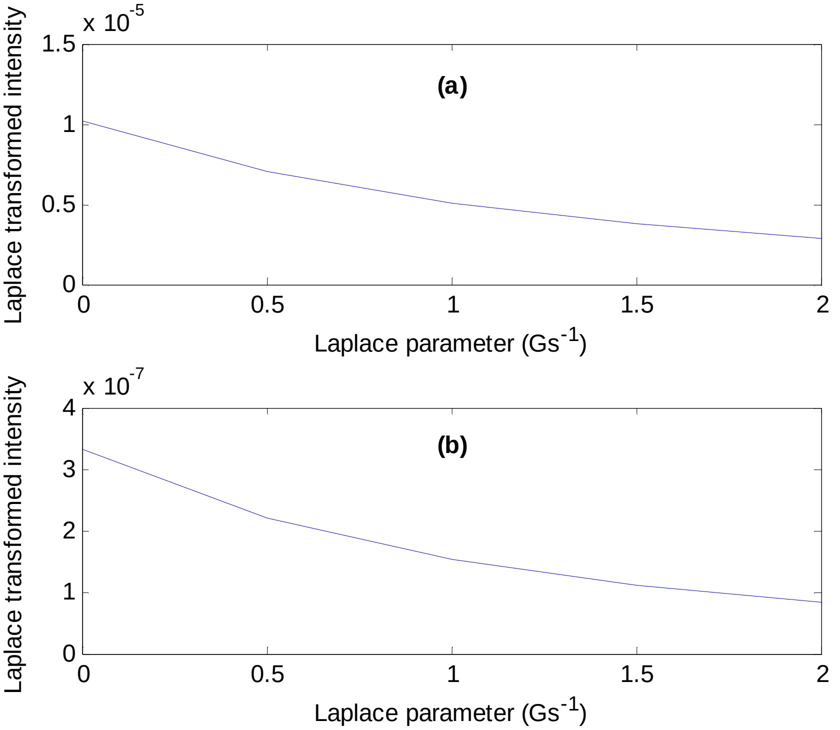

Figure 4.19 Laplace domain noise characterization for zero and positive Laplace parameters. (a) for average intensity, (b) for standard deviation.

Figure 4.20 shows the signal-to-noise ratio as a function of Laplace parameter. Here,

$$SNR = \frac{\mu}{\delta}$$

where μ is the average Laplace transformed intensity and δ is the standard deviation.

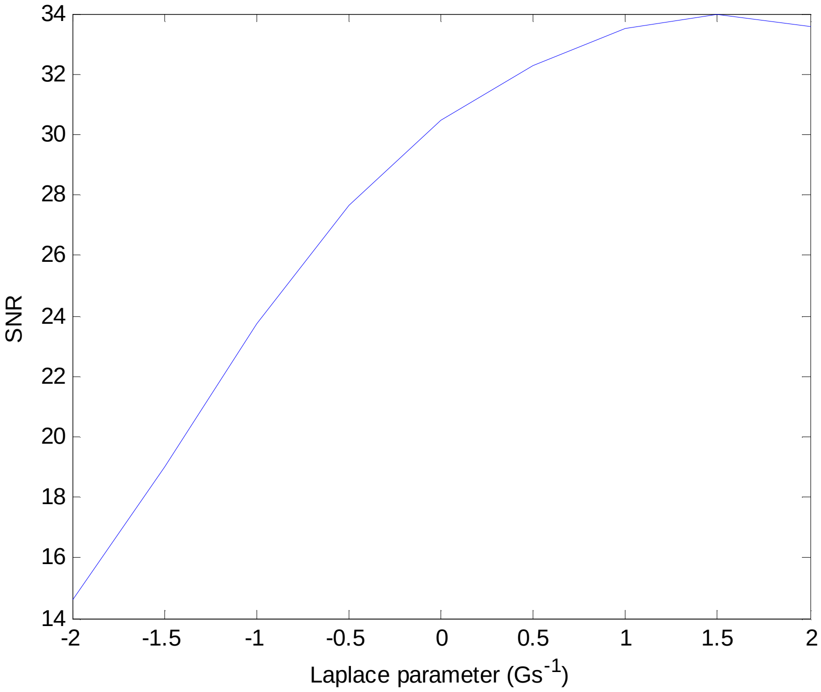

Figure 4.20 Signal to noise ratio as a function of Laplace parameter

It can be seen that the best SNR occurs when the Laplace parameter is chosen to be between 1 Gs^{-1} to 2 Gs^{-1}. This provides valuable guidance for the following chapters which employ Laplace transformed temporal profiles for time-resolved imaging or spectroscopy experiments.

4.5 Summary and discussion

This chapter describes the design and implementation of a novel PRSPC system combining the single photon counting technique with the SSTR method. Compared with the prototype PRSPC system, this high speed implementation realized real time data acquisition. It can reach a photon count rate of 3Mcps which is limited by the HRMTime timing module and the data processing time taken by the Labview program.

The PRSPC method was developed to achieve a comparable operation performance as the conventional TCSPC method and faster data acquisition. The PRSPC system reported in this chapter achieves high speed data acquisition and retains the key advantages of TCSPC. For comparison purpose, the key performance parameters of the three methods, including PRSPC, TCSPC and SSTR, are listed in the following table.

Table 4.6 Key performance parameters of the 3 time-resolved optical measurement methods

	TCSPC	SSTR	PRSPC
Time resolution	Ultra high. Limited by TTS and trigger accuracy in the electronic system.	Limited by the width of the detector impulse response. One order lower than that of TCSPC.	High. Mainly determined by the band width of the PRBS. FWHM~260ps; Rise time (20-80%)~130ps
Sensitivity	Ultra high. Down to the single photon level.	Lower than that of TCSPC	Same with TCSPC
Acquisition speed	Limited by the low photon count rate, typically below 1Mcps.	Fast acquisition speed	Can reach higher photon count rate (above 3Mcps) and thus a faster acquisition speed.

It can be seen from Table 4.6 that the PRSPC method does not sacrifice much operating performance compared with TCSPC yet achieved higher photon count rate and faster data acquisition. Besides, the PRSPC system also offers portability and low cost, which are clearly not with TCSPC.

TCSPC requires a picosecond or femtosecond laser system, which is generally very bulky and of high cost. In contrast, PRSPC uses small laser diodes as light sources. In addition, a commercial TCSPC module (e.g., from Becker & Hickl) typically costs more than 15,000 €, while the key components of the PRSPC system, the HRMTime timing module only costs 9,000€. Based on the above comparisons, the PRSPC system is significantly less expensive and more compact. We expect our PRSPC system will be very competitive in terms of performance to cost ratio.

In the following two chapters, the PRSPC system will be integrated into different experimental systems to explore its applications in time-resolved measurements.

Chapter 5 Time-resolved diffuse optical imaging based on PRSPC method

The past decades have witnessed a growing interest in applications of diffuse optical imaging (DOI) in medical diagnoses and biomedical research, such as breast cancer detection [116-118], functional brain imaging [119-121] and small animal imaging [122]. DOI is noninvasive and nonionizing, has a large penetration depth and functional imaging capability. The three fundamental measurement schemes in DOI can be categorized as continuous-wave, frequency-domain and time-domain [123-126]. Compared to the frequency-domain and continuous-wave DOT, it has been proved that the time-domain DOT may generate reconstructed images of higher spatial resolution due to the more information obtainable by investigating the full time spectra [123,124].

As aforementioned, PRSPC was developed as a method to be used in time-resolved techniques. With high time-resolution and sensitivity, it can measure the temporal profile of a certain subject, when illuminated by an ultra-short light pulse. In this chapter, a simple time-resolved diffuse optical imaging experimental system was built up based on the PRSPC system described in Chapter 4. Liquid phantom studies have been conducted to explore the potential applications of PRSPC in time-resolved diffuse optical imaging.

5.1 Fabrication of liquid phantom

As a polydisperse, lipofundin at different concentrations can be used to mimic the optical properties of biological tissues in bioimaging research [127].

Figure 5.1 shows the lipofundin emulsion product used in this study (Lipofundin MCT/LCT 20%, B.Braun Melsungen AG, Germany). 1.32 mL Lipofundin MCT/LCT 20% was mixed with 86.64 mL distilled water so that the lipofundin concentration was 0.3%. The water for lipofundin dilution was obtained from distilled water at room temperature.

Figure 5.1 Lipofundin emulsion (B. Braun Melsungen AG).

For wavelength of 850 nm, the μ_a and μ_s' of the liquid phantom are dominated by water and lipofundin respectively. At room temperature (25^{o}C), the absorption coefficient of water is 0.02 cm^{-1}. The absorption contributed from lipofundin emulsion is negligible. The scattering property is dominated by the scattering properties of the lipofundin. In order to estimate the phantom's scattering property, the Mie theory was used to calculate the intrinsic μ_s' of lipofundin suspension. The calculation procedure can be found in Appendix A.3.1. The results show the reduced scattering coefficient μ_s' of 0.3% lipofundin liquid phantom is approximately of 2.9 cm^{-1}.

5.2 Experimental setup

The schematic of the DOI experimental setup is presented in Figure 5.2.

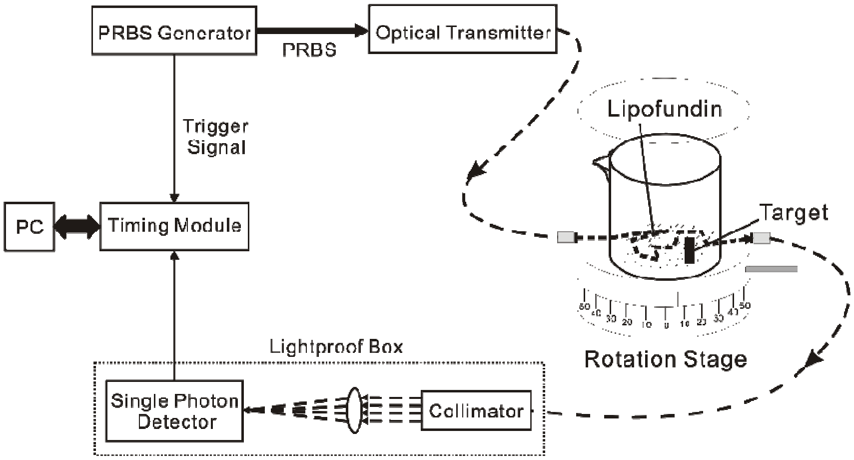

Figure 5.2 Schematic of the time-resolved DOI experimental setup. The dash lines represent the optical signal path and the solid lines represent the electrical signal.

The DOI experimental setup employed the PRSPC system shown in Figure 4.1 and a rotation stage (see Appendix A.4.1) with proper optical path alignment. The device information of the PRBS generator, optical transmitter, single photon counting detector and the HRMTime timing module has been elaborated in Chapter 4.

The TG2P1A broadband PRBS source is used to generate a 10 Gbps PRBS with a pattern length of 2^{10}-1 bits. The 850 nm VCSEL transmitter (V-226) is modulated by the 10Gbps PRBS, and its output is tuned to 1mW power and coupled to a multimode optical fiber (core diameter~62.5 μm). This multimode fiber directs the laser beam to the sample under investigation.

As shown in Figure 5.3, the 0.3% lipofundin suspension is contained in a transparent beaker as the sample background and a small cylindrical absorber (diameter = 7 mm, length = 18 mm, $\mu_a \approx 0.1$ cm^{-1}, $\mu_s' \approx 8$ cm^{-1}) is immersed in the lipofundin suspension as the target.

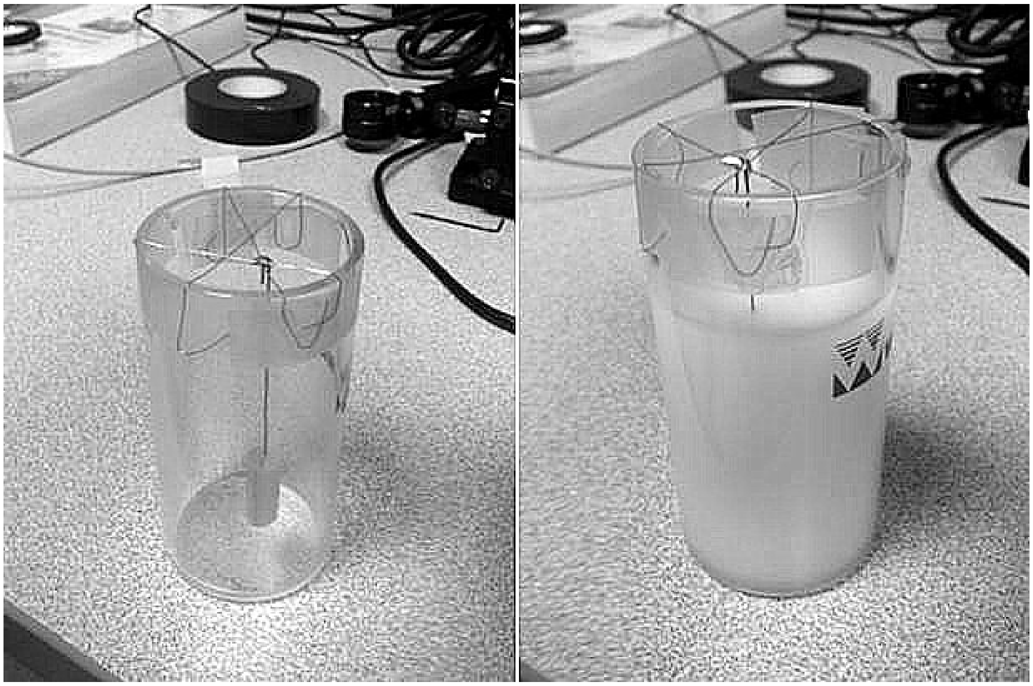

Figure 5.3 Lipofundin suspension and target contained in a beaker

The beaker with the suspension and target is placed onto the rotation stage shown in Figure 5.4. The configuration of the laser probes, the lipofundin background and the target is illustrated in Figure 5.5. The target position shown corresponds to the initial state during experiments.

Figure 5.4 The rotation stage with lightproof covering.

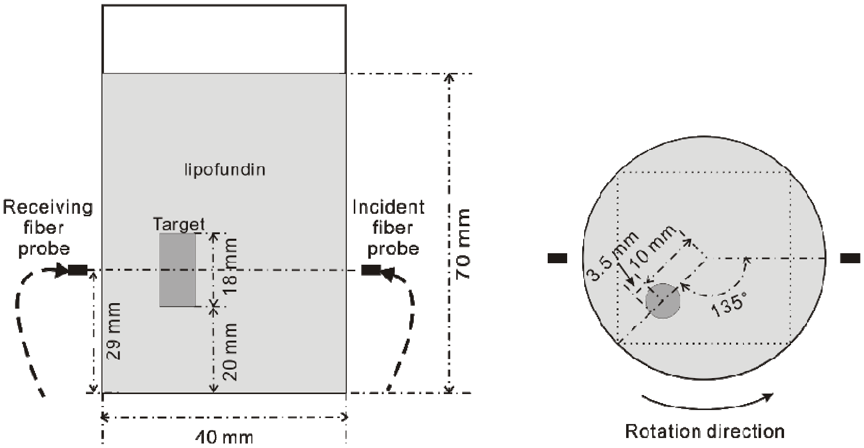

Figure 5.5 Configuration of laser probes, lipofundin sample and target.
Left, lateral view; right, vertical view.
The dash square in the vertical view corresponds to the image reconstruction area.

Upon illumination by the laser source, the diffuse photons from the lipofundin suspension are collected by another multimode optical fiber (core diameter~62.5 μm). To ensure optimal photon detection efficiency, this fiber is coupled to a collimator and the collimated light beam is focused by a lens (focal length~2 cm) to the active area (diameter~20 μm) of the SPC module.

The collimator, lens and the SPC module are placed in a lightproof box to minimize room light influence. To control the actual photon count rate of the detector, neutral density filters are placed between the collimator and the lens when needed.

The electrical pulses output by the detector representing the photon events are then added with proper DC offset and then recognized by the HRMTime timing module which continuously time-tags the rising edge of each single pulse. The time bin size is set to its minimum value of 27 ps. The pattern trigger signal, with a period of 32 times of the PRBS repetition time from the PRBS generator is amplified and taken by the timing module as a reference signal for synchronization. The time tags for both the photon pulses and the reference signal are continuously transferred to the PC, controlled by the LabVIEW program shown in Figure 4.15. The LabVIEW program accumulates the recorded photons to build up the signal arriving at the SPC detector, and then cross-correlates it with the original PRBS to retrieve the time spectrum of the detected photons.

5.3 Experimental procedure

During experiments, each time the rotation stage carrying the lipofundin suspension and target was manually rotated by 3° and the corresponding TPSF was measured. The rotation over 180° resulted in 61 TPSF measurements in total. The photon count rate detectable at the SPC detector was around 10^4 cps. To acquire around 1 million photons for each TPSF, we set the data acquisition time to 100 seconds. It is worthwhile to mention that the low count rate is specific to the experimental setup we used. The acquisition time can be much reduced if a large active area SPC detector is available. For example, a 200 μm SPC can help cut the TPSF acquisition time down to one second.

5.4 Image reconstruction results

As mentioned in the scope of this thesis, the phantom study in this chapter mainly aims for exploration of the potential applications of the PRSPC method, which is, in this chapter, to conduct real time time-resolved measurements of diffuse photons. The image reconstruction part is not a research objective of this study, thus only the basic procedure and algorithm are included here.

The image reconstruction was conducted in COMSOL/MATLAB environment. A 3D FEM forward model was built up in COMSOL Multiphysics 3.4 according to the geometry in Figure 5.5. Laplace domain diffusion equation and Laplace transformed TPSFs were used based on a Laplace parameter of 1.5 Gs^{-1}. For demonstration purpose, we only considered the 2D image for the slice at Z=29 mm, which is at the same height with the laser probes. Rytov approximation and Levenberg-Marquardt algorithm with positivity constraint were used to solve the inverse problem and to simultaneously reconstruct the absorption coefficients and the diffusion coefficients [128]. The inverse method was conducted in MATLAB. The optical properties of the model were updated for each iteration, and so were the forward model and forward solution in COMSOL. The images in Figure 5.6 are the reconstructed results after 5 times iteration. The images cover a transverse sectional area in which both x and y range from -1.4 cm to 1.4 cm. From Figure 5.6, we can see the reconstructed target position is not much different from its true position. The error could stem from modeling errors and/or measurement errors, e.g. the X-Y plane centre for the beaker and the rotation stage were not precisely overlapping. Within the reconstructed target area (represented by solid circle), the μ_a has a mean value of 0.0975 cm^{-1} and standard deviation of 0.0128 cm^{-1} whilst the μ_s' has a mean value of 5.4117 cm^{-1} and standard deviation of 1.7488 cm^{-1}, which are close to the true values (μ_a~0.1 cm^{-1}, μ_s'~8 cm^{-1}).

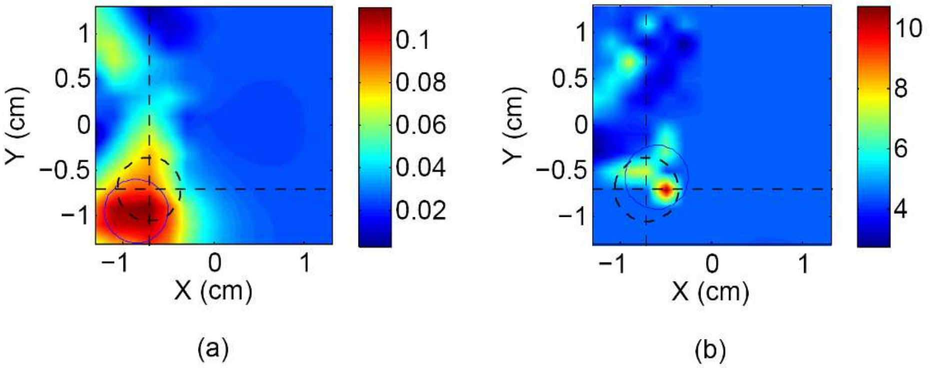

Figure 5.6 Reconstructed optical properties of the X-Y plane at Z=29 mm. The unit for the color bar is cm^{-1}. The dash circle represents the actual target position while the solid circle represents the reconstructed target position.
(a) for absorption coefficients and (b) for reduced scattering coefficients.

5.5 Summary and discussion

The lipofundin phantom based experiments demonstrate that the PRSPC system described in Chapter 4 is capable of fast acquisition of temporal profile of diffuse photons and has high potential in time-domain DOT systems. In addition, considering that the system uses a continuous wave laser instead of a pulsed laser, it has high potential to be easily integrated into a portable device.

As to image reconstruction, it is well known that it is far more challenging to reconstruct absorption and scattering coefficients simultaneously. From Figure 5.6(a), one can see that the reconstructed target is only slightly shifted from the true position while the reconstructed value is very close to the true value. The scattering image (Figure 5.6(b)) is of lower quality, but the peak value in the target region is not far from the true value.

Last, the experimental setup and procedure expatiated in this chapter can be further optimized in future studies. For instance, the large area single photon counter may be adopted to enhance the system sensitivity and to reduce the data acquisition time. Consequently, more measurements could be made and the image quality could be further improved.

Chapter 6 Blood glucose testing using time-resolved spectroscopy based on PRSPC method: a preliminary study

In this chapter, the PRSPC system developed in Chapter 4 was integrated into a time-resolved near infrared (NIR) spectroscopy system, which was used for preliminary studies on human blood sugar testing. Firstly, a brief review on human blood glucose testing will be in place. Secondly, the methodology and experimental system employed will be illustrated. Last, in vivo experimental results will be shown.

6.1 Blood glucose measurement

Diabetes mellitus is a chronic disease that occurs either when the pancreas does not produce enough insulin or when the body cannot effectively use the insulin it produces. Insulin is a hormone that regulates blood sugar. Hyperglycaemia, or raised blood sugar, is a common effect of uncontrolled diabetes and over time leads to serious damage to many of the body's systems, especially the nerves and blood vessels. Over time, diabetes can damage the heart, blood vessels, eyes, kidneys and nerves.

Some key facts related to diabetes are listed below [129]:

- More than 220 million people worldwide have diabetes.
- In 2005, an estimated 1.1 million people died from diabetes.
- At present there is no cure for diabetes.

- WHO projects that diabetes deaths will double between 2005 and 2030.
- Healthy diet, regular physical activity, maintaining a normal body weight and avoiding tobacco use can prevent or delay the onset of diabetes.

Self-monitoring and control of blood glucose by taking insulin is an integral part of diabetes mellitus therapy, as it can largely reduce the probability of various acute and chronic complications associated with diabetes. Most diabetic patients measure their blood glucose concentration several times a day to assess the effectiveness of their diet, exercise and medication. Compared to the widely used conventional blood glucose meters, continuous noninvasive glucose monitoring including the optical approaches, has drawn enormous attentions and extensive researches as it can provide prompt information of glucose level with improved patient comfort and compliance.

6.1.1 Invasive method

Improved technology for measuring blood glucose is rapidly changing the standards of care for diabetic people. There are several well developed invasive methods of blood glucose testing which use small blood samples usually taken from the fingertip, and two representatives are introduced below.

A visual test strip is a medium cost method for monitoring blood glucose. A drop of blood (≈20µl) which one obtains by lancing the finger is placed on a test zone on which the chemicals will react with the glucose in the blood and the changed color can be converted into readings. This method is suitable for prediabetic people who are not using insulin and are occasionally monitoring their blood glucose level. It is also an economic solution for people who can not afford test strips that are used in electronic meters, and for those who dislike electronic meters or who need a back up for their meter.

Another well developed invasive method is to use a blood glucose meter which is an electronic device for measuring the blood glucose level. A relatively small drop of blood is placed on a disposable test strip which interfaces with a digital meter. The level of blood glucose will be shown on the digital display within several seconds.

Recently, there was an advanced method which makes use of small blood drops for blood glucose testing from other places than the finger tips. While still using the same test strips and meter, this alternate sites testing practically reduces the pain, and gives the real estate on the finger tips a needed break if they became sore. The disadvantage of this technique, however, is that there is usually less blood flow to alternate sites, preventing the reading from being accurate when the blood sugar level is changing.

6.1.2 Non-invasive (NI) technologies

NI (AKA “transcutaneous”) diagnosis and monitoring of human blood glucose level have attracted tremendous attention since the 1980s because NI determination of glucose eliminates pain in the measurement process, has the potential for continuous measurement, allows tighter control of diabetes and delays the onset of diabetes complications and their associated health care costs.

It is now more than 20 years since the first report of the feasibility of NI glucose testing. Over this period, several potential alternatives have emerged [see review papers 130-132]. Some of them have been introduced as follows.

Photoaccoustic spectroscopy

The photoaccoustic spectroscopy (PAS) method [133-137] is based on ultrasonic waves created by tissue absorption of pulsed light. Upon illumination by laser beams, heat is generated in cells causing pressure variations in the sample. A piezoelectric transducer can be used to detect those acoustic signals with the specific incident wavelengths reflecting optical properties of glucose in blood. PAS non-invasive glycemic monitoring devices are already commercialized, e.g. the Aprise, from the Glucon company. Although this method was shown to correlate with blood sugar levels, the measurements are sensitive to chemical interferences from biological compounds and to physical interferences from the temperature and pressure changes. Thus it is still necessary to improve the reproducibility and sensitivity in order to decrease interferences from other substances.

Optical coherent tomography

Optical coherent tomography (OCT) has been proved to have the potential to monitor glucose-induced changes in tissues in vitro [138]. However, more research may be necessary to demonstrate the feasibility for in vivo blood glucose measurements.

Electromagnetic sensors

Electromagnetic sensors based on eddy currents are able to detect variation of the dielectric parameters of the blood caused by glucose concentration changes [139]. Studies also reported that even localized nuclear magnetic resonance has shown good performance to detect glycogen metabolism in the human brain [140].

Bioimpedance spectroscopy

Bioimpedance spectroscopy is a method that once was commercialized (Pendra, Pendragon) however exited market when Pendragon was closed in 2005 as this equipment was found suitable only for a small group of customers whose local dielectric skin characteristics show a minimum resonance frequency [141]. The equipment gathers information of a LC resonance circuit with the skin working as dielectric from the capacitor. One limitation of this research is that it requires the patient to rest for 60 min before testing [142].

Thermal emission spectroscopy

Thermal emission spectroscopy measures infra-red signals resulted from glucose concentration changes in human body. A prototype system uses similar concept as standard clinical tympanic membrane thermometers, with the addition of specific wavelengths for glucose fingerprint. The system was calibrated and tested in patients demonstrating reproducibility and predicting glucose concentrations with moderate error [143]. Such a system is sensitive to body movements and ambient temperature change.

Raman spectroscopy

Raman spectroscopy uses laser radiation sources from visible to the MIR range and measures very weak scattered light signals whose wavelengths are different from that of the exciting beam. Raman assays are not affected by interference from water as it has weak scattering indexes. Another advantage is that the resulting bands are narrow and have distinct peaks, allowing for easier separation of signals than in absorption spectroscopy [144,145]. M. Enejder et al. [146] reported the first successful study of the use of Raman spectroscopy for quantitative, noninvasive measurement of blood glucose. Their study, however, suffered from instability of the laser wavelength and intensity, and long spectra acquisition times.

Reverse iontophoresis

The method of iontophoresis utilizes electrical current to deliver charged drug compounds through the skin. NI glucose monitoring, however, uses transport of glucose in the opposite direction to that of normal medicaments and therefore is called ‘reverse iontophoresis’ [20]. The GlucoWatch monitor from Animas Technologies is a commercialized glucose control device manufactured utilizing such a technique with two independent potentiostat circuits [147]. The device makes use of the fact that glucose can be extracted through the epidermis surface via the electro-osmotic flow to the iontophoretic cathode, along with Na^+ ions. However, such a device is no longer available due to its unsatisfactory performance and other disadvantages including the time delay compared with blood values, skin irritation, inaccuracies of results, long calibration procedures and long warm-up period [148,149].

Near infrared (NIR) spectroscopy

NIR spectroscopy uses the near-infrared region of the electromagnetic spectrum (from about 800 nm to 2500 nm) and is based on molecular overtone and combination vibrations. Such transitions are forbidden by the selection rules of quantum mechanics. As a result, the molar absorptivity in the near IR region is typically quite small. One advantage is that NIR offers deeper penetration into tissue than mid infrared radiation. NIR spectroscopy is therefore very useful in probing bulk material with little or no sample preparation.

The molecular overtone and combination bands seen in the NIR are typically very broad, leading to complex spectra; it can be difficult to assign specific features to specific chemical components. Multivariate (multiple wavelength) calibrations (e.g., principal components analysis, partial least squares, or artificial neural networks) are the often employed techniques to extract the desired information. Careful development of a set of calibration samples and application of multivariate calibration techniques is essential for near-infrared analytical methods [150].

To date, among all the non-invasive blood glucose sensing methods, those employing NIR spectroscopy in tissues, like finger, lip, tough, etc. offer the most promising prospects [131,151-160]. However, due to the weak glucose signal compared to signals corresponding to other skin tissue components, body temperature change, and structure change in human tissue, few of the reported works provided sufficiently precise and accurate measurements for reliable clinical use [131].

A recently emerged technique named occlusion spectroscopy [161-168], however, showed a considerable promise for non-invasive monitoring of blood glucose. The major advance of this method is the use of an artificially induced time variance of optical transmission, i.e. the blood transparency instead of natural time variance of optical transmission used for pulse oximetiy. The time evolution of blood transparency is a rather strong signal and results in a high signal to noise ratio. Studies have shown the detailed behavior of the blood transparency following occlusion as a function of time is determined by the change of light scattering due to RBC aggregation, and thus contains rich information on: the volume fraction of scatterers (hematocrit), the mismatch of refraction indexes (glucose) and average absorption of whole blood (oxygen saturation) [162-165,169,170].

A device named NBM (Orsense Ltd.) utilizing this occlusion spectroscopy technique showed acceptable accuracy during in vitro and in vivo testing [171]. In vitro experiments applying in vivo-like algorithms showed a strong correlation between calculated and actual glucose concentrations despite the presence of physiological interferences. A Clarke error grid analysis of the in vivo clinical study showed that 95.5% of the measurements fall within the clinically acceptable A&B regions (zone A, 69.7%; and zone B, 25.7%).

6.2 The PRSPC based occlusion spectroscopy method

The method of occlusion spectroscopy starts with occlusion caused blood flow cessation in a human finger realized by applying an over-systolic pressure to fingertip and continuous observation of the transmission light signal, i.e. the blood transparency. Figure 6.1 shows the transmission signal of a human finger when illuminated by a 980nm laser source whose output power is 2.2 mW. The occlusion occurred at t=22s.

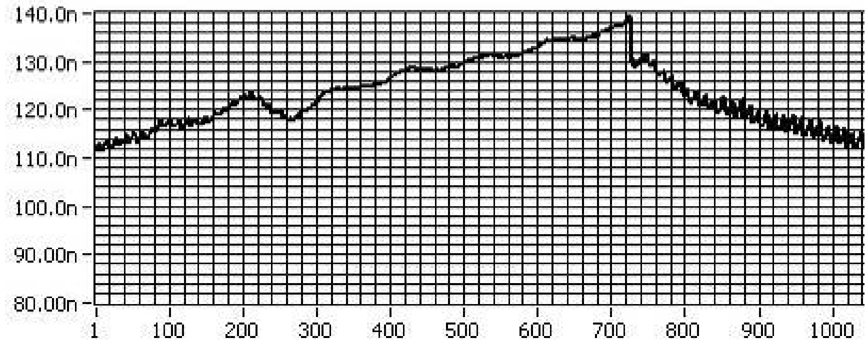

Figure 6.1 Blood transparency observed following occlusion. X-axis stands for time (unit 0.1s) and Y-axis for transmission signal power (unit watt).

In this part of work, instead of continuous recording of the transmission power, the PRSPC system was used to measure the temporal profiles of diffuse photons (transmission mode) at several time delays following occlusion. A detailed comparison of the data acquisition and processing procedures following occlusion employed in the reported occlusion spectroscopy method and the PRSPC based occlusion spectroscopy method is included below:

- **Reported occlusion spectroscopy method [165]**

I. Record $T(\lambda_1, t)$ and $T(\lambda_{ref}, t)$ simultaneously, which stand for the transmission signals following occlusion for the two wavelengths used. Here, λ_1 =637nm and λ_{ref} =940nm. The choice of 940nm is because there is no practical glucose influence on the transmission evolution curves for the wavelength 940nm. Thus it is employed as the reference wavelength [162-164,172].

II. Calculate *CP* (calculated parameter) at multiple time delays, where

$$CP = (d(LogT(\lambda_1))/dt)/(d(LogT(\lambda_{ref}))/dt)$$

It has been proved [165] that the mathematical meaning of *CP* is similar to the parameter called γ, widely used in pulse-oximetry. For pulsatile transmission signal it is defined as:

$$\gamma = \frac{\delta(T(\lambda_1, t))/T(\lambda_1)}{\delta(T(\lambda_{ref}, t))/T(\lambda_{ref})}$$

To calculate $\delta(T(\lambda))$, appropriate signal processing procedure is required to reduce all unrelated alterations of the signal. γ is practically unaffected by varying factors of the human body, such as local blood volume, blood hematocrit, measurement geometry and thickness of skin and pigmentation. This means γ depends on absorption and scattering properties of the measured blood only, rendering the value of γ extremely valuable and of high practical and theoretical importance.

CP is equivalent to γ under small signal fluctuations. Hence, it has been suggested that the *CP* of post-occlusion signal, analogous to γ, is resistant to non-blood related interferences.

III. Average the *CP*s at different time delays to generate one averaged experimental *CP*. Real glucose level is measured from a blood glucose meter.

The above steps are repeated in clinical trials. The recorded experimental *CPs* are plotted as a function of the corresponding blood glucose meter readings (G) to see the dependence of *CP* on *G*.

- **PRSPC based occlusion spectroscopy**

I. For both the two wavelengths used, measure the TPSFs of the diffuse transmittance signal at t=-15s, t=3s, t=21s and t=39s (occlusion occurs at t=0s).

II. Convert the time domain measurements to Laplace domain. Calculate the Laplace transformed value for each TPSF:

$$F_{T_i}(\lambda, S_j) = \int_0^\infty I_{T_i}\ (\lambda, t) e^{-S_j t} dt$$

Here $I_{T_i}\ (\lambda, t)$ is the measured TPSF at a certain time delay T_i after occlusion where *i*=1, 2, 3 or 4, corresponding to the 4 time delays in Step I with *i*=1 for the earliest. λ has two values λ_1 =850nm and λ_{ref} =980nm, where the 980nm wavelength is utilized as a substitute for the recommended reference wavelength of 940nm. $F_{T_i}(\lambda, S_j)$ is the Laplace transformed value of $I_{T_i}\ (\lambda, t)$ with a Laplace parameter of S_j.

III. Generate a parametric slope (*PS*). Firstly define two arrays X and Y, where X is composed of the 4 Laplace values for λ_{ref} and Y is composed of the 4 Laplace values for λ_1. In MATLAB codes:

$$\text{X=[} F_{T_1}(\lambda_{ref}, S_j)\,; F_{T_2}(\lambda_{ref}, S_j)\,; F_{T_3}(\lambda_{ref}, S_j)\,; F_{T_4}(\lambda_{ref}, S_j)\,\text{];}$$

$$\text{Y=[} F_{T_1}(\lambda_1, S_j)\,; F_{T_2}(\lambda_1, S_j)\,; F_{T_3}(\lambda_1, S_j)\,; F_{T_4}(\lambda_1, S_j)\,\text{];}$$

Secondly, assume linear relationship of X and Y:

$$Y=A1\times X+A0$$

and use the linear fitting function in MATLAB to find A1, i.e. the parametric slope *PS*.

The above steps are repeated. The acquired experimental *PS*s are plotted as a function of the corresponding blood glucose meter readings to see the dependence of *PS* on G.

6.3 Experimental system and measurement procedure

The experimental system was built based on the scheme shown in Figure 4.1. The output from the PRBS generator is evenly split by a power splitter (Mini Circuits, ZFSC-2-2500) and used to modulate the two transmitters. Figure 6.2 and Figure 6.3 show the arrangement of the optical transmitters and receiver (SPC detector) inside the lightproof box. The label ‘A’ indicates the self-made 980nm VCSEL transmitter, ‘B’ for the output from the 850nm transmitter (see 4.3.1.1), ‘C’ for the light guide to direct the modulated laser beam to human finger surface and ‘D’ for the light guide to direct the diffused photons through finger to the SPC detector (E). The illumination by the two wavelengths is carried one by one. This is realized by utilizing a 2×2 latching-type optical switch (OSW-2×2-1300-62.5-L-1-FP) and a DAQ card (NI USB-6212). The LabVIEW program performing this function is included in appendix A.2.3.1.

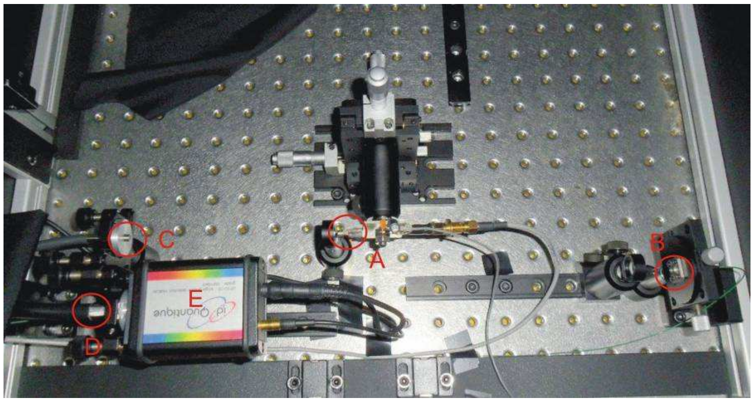

Figure 6.2 Alignment of the optical transmitters and receiver.

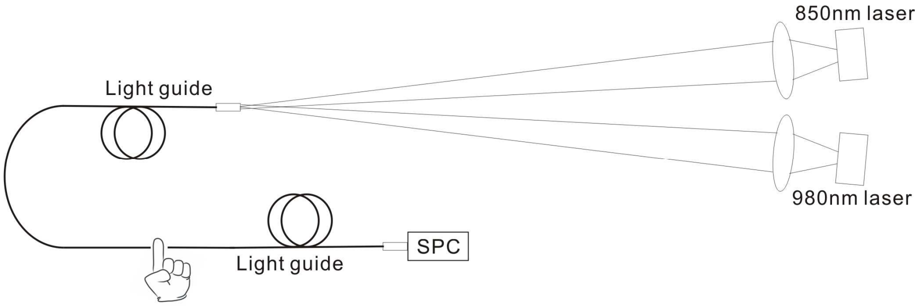

Figure 6.3 Optical diagram

Figure 6.4 shows the finger holder and the occlusion arrangement. The occlusion is realized by applying an over-systolic pressure (around 180mmHg, monitored on a computer) to the upper arm through a blood pressure cuff. The thin light guide directs the incident light beam onto the index finger pulp and the thick light guide directs the diffused photons to the detector. To ensure consistent condition during experiments and get rid of motion artifacts, the finger’s position is marked for each subject while the contact pressure between the finger pulp and the glass window covering the light guide is maintained by monitoring through a pressure sensor (see bottom right of Figure 6.4). Details of the pressure sensor configuration and software control can be found in appendix A.4.3 and A.2.1 respectively.

Figure 6.4 Finger holder and occlusion arrangement

6.4 Results and discussion

As illustrated in sub-section 6.2, each occlusion measurement includes one experimental *PS* for a preset Laplace parameter and a reference glucose level G. For the 6 human subjects examined, totally 24 occlusion measurements were conducted. However, instead of one single preset Laplace parameter, several Laplace parameters were used in the data processing process. The measurement accuracy of the system was examined for each Laplace parameter chosen and the optimal Laplace parameter was determined.

Shown in Figure 6.5-Figure 6.9 are the results of the dependence of *PS* on G for five Laplace parameters, namely 0, 0.5, 1, 1.5 and 2 Gs^{-1}. The different symbols in the figures represent different human subjects. For each Laplace parameter, the corresponding figure is obtained as follows:

1) Each occlusion measurement gives one *PS*, with the goodness of fitting tested by calculating the coefficient of determination R^2. If $R^2<0.7$, the fitting is considered to be bad and the measurement is considered invalid. Outlier values of *PS* are also considered invalid measurements.

2) Plot the valid *PS*s as a function of G. A second linear fitting is conducted with these valid measurements. The dependence of *PS* on G and the coefficient of determination R^2 are determined.

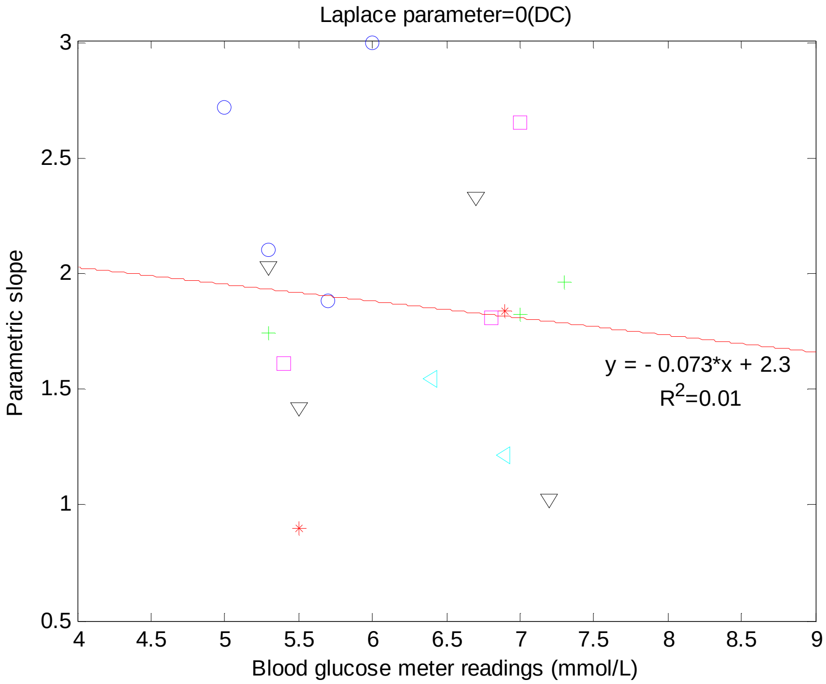

Figure 6.5 Dependence of *PS* on glucose level and the linear fitting result (DC).
A plot of 18 valid measurements. Different symbols stand for different human subjects.

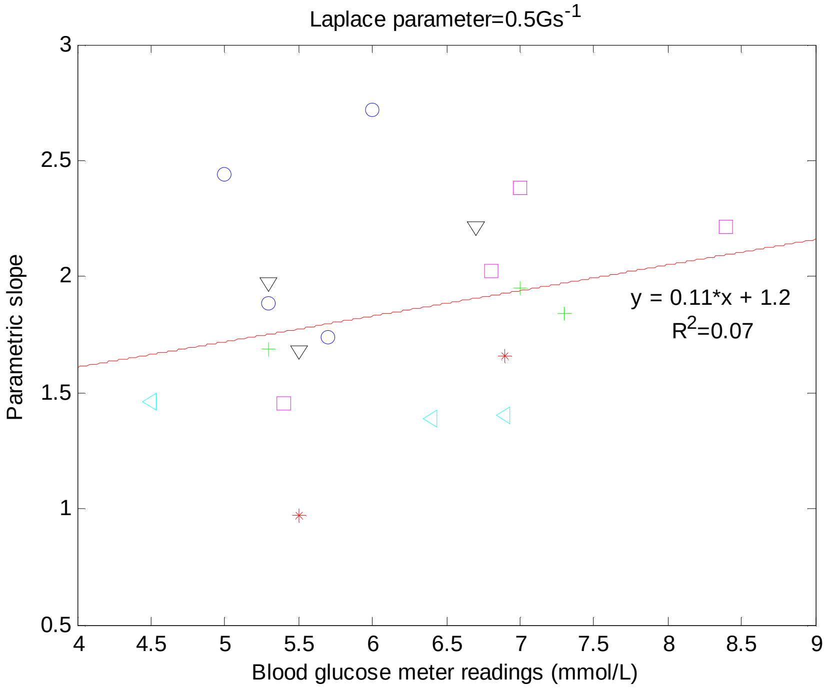

Figure 6.6 Dependence of *PS* on glucose level and the linear fitting result (0.5Gs^{-1}).
A plot of 19 valid measurements. Different symbols stand for different human subjects.

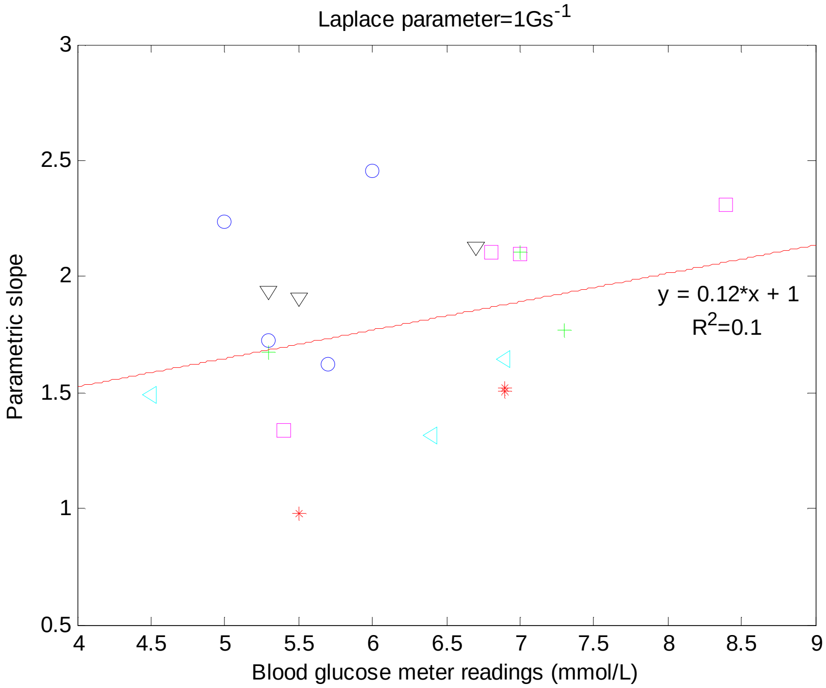

Figure 6.7 Dependence of *PS* on glucose level and the linear fitting result (1Gs^{-1}).
A plot of 20 valid measurements. Different symbols stand for different human subjects.

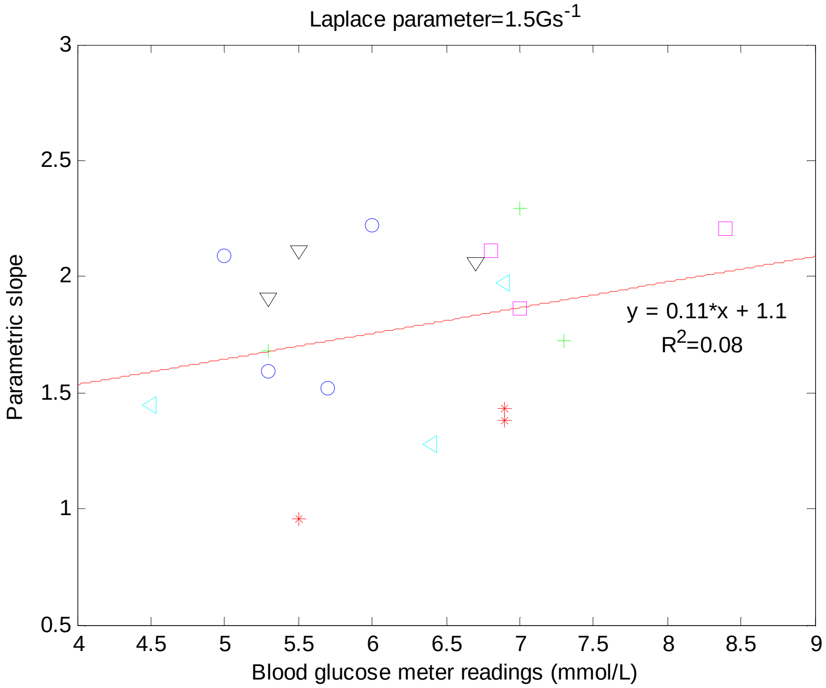

Figure 6.8 Dependence of *PS* on glucose level and the linear fitting result (1.5Gs^{-1}).
A plot of 19 valid measurements. Different symbols stand for different human subjects.

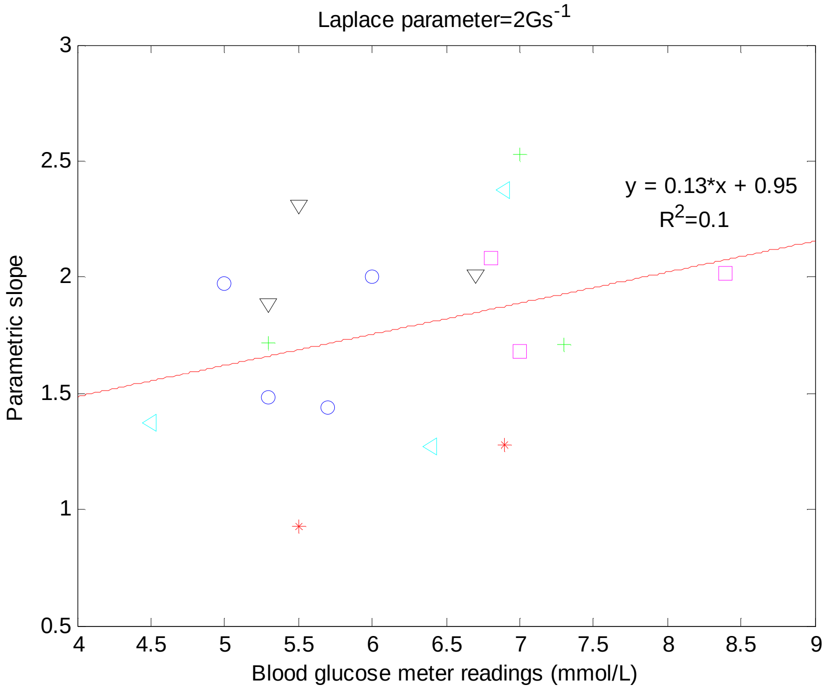

Figure 6.9 Dependence of *PS* on glucose level and the linear fitting result (2Gs^{-1}).
A plot of 18 valid measurements. Different symbols stand for different human subjects.

It can be seen that a Laplace parameter of 1 Gs^{-1} gives the most number of valid measurements (20 out of 24) and the best goodness of fitting (R^2=0.1) for the valid measurements. This indicates that the Laplace parameter should be set to 1Gs^{-1} in this experiment (complying with the conclusion in 4.4.3.2), in order to achieve best measurement accuracy.

Same as Figure 6 in [165], the ascending dependence *PS*(G) revealed in Figure 6.7 is in qualitative agreement with theoretical predictions [162-164]. In Figure 6.7, the ascending dependence of *PS*(G) is clear for each subject involved. However, it is evident that the fitting result involving all subjects has larger residual values and lower coefficient of determination. This is most likely attributed to the fact that the subjects involved in this study have larger variation of hemoglobin levels than those involved in [165]. The rationale is the following: the information regarding all three parameters (hemoglobin, glucose and saturation) are extracted from the same set of occlusion curves, which means they are inter-dependent. To get rid of the inter-dependence of hemoglobin, glucose and saturation, two arrangements were adapted [165], including the use of 940nm as the reference wavelength and selecting patients with a low variation of hemoglobin values for the clinical trial. The hemoglobin values for the 6 volunteers involved in this study, however, were not measured before experiments and probably may not have a low variation. The consequence is that the dependence *PS*(G) shown in Figure 6.7 may contain information regarding glucose but also the hemoglobin level.

It is well known that the glucose level is positively correlated with the refractive index of blood serum [173,174]. As glucose level increases, the refractive index mismatch Δn between scatters (RBC and RBC aggregates) and medium (blood serum) becomes smaller. According to the linear relationship given in [174]: $d\Delta n / dG = -1.515 \times 10^{-6}\, dl / mg$, the whole range of possible physiological changes of glucose $G \in (50mg/dl, 600mg/dl)$ leads to a rather small range of $\Delta n \sim 1\% n_0$, where n_0 is the refractive index of the blood serum. However, the dependence *CP*(G) may be stronger [164]. The dependence *PS*(G) generated from this experiment also shows clear positive correlation between *PS* and G, which validates the occlusion spectroscopy method in a time-resolved approach.

Nevertheless, the experimental system and measurement procedure still have potential to improve:

- The 980nm reference wavelength is close to the recommended 940nm, but it is certainly not a perfect substitute. To refine the experimental results, a 940nm or other recommended value should be used for the reference wavelength.

- The current finger holder setup allows loose contact of finger with the glass window in front of the light guide. If the position of the finger can be fixed during testing, the motion artifacts may be further reduced.

- The occlusion action is performed by squeezing air through the pump connected to the blood pressure cuff. It usually takes about 4-6 seconds to reach the desired pressure (around 180mmHg). This non-standardized procedure may introduce inconsistency in the testing conditions as the time taken to occlude the blood and the final pressure applied to the blood vessel may have slight variations. If the occlusion action can be conducted using a 1-click device like the device involved in [165], the improved consistency of testing conditions may help to obtain better experimental results.

- The absorption by water is very strong at the wavelength 980nm, which causes low transmission photon count rate (low blood transparency). To acquire enough photons, the acquisition time for 980nm is set to be 8 seconds to collect around 0.5M photons. Limited by the long acquisition time, the current experimental system allows 3-4 TPSF acquisitions within 40 seconds after occlusion takes place. The photon count rate can be higher by replacing the 980nm VCSEL transmitter by one of other wavelengths where absorption by water is low. In this way, the system should allow more TPSF acquisitions after occlusion, possibly leading to more accurate parametric slopes.

Chapter 7 Conclusions

7.1 Conclusions

The first objective of this study was to validate a new time-resolved optical measurement method termed pseudo-random single photon counting (PRSPC). The computer based simulations proved that the PRSPC method can be used to conduct time-resolved measurements. The retrieved temporal profile by using PRSPC method was in well agreement with the original input of the simulation. The PRSPC prototype validated the method experimentally. The calibration experiments gave a system response of 150ps (20%-80% rise time). The phantom based experiments qualitatively proved that the method is able to identify small changes in optical properties (absorption and/or scattering) of the sample. This part of work laid the foundation for the following studies.

The second objective of this thesis was to design, implement, optimize and evaluate a high speed PRSPC system, which can be integrated into a time resolved diffuse optical imaging system or other time resolved optical techniques. Emphasis was placed on achieving optimal temporal resolution and fast data acquisition speed. The finalized PRSPC system can reach a photon count rate of 3Mcps, limited by the data processing time taken by LabVIEW program and the maximum count rate (4.5 Mcps) allowed by the HRMTime module. The system calibration result in sub-section 4.4.2 shows a 20%-80% rise time of 130 ps and a full width at half maximum about 260ps. The short rise time indicates that this PRSPC system can achieve a high time resolution. The establishment of this PRSPC system provides a valuable alternative approach in conducting time-resolved measurements, as it does not sacrifice much operating performance compared with TCSPC yet achieves higher photon count rate and faster data acquisition. Besides, the PRSPC system also offers portability and low cost, which are not with TCSPC.

The third objective was to explore the potential of the high speed PRSPC system in time-resolved diffuse optical imaging. The lipofundin phantom based experiments demonstrated that the PRSPC system described in Chapter 4 is capable of fast acquisition of temporal profiles of diffuse photons and has high potential in time-domain DOT systems. In addition, considering that the system uses a continuous wave laser instead of a pulsed laser, it is readily available to be integrated into a portable device. In the reconstructed image Figure 5.6(a), the reconstructed target is only slightly shifted from the true position while the reconstructed value is very close to the true value. The scattering image (Figure 5.6(b)) is of lower quality, but the peak value in the target region is not far from the true value.

The fourth objective was to explore the potential of the PRSPC method in time-resolved spectroscopic applications. The PRSPC system was combined with occlusion spectroscopy for human blood glucose testing studies. The experiments adopted the basic principle of occlusion spectroscopy to make use of the time evolution of blood transparency following prolonged cessation of blood in human finger, but different measurement and data processing procedures. The experimental results of 6 volunteer subjects (Figure 6.5) showed good qualitative agreement with theoretical prediction. This part of work demonstrated that a time-resolved occlusion spectroscopy method is possible and has potential to generate research significance.

7.2 Recommendations for future work

The following aspects are recommended for future research, which can help either improve the performance of the PRSPC system or lead to possible new scientific findings:

- The electrical components are a major source of the noise level in the PRSPC system. Damping noise by optimizing the electrical design could help improve the signal to noise ratio. The RF components, such as the power splitter, bias tee and amplifier may introduce jitter into the electrical signal. Although necessary shields have been used to reduce the jitter, better performing substitutes are still in need to further reduce the noise level.

- The LabVIEW program is the most significant factor limiting the maximum count rate that is reachable by the PRSPC system. Thus an important aspect of future work would be to improve the efficiency of the LabVIEW program so that the data processing can be faster and a higher photon count rate can be reached.

- The current PRSPC system features single source-detector pair. Although time-resolved diffuse optical imaging experiments were conducted using this system, the low scanning speed is a main obstacle to realize real time imaging. An interesting future direction thus can be to design and implement a source-detector array and integrate with the current PRSPC system. The higher time resolution may probably result in higher spatial resolution for the reconstructed image compared with the reported work based on the SSTR method.

- The in vivo blood glucose testing in Chapter 6 resulted in qualitative agreement of the experimental result with theoretical prediction. For establishment of quantitative correlation between the experimental *PS* and glucose meter reading, however, extensive future work is a mandate. Firstly, sufficient human subjects must be recruited following relevant protocol. The second step is to group the subjects according to the method reported in [165] and conduct the experiments described in Chapter 6 to obtain enough data points, e.g. 30 for each group. Thereafter, the quantitative correlation is to be extracted from the data points. Finally, this quantitative relationship will be applied to the existing experimental procedure for derivation of experimental glucose levels. Statistical analysis should be conducted to analyze the accuracy of the whole process, i.e. the PRSPC based occlusion spectroscopy method.

Bibliography

1. M. S. Patterson, B. Chance, and B. C. Wilson, "Time resolved reflectance and transmittance for the noninvasive measurement of tissue optical properties," Appl. Opt. **28**, 2331-2336 (1989)

2. J.R. Lakowicz, H. Szmacinski, K. Nowaczyk, K.W. Berndt and M. Johnson, "Fluorescence lifetime imaging," Anal. Biochem. **202**, 2, 316-330 (1992)

3. P. I. H. Bastiaens and A. Squire, “Fluorescence lifetime imaging microscopy: spatial resolution of biochemical processes in the cell,” Trends Cell Biol. **9**, 2, 48-52 (1999).

4. Hielscher, A.H., Klose, A.D. and Hanson, K.M., “Gradient-based iterative image reconstruction scheme for time-resolved optical tomography,” Medical Imaging, IEEE Transactions on, **18**(3), 262 – 271 (1999)

5. C. V. Shank, R. Yen, and C. Hirlimann, “Time-Resolved Reflectivity Measurements of Femtosecond-Optical-Pulse-Induced Phase Transitions in Silicon,” Phys. Rev. Lett. **50**, 454–457 (1983)

6. Rick Trebino, Kenneth W. DeLong, David N. Fittinghoff, John N. Sweetser, Marco A. Krumbügel, Bruce A. Richman and Daniel J. Kane, “Measuring ultrashort laser pulses in the time-frequency domain using frequency-resolved optical gating,” Rev. Sci. Instrum. **68**, 3277 (1997)

7. Jeremy C. Hebden, Hylke Veenstra, Hamid Dehghani, Elizabeth M. C. Hillman, Martin Schweiger, Simon R. Arridge and David T. Delpy, “Three-dimensional time-resolved optical tomography of a conical breast phantom,” Appl. Opt. **40**, 3278-3287 (2001)

8. Hideo Eda, Ichiro Oda, Yasunobu Ito, Yukihisa Wada, Yukio Oikawa, Yoshio Tsunazawa, Michinosuke Takada, Yutaka Tsuchiya, Yutaka Yamashita, Motoki Oda, Angelo Sassaroli, Yukio Yamada and Mamoru Tamura, “Multichannel time-resolved optical tomographic imaging system,” Rev. Sci. Instrum. **70**, 3595 (1999)

9. A. A. Oraevsky, S. L. Jacques, and F. K. Tittel, "Measurement of tissue optical properties by time-resolved detection of laser-induced transient stress," Appl. Opt. **36**, 402-415 (1997)

10. Alwin Kienle and Michael S. Patterson, "Improved solutions of the steady-state and the time-resolved diffusion equations for reflectance from a semi-infinite turbid medium," J. Opt. Soc. Am. A **14**, 246-254 (1997)

11. F. Gao, H. J. Zhao, and Y. Yamada, “Improvement of Image Quality in Diffuse Optical Tomography by use of Full Time-Resolved Data,” Appl. Opt. **41**, 778-791 (2002).

12. F. Gao, P. Poulet, and Y. Yamada, “Simultaneous mapping of absorption and scattering coefficients from a three dimensional model of time-resolved optical tomography”, Appl. Opt. **39,** 5898-5910 (2000)

13. Feng Gao, Yukari Tanikawa, Huijuan Zhao, and Yukio Yamada, "Semi-Three-Dimensional Algorithm for Time-Resolved Diffuse Optical Tomography by Use of the Generalized Pulse Spectrum Technique," Appl. Opt. **41**, 7346-7358 (2002)

14. Steen J. Madsen, Brian C. Wilson, Michael S. Patterson, Young D. Park, Steven L. Jacques, and Yaron Hefetz, "Experimental tests of a simple diffusion model for the estimation of scattering and absorption coefficients of turbid media from time-resolved diffuse reflectance measurements," Appl. Opt. **31**, 3509-3517 (1992)

15. Huijuan Zhao, Feng Gao, Yukari Tanikawa, Kazuhiro Homma, and Yukio Yamada, "Time-resolved diffuse optical tomographic imaging for the provision of both anatomical and functional information about biological tissue," Appl. Opt. **44**, 1905-1916 (2005)

16.Bruno Montcel, Renee Chabrier, and Patrick Poulet, "Detection of cortical activation with time-resolved diffuse optical methods," Appl. Opt. **44**, 1942-1947 (2005)

17. M. Essenpreis, C. E. Elwell, M. Cope, P. van der Zee, S. R. Arridge, and D. T. Delpy, "Spectral dependence of temporal point spread functions in human tissues," Appl. Opt. **32**, 418-425 (1993).

18. C. Zint, W. Uhring, M. Torregrossa, B. Cunin, and P. Poulet, "Streak Camera: A Multidetector for Diffuse Optical Tomography," Appl. Opt. **42**, 3313-3320 (2003).

19. W. Becker, A. Bergmann, M.A. Hink, K. König, K. Benndorf, C. Biskup, "Fluorescence lifetime imaging by time-correlated single-photon counting," Microsc. Res. Tech. **63**, 1, 58-66 (2004).

20. “Basic Principle of the Single Photon Counting Lifetime Measurement,” in Time-correlated single photon counting, D.V. O'Connor, D. Phillips (Academic, 1984), pp. 36-54.

21. B. Tromberg, A. Cerussi, N. Shah, M. Compton, A. Durkin, D. Hsiang, J. Butler, and R. Mehta, "Imaging in breast cancer: Diffuse optics in breast

cancer: detecting tumors in pre-menopausal women and monitoring neoadjuvant chemotherapy," Breast Cancer Research **7**, 279 - 285 (2005).

22. J. Hebden, T. Yates, A. Gibson, N. Everdell, S. Arridge, D. Chicken, M. Douek, and M. S. Keshtgar, "Monitoring recovery after laser surgery of the breast with optical tomography: a case study," Appl. Opt. **44**, 1898-1904 (2005).

23. H. Zhao, F. Gao, Y. Tanikawa, and Y. Yamada, "Time-resolved diffuse optical tomography and its application to in vitro and in vivo imaging," Journal of Biomedical Optics **12**, 062107-062113 (2007).

24 . G. Boverman, Q. Fang, S. A. Carp, E. L. Miller, D. H. Brooks, J. Selb, R. H. Moore, D. B. Kopans, and D. A. Boas, "Spatio-temporal imaging of the hemoglobin in the compressed breast with diffuse optical tomography," Phys. Med. Biol. **52,** 3619-3641 (2007).

25 . J. Hebden, and T. Austin, "Optical tomography of the neonatal brain," European Radiology, **17,** 2926-2933 (2007).

26 . J. C. Hebden, D. J. Hall, M. Firbank and D. T. Delpy, "Time-resolved optical imaging of a solid tissue-equivalent phantom," Appl. Opt. **34,** 8038 (1995).

27 . S. V. Patwardhan, and J. P. Culver, "Quantitative diffuse optical tomography for small animals using an ultrafast gated image intensifier," Journal of Biomedical Optics, **13,** 011009-011007 (2008).

28 . A. Gibson, R. M. Yusof, H. Dehghani, J. Riley, N. Everdell, R. Richards, J. C. Hebden, M. Schweiger, S. R. Arridge, and D. T. Delpy, "Optical Tomography of a Realistic Neonatal Head Phantom," Appl. Opt. **42,** 3109-3116 (2003).

29 . V. Y. Soloviev, K. B. Tahir, J. McGinty, D. S. Elson, M. A. A. Neil, P. M. W. French, and S. R. Arridge, "Fluorescence lifetime imaging by using time-gated data acquisition," Appl. Opt. **46,** 7384-7391 (2007).

30 . A.A. Heikal, W.W. Webb, "One- and two-photon time-resolved fluorescence spectroscopy of selected fluorescent markers: photobleaching, triple-, and singlet-state dynamics," Biophys. J. **73,** 260 (1999)

31 . A.A. Heikal, S.T. Hess, G.S. Baird, R.Y. Tsien and W.W. Webb, "Molecular spectrocopy and dynamics of intrinsically fluorescent proteins: Coral red (dsRed) and yellow (Citrine)," PNAS **97,** 11996-12001 (2000)

32. A. Málnási-Csizmadia, M. Kovács, R.J. Woolley and S.W. Botchway, "The dynamics of the relay loop tryptophan residue in the dictyostelium

myosin motor domain and the origin of spectrocopic signals," J. Biol. Chem. **276** 19483-19490 (2001)

33. M.J.B. Pereira, D. A. Harris, D. Rueda, N.G. Walter, "Reaction pathway of the trans-acting hepatitis delta virus ribozyme: A conformational change accompanies catalysis," Biochemistry **41** 730-740 (2002)

34. W. Becker, H. Hickl, C. Zander, K.H. Drexhage, M. Sauer, S. Siebert and J. Wolfrum, "Time-resolved detection and identification of single analyte molecules in microcapillaries by time-correlated single photon counting," Rev. Sci. Instrum. **70**, 1835-1841 (1999)

35. M. Prummer, C. Hübner, B. Sick, B. Hecht, A. Renn and U. P. Wild, "Single-Molecule Identification by Spectrally and Time-Resolved Fluorescence Detection," Anal. Chem. **72**, 433-447 (2000)

36. C. Zander, K.H. Drexhage, K. T. Han, J. Wolfrum and M. Sauer, "Single-molecule counting and identification in a microcapillary," Chem. Phys. Lett. **286** 457-465 (1998)

37. P. Schwille, S. Kummer, A.A. Heikal, W.E. Moerner, and W.W. Webb, "Fluorescence correlation spectroscopy reveals fast optical excitation-driven intramolecular dynamics of yellow fluorescent proteins," PNAS, **97**, 151-156 (2000)

38. M. Sauer, B. Angerer, W. Ankenbauer, Z. Földes-Papp, F. Göbel, K. -T. Han, R. Rigler, A. Schulz, J. Wolfrum and C. Zander, "Single molecule DNA sequencing in submicrometer channels: state of the art and future prospects," J. Biotechnol. **86**, 3, 181-201 (2001)

39. J. P. Knemeyer, N. Marmé, and M. Sauer, "Probes for Detection of Specific DNA Sequences at the Single-Molecule Level," Anal. Chem. **72**, 3717-3724 (2000)

40. W. Becker, A. Bergmann, H. Wabnitz, D. Grosenick and A. Liebert, "High count rate multichannel TCSPC for optical tomography," Proc. SPIE. **4431**, 249-254 (2001)

41. D. Grosenick, H. Wabnitz, H. Rinneberg, K.Th. Moesta and P. Schlag, "Development of a time-domain optical mammograph and first in-vivo applications," Appl. Opt. **38**, 2927-2943 (1999)

42. R. Cubeddu, A. Pifferi, P. Taroni, A. Torricelli and G. Valentini, "Compact tissue oximeter based on dual-wavelength multichannel time-resolved reflectance," Appl. Opt. **38**, 3670-3680 (1999)

43. H.-G. Eberle, J. Beuthan, G. Müller, "The propagation of ps-laser-pulses

through different bone structure," Z. Med. Phys. **10**, 177-183 (2000)

44. P. Poulet, C.V.Zint, M. Torregrossa, W. Uhring, B. Cunin, "Comparison of two time-resolved detectors for diffuse optical tomography: Photomultiplier tube - time-correlated single photon counting and multichannel streak camera," Proc.SPIE. **4955**, 154-163 (2003)

45. B. J. Bacskai, J. Skoch, G. A. Hickey, R. Allen, and B. T. Hyman, "Fluorescence resonance energy transfer determinations using multiphoton fluorescence lifetime imaging microscopy to characterize amyloid-beta plaques," J. Biomed. Opt. **8**, 3, 368 (2003)

46. H. J. Youn, E. Terpetschnig, H. Szmacinski and J. R. Lakowicz, "Fluorescence Energy Transfer Immunoassay Based on a Long-Lifetime Luminescent Metal–Ligand Complex," Anal. Biochem. **232**, 24-30 (1995)

47. J. P. Culver, R. Choe, M. J. Holboke, L. Zubkov, T. Durduran, A. Slemp, V. Ntziachristos, B. Chance, and A. G. Yodh. "Three-dimensional diffuse optical tomography in the parallel plane transmission geometry: Evaluation of a hybrid frequency domain/continuous wave clinical system for breast imaging." Med. Phys. **30**, 235–247 (2003).

48. H. Dehghani, B.W. Pogue, S. D. Jiang, B. Brooksby, and K. D. Paulsen. "Three-dimensional optical tomography: resolution in small-object imaging." Appl. Opt. **42**, 3117–3128 (2003).

49. M. A. Franceschini, K. T. Moesta, S. Fantini, G. Gaida, E. Gratton, H. Jess,W.W. Mantulin, M. Seeber, P. M. Schlag, and M. Kaschke. "Frequency-domain techniques enhance optical mammography: Initial clinical results." Proc. Natl. Acad. Sci. U. S. A. **94**, 6468–6473 (1997).

50. G. Gesztelyu, W. Finnegan, J. A. DeMaro, J. Y. Wang, and J. L. Chen. "Parenchymal microvascular systems and cerebral atrophy in spontaneously hypertensive rats." Brain Res. **611**, 249–257 (1993).

51. X. J. Gu, Q. Z. Zhang, M. Bartlett, L. Schutz, L. L. Fajardo, and H. B. Jiang. "Differentiation of cysts from solid tumors in the breast with diffuse optical tomography." Acad. Radiol. **11**, 53–60 (2004).

52. H. Jiang, Y. Xu, N. Ifitimia, J. Eggert, K. Klove, L. Baron, and L. Fajardo. "Threedimensional optical tomographic imaging of breast in a human subject." IEEE Trans. Med. Imaging **20**, 1334–1340 (2001).

53. A. Pifferi, P. Taroni, A. Torricelli, F. Messina, R. Cubeddu, and G. Danesini. "Fourwavelength time-resolved optical mammography in the 680-980-nm range." Opt. Lett. **28**, 1138–1140 (2003).

54. B. W. Pogue, S. P. Poplack, T. O. McBride, W. A. Wells, K. S. Osterman, U. L. Osterberg, and K. D. “Paulsen. Quantitative hemoglobin tomography with diffuse near-infrared spectroscopy: Pilot results in the breast.” Radiology **218**, 261–266 (2001).

55. Q. I. Zhu, M. M. Huang, N. G. Chen, K. Zarfos, B. Jagjivan, M. Kane, P. Hedge, and S. H. Kurtzman. “Ultrasound-guided optical tomographic imaging of malignant and benign breast lesions: Initial clinical results of 19 cases.” Neoplasia **5**, 379–388 (2003).

56. T. Durduran. “Non-invasive measurements of tissue hemodynamics with hybrid diffuse optical methods.” Ph.D. disseration University of Pennsylvania (2004).

57. J. R. Kappa, H. D. Berkowitz, R. Seestedt, and B. Chance. “Evaluation of calf muscle oxygen content using NIRS in patients with peripheral vascular disease.” Medical intelligence unit: vascular surgery 2000, 10–16. (1991).

58. V. Quaresima, M. Ferrari, M. A. Franceschini, M. L. Hoimes, and S. Fantini. “Spatial distribution of vastus lateralis blood flow and oxyhemoglobin saturation measured at the end of isometric quadriceps contraction by multichannel near-infrared spectroscopy.” J. Biomed. Opt. **9**(2), 413–420 (2004).

59. U. Wolf, M. Wolf, J. H. Choi, L. A. Paunescu, L. P. Safonova, A. Michalos, and E. Gratton. “Mapping of hemodynamics on the human calf with near infrared spectroscopy and the influence of the adipose tissue thickness.” Adv. Exp. Med. Biol. **510**, 225–230 (2003).

60. B. C.Wilson, M. S. Patterson, and L. Lilge. “Implicit and explicit dosimetry in photodynamic therapy: a new paradigm.” Lasers Med. Sci. **12**(3), 182–199 (1997).

61. H.Wang, M. E. Putt, M. J. Emanuele, D. B. Shin, E. Glatstein, A. G. Yodh, and T. M. Busch. “Treatment-induced changes in tumor oxygenation predict photodynamic therapy outcome.” Cancer Res. **64**, 7553–7561 (2004).

62. U. Sunar, J. Zhang, J. Du, T. Durduran, C. Zhou, G. Yu, A. Kilger, H. Quon, R. Lustig, L. Loevner, S. Nioka, A. G. Yodh, and B. Chance. “Clinical responses of head & neck tumors to radiation therapy by NIR spectroscopy.” Biomedical Topical Meetings (The Optical Society of America, Washington, DC) FB7 (2004).

63. M. C. Case and P. F. Zweifel. Linear Transport Theory. Addison-Wesley New York (1967).

64. K. Furutsu, and Y. Yamada, "Diffusion approximation for a dissipative random medium and the applications," Physical Review E 50, 3634 (1994).

65. R. Pierrat, J.-J. Greffet, and R. Carminati, "Photon diffusion coefficient in scattering and absorbing media," J. Opt. Soc. Am. A 23, 1106-1110 (2006).

66. T. Durduran, A. G. Yodh, B. Chance, and D. A. Boas. “Does the photon-diffusion coefficient depend on absorption?” J. Opt. Soc. Am. A **14**(12), 3358 (1997).

67. Boas, D.A., O’Leary, M.A., Chance, B., and Yodh, A.G., “Detection and characterization of optical inhomogeneities with diffuse photon density waves: a signal-to-noise analysis,” Appl. Opt., **36**, 75 (1997)

68. Boas, D.A., O’Leary, M.A., Chance, B., and Yodh, A.G., “Scattering and wavelength transduction of diffuse density waves,” Phys. Rev. E., **47**, R2999, (1993)

69. Li, X.D., Durduran, T., Yodh, A.G., Chance, B., and Pattanayak, D.N., “Diffraction tomography for biochemical imaging with diffuse-photon density waves,” Opt. Lett., **22**, 573, (1997)

70. Ripoll, J., Nieto-Vesperinas, M., and Carminati, R., “Spatial resolution of diffuse photon density waves,” J. Opt. Soc. Am., **A16**, 1466 (1999)

71. Reynolds, J.S., Przadka, A., Yeung, S.P., and Webb, K.J., “Optical diffusion imaging: a comparative numerical and experimental study,” Appl. Opt., **35**, 3671 (1996)

72. O’Leary, M.A., Boas, D.A., Chance, B., and Yodh, A.G., “Experimental images of heterogeneous turbid media by frequency-domain diffusing-photon tomography,” Opt. Lett., **20**, 426 (1995)

73. Colak, S.B., Papaioannou, D.G., ’t Hooft, G.W., van der Mark, M.B., Schomberg, H., Paasschens, J.C.J., Melissen, J.B.M. and van Asten, N.A.A.J., “Tomographic image reconstruction from optical projections in light-diffusing media,” Appl. Opt., **36**, 180 (1997)

74. Matson, C.L., “A diffraction tomographic model of the forward problem using diffuse photon density waves,” Opt. Express, **1**, 6 (1997)

75. Yao, Y., Wang, Y., Pei, Y., Wenwu, Z., and Barbour, R.L., “Frequency-domain optical imaging of absorption and scattering distributions by a Born iterative method,” J. Opt. Soc. Am., **A14**, 325 (1997)

76. Chen, B., Stamnes, J.J., and Stamnes, K., “Reconstruction algorithm for

diffraction tomography of diffuse photon density waves in a random medium," Pure Appl. Opt., **7**, 1161 (1998)

77. Matson, C.L. and Liu, H., "Backpropagation in turbid media," J. Opt. Soc. Am., **A16**, 1254 (1999)

78. Gaudette, R.J., Brooks, D.H., DiMarzio, C.A., Kilmer, M.E., Miller, E.L., Gaudette, T., and Boas, D.A., "A comparison study of linear reconstruction techniques for diffuse optical tomographic imaging of absorption coefficient," Phys. Med. Biol., **45**, 1051 (2000)

79. Kilmer, M.E., Miller, E.L., Boas, D., and Brooks, D., "A shape-based reconstruction technique for DPDW data," Opt. Express, **7**, 481 (2000)

80. Markel, V.A. and Schotland, J.C., "Inverse problem in optical diffusion tomography. I. Fourier- Laplace inversion formulas," J. Opt. Soc. Am., **A18**, 1336 (2001)

81. Schotland, J.C., "Continuous-wave diffusion imaging," J. Opt. Soc. Am., **A14**, 275 (1997)

82. Cheng, X. and Boas, D.A., "Diffuse optical reflection tomography with continuous-wave illumination," Opt. Express, **3**, 118 (1998)

83. G. Strangman, D. A. Boas, and J. Sutton, "Non-invasive neuroimaging using near infrared light," Biol. Psychiatry **52**, 679–693 (2002).

84. R. Cubeddu, A. Pifferi, L. Spinelli, P. Taroni, and A. Torricelli, "Breast lesion characterization by a novel nonlinear perturbation approach," Proc. SPIE **5138**, 23–29 (2003).

85. B. W. Pogue, M. Testorf, T. McBridge, U. Osterberg, and K.Paulsen, "Instrumentation and design of a frequency domain diffuse optical tomographic imager for breast cancer detection," Opt. Express **1**, 391–403 (1997)

86. D. Grosenick, H. Wabnitz, H. Rinneberg, K. T. Moesta, and P. M. Schlag, "Development of a time-resolved optical mammography and first in vivo applications," Appl. Opt. **38**, 2927–2943 (1999)

87. J. C. Hebden, A. Gibson, R. M. Yusof, N. Everdell, E. M. C. Hillman, D. T. Delpy, S. R. Arridge, T. Austin, J. H. Meek, and J. S. Wyatt, "Three-dimensional optical tomography of the premature infant brain," Phys. Med. Biol. **47**, 4155–4166 (2002)

88. J. C. Hebden, A. Gibson, T. Austin, R. M. Yusof, N. Everdell, D. T. Delpy, S. R. Arridge, J. H. Meek, and J. S. Wyatt, "Imaging changes in blood volume

and oxygenation in the newborn infant brain using three-dimensional optical tomography," Phys. Med. Biol. **49**, 1117–1130 (2004).

89. "Theoretical Models and Algorithms in Optical Diffusion Tomography" in Biomedical Photonics Handbook, Stephen J. Norton and Tuan Vo-Dinh (CRC Press, 2003)

90. Cell Biology, a Laboratory Handbook (Vol. 3, 136–146) Bastiaens, P. I. H. and Jovin, T. M. (Academic Press, 1998)

91. Griffin, A. B., Adams, S. R. and Tsien, R. Y. "Specific Covalent Labeling of Recombinant Protein Molecules Inside Live Cells," Science, **281**, 269–272 (1998)

92. Tsien, R. Y. "The green fluorescent protein," Ann. Rev. Biochem. **76**, 509–538 (1998)

93. "Lifetime-Based Imaging" in Biomedical Photonics Handbook, Petr Herman, Hai-Jui Lin and Joseph R. Lakowicz (CRC Press, 2003)

94. M. A. A. Neil, R. Juškaitis and T. Wilson, "Real time 3D fluorescence microscopy by two beam interference illumination," Opt. Commun. **153**, 1-4 (1998)

95. Hamamatsu, "Guide to Streak Cameras," http://sales.hamamatsu.com/assets/pdf/catsandguides/e_streakh.pdf

96. W. Becker, Advanced time-correlated single-photon counting techniques (Springer, 2005)

97. Becker & Hickl GmbH, "The bh TCSPC handbook," http://www.becker-hickl.com/literature.htm

98. W. Becker, Advanced time-correlated single-photon counting techniques (Springer, 2005)

99. F. E. W. Schmidt, M. E. Fry, E. M. C. Hillman, J. C. Hebden, and D. T. Delpy, "A 32-channel time-resolved instrument for medical optical tomography," Rev. Sci. Instrum. **71**, 256-265 (2000).

100. Valery Tuchin, Tissue optics : light scattering methods and instruments for medical diagnosis (SPIE Publications, 2000)

101. N. G. Chen, and J. Bai, "Estimation of quasi-straightforward propagating light in tissues," Phys. Med. Biol. **44**, 1669-1676 (1999)

102. N. G. Chen, and Q. Zhu, "Optical Tomography with Early Arriving

Photons: Sensitivity and Resolution Analysis," Proc. SPIE, **4250**, 38-44 (2001)

103. N.G. Chen and Q. Zhu, "Time-resolved diffusive optical tomography using pseudo-random sequences," Opt. Express. **11**, 3445-3454 (2003).

104. N.G. Chen and Q. Zhu, "Time-resolved optical measurements with spread spectrum excitations," Opt. Lett. **27**, 1806-1808 (2002).

105. N.G. Chen and Q. Zhu, "Spread spectrum time-resolved photon migration imaging system: the principle and simulation results," Proc. SPIE **4955**, 474-479 (2003).

106. W. Mo and N.G. Chen, "A Novel Implementation of Time-Domain Diffusive Optical Tomography," IEEE/ICME, 1101-1104 (2007)

107. W. Mo and N.G. Chen, "High performance time-resolved diffuse optical tomography system," Proc. SPIE, **6849**, 04-08 (2008)

108. R. C. Dixon, Spread Spectrum Systems (Wiley, New York, 1976)

109. H. J. Zepernick and A. Finger, Pseudo Random Signal Processing: Theory and Application (Wiley, 2003)

110. M. Firbank and D. T. Delpy, "A design for a stable and reproducible phantom for use in near infra-red imaging and spectroscopy," Phys. Med. Bio. 38, 847-853 (1993)

111. M. Firbank, M. Oda and D. T. Delpy, "An improved design for a stable and reproducible phantom material for use in near-infrared spectroscopy and imaging," Phys. Med. Biol. **40,** 955-961 (1995)

112. W. Cheong, S. A. Prahl, and A. J. Welch, "A Review of the Optical Properties of Biological. Tissues," IEEE J. Quantum Electron. **26**, 12, 2166-2185 (2002)

113. A. Ishimaru, "Diffusion of light in turbid material," Appl. Opt. **28**, 2210-2215 (1989)

114. S.L. Jacques, "Time resolved propagation of ultrashort laser pulses within turbid tissues," Appl. Opt. **28**, 2223-2229 (1989)

115. A. E. Profio, "Light transport in tissue," Appl. Opt. **28**, 2216-2222 (1989)

116. D. R. Leff, O. Warren, L. C. Enfield, A. P. Gibson, T. Athanasiou, D. K. Pattern, J. C. Hebden, G. Z. Yang, and A. Darzi, "Diffuse optical imaging of the healthy and diseased breast - a systematic review," Breast Cancer Res. Treat. **108**, 9-22 (2008).

117. L. C. Enfield, A. P. Gibson, N. L. Everdell, D. T. Delpy, M. Schweiger, S. R. Arridge, C. Richardson, M. Keshtgar, M. Douek, and J. C. Hebden, “Three-dimensional time-resolved optical mammography of the uncompressed breast,” Appl. Opt. **46**, 3628-3638 (2007).

118. A. Cerussi, N. Shah, D. Hsiang, A. Durkin, J. Butler, and B. J. Tromberg, “In vivo absorption, scattering, and physiologic properties of 58 malignant breast tumors determined by broadband diffuse optical spectroscopy,” J. Biomed. Opt. **11**, 044005 (2006).

119. J. C. Hebden and T. Austin, “Optical tomography of the neonatal brain,” Euro. Rad. **17**, 2926-2933 (2007).

120. M. A. Franceschini, D. K. Joseph, T. J. Huppert, S. G. Diamond, and D. A. Boas, “Diffuse optical imaging of the whole head,” J. Biomed. Opt. **11**, 054007 (2006).

121. T. Austin, J. C. Hebden, A.P. Gibson, G. Branco, R. Yusof, S. R. Arridge, J. H. Meek, D.T Delpy, and J. S.Wyatt, “Three-dimensional optical imaging of blood volume and oxygenation in the preterm brain,” Neuroimage, **31**, 1426-1433 (2006).

122. H. Xu, H. Dehghani, B. W. Pogue, R. Springett, K. D. Paulsen, J. F. Dunn, “Near-infrared imaging in the small animal brain: optimization of fiber positions,” J. Biomed. Opt. **8**, 102-110 (2003).

123. M. Schweiger, A. Gibson, and S. R. Arridge, “Computational aspects of diffuse optical tomography,” Comput. Opt. **5**, 33-41 (2001).

124. F. Gao, H. J. Zhao, Y. Yamada, “Improvement of image quality in diffuse optical tomography by use of full time-resolved data,” Appl. Opt. **41**, 778-791 (2002).

125. W. Becker, A. Bergmann, A. Gibson, N. Everdell, D. Jennions, M. Schweiger, A. R. Arridge, and J. C. Hebden, “Multi-dimensional time-correlated single photon counting applied to diffuse optical tomography,” Proc. SPIE **5693**, 34-42 (2005).

126. H. Eda, I. Oda, Y. Ito, Y. Wada, Y. Oikawa, Y. Tsunazawa, and M. Takada, “Multi-channel time-resolved optical tomographic imaging system,” Rev. Sci. Instrum. **70**, 3595-3602 (1999).

127. A V Bykov, A K Indukaev, A V Priezzhev, R Myllylä, “Study of the influence of glucose on diffuse reflection of ultrashort laser pulses from a medium simulating a biological tissue,” Quantum Electronics, **38**, 491–496 (2008).

128. S.R. Arridge, “Optical tomography in medical imaging,” Inverse Probl. **15**, R41-93, (1999).

129. World Health Organization,
http://www.who.int/mediacentre/factsheets/fs312/en/

130. O.S. Khalil, “Spectroscopic and clinical aspects of noninvasive glucose measurements,” Clin. Chem. **45**, 165 (1999)

131. O.S. Khalil, “Non-invasive glucose measurement technologies: An update from 1999 to the dawn of the new millennium,” Diabetes Technol. Ther. **6**, 660–697 (2004)

132. CE Ferrante do Amaral, B Wolf, “Current development in non-invasive glucose monitoring,” Medical Engineering & Physics, **30**(5), 541-549 (2008)

133. GB Christison, HA MacKenzie, ‘Laser photoacoustic determination of physiological glucose concentrations in human whole blood’, Medical and Biological Engineering and Computing, **31**, 3, 284-290 (1993)

134. Hugh A. MacKenzie, Helen S. Ashton, Stephen Spiers, Yaochun Shen, Scott S. Freeborn, John Hannigan, John Lindberg and Peter Rae, ‘Advances in Photoacoustic Noninvasive Glucose Testing’, Clinical Chemistry, **45**, 1587-1595 (1999)

135. Wickramasinghe Y, Yang Y, Spencer SA. Current problems and potential techniques in in-vivo glucose monitoring. J Fluorescence **14**, 513 (2004)

136. Allen TJ, Cox BT, Beard PC. Generating photoacoustic signals using high peak power laser diodes, Proceedings of the SPIE, **5697**, 233–242. (2005)

137. Ram Weiss, Yevgeny Yegorchikov, Alexander Shusterman, Itamar Raz, ‘Noninvasive Continuous Glucose Monitoring Using Photoacoustic Technology—Results from the First 62 Subjects’, Diabetes Technology & Therapeutics, **9**(1), 68-74 (2007)

138. M Kinnunen, R Myllylä, T Jokela, S Vainio, ‘In vitro studies toward noninvasive glucose monitoring with optical coherence tomography’, Applied Optics, **45**(10):2251-60 (2006)

139. Gourzi M, Rouane A, Guelaz R, Alavi MS, McHugh MB, Nadi M, et al. “Non-invasive glycaemia blood measurements by electromagnetic sensor: study in static and dynamic blood circulation,” J Med Eng Technol **29,** 22 (2005)

140. Oz G, Henry PG, Seaquist ER, Gruetter R. Direct, “Noninvasive

measurement of brain glycogen metabolism in humans," Neurochem Int **4**, 323 (2003)

141. Pfutzner A, Caduff A, Larbig M, Schrepfer T, Forst T, "Impact of posture and fixation technique on impedance spectroscopy used for continuous and noninvasive glucose monitoring. Diabetes Technol Ther, **6,** 435, (2004)

142. Caduff A, Hirt E, Feldman Y, Ali Z, Heinemann L, "First human experiments with a novel non-invasive, non-optical continuous glucose monitoring system. Biosens Bioelectron," **19**, 209, 2003

143. Malchoff CD, Shoukri K, Landau JI, Buchert JM, "A novel noninvasive blood glucose monitor. Diabetes Care," **25**, 2268 (2002)

144. A. J. Berger, T. W. Koo, I. Itzkan, G. Horowitz, and M. S. Feld, "Multicomponent blood analysis by near-infrared Raman spectroscopy,'' Appl. Opt. **38**, 2916–2926 (1999)

145. Berger AJ, Itzkan I, Feld MS, "Feasibility of measuring blood glucose concentration by near-infrared Raman spectroscopy," Spectrochim Acta A, **53,** 287 (1997)

146. A. M. Enejder, T. G. Scecina, J. Oh, M. Hunter, W. Shih, S. Sasic, G.L. Horowitz, and M. S. Feld, "Raman spectroscopy for non-invasive glucose measurements," J. Biomed. Opt. **10**, 1–9, (2005)

147. Tierney MJ, JayalakshmiY, ParrisNA, ReidyMP, Uhegbu C,Vijayakumar P. "Design of a biosensor for continual, transdermal glucose monitoring," Clin Chem, **45**, 1681 (1999)

148. Panchagula R, Pillai O, Nair VB, Ramarao P. "Transdermal iontophoresis revisited," Curr Opin Chem Biol **4,** 468 (2000)

149. Park HD, Lee KJ, Yoon HR, Namb HH. "Design of a portable urine glucose monitoring system for health care," Computers Biol Med **35,** 275 (2005)

150. Roman M. Balabin, Ravilya Z. Safieva, and Ekaterina I. Lomakina, "Comparison of linear and nonlinear calibration models based on near infrared (NIR) spectroscopy data for gasoline properties prediction," Chemometr Intell Lab **88** (2), 183–188 (2007)

151. M. R. Robinson, R. P. Eaton, D. M. Haaland, G. W. Koepp, E. V. Thomas, B. R. Stallard, and P. L. Robinson, ''Noninvasive glucose monitoring in diabetic patients: a preliminary evaluation,'' Clin.Chem. **38**, 1618–1622 (1992)

152. H. M. Heise, R. Marbach, T. Koschinsky, and F. A. Gries, ''Non-invasive

blood glucose sensors based on near-infrared spectroscopy,’’ Artif. Organs **18**, 439–447 (1994)

153. U. A. Muller, B. Mertes, C. Fischbacher, K. U. Jageman, and K. Danzer, ‘‘Non-invasive blood glucose monitoring by means of near infrared spectroscopy: methods for improving the reliability of calibration models,’’ Int. J. Artif. Organs **20**, 285–290 (1997)

154. H. M. Heise, A. Bittner, and R. Marbach, “Clinical chemistry and near infrared spectroscopy: Technology for non-invasive glucose monitoring,” J. Near Infrared Spectrosc. **6**, 349–359 (1998)

155. M. A. Arnold, J. J. Burmeister, and G. W. Small, “Phantom Glucose Calibration Models from Simulated Noninvasive Human Near-Infrared Spectra,” Anal. Chem. **70**, 1773 (1998)

156. GL Coté, “Noninvasive and minimally-invasive optical monitoring technologies,” J.Nutr. **131**(5), 1596S–1604S (2001)

157. H. M. Heise, “Applications of near-infrared spectroscopy in medical sciences,” in Near-Infrared Spectroscopy, H. W. Siesler, Y. Ozaki, S. Kawata, and H. M. Heise, Eds., pp. 289 Wiley-VCH, Weinheim, Germany (2002)

158. K. Maruo, M. Tsurugi, M. Tamura, and Y. Ozaki, “In vivo noninvasive measurement of blood glucose by near-infrared diffusereflectance spectroscopy,” Appl. Spectrosc. **57**(10), 1236–1244 (2003)

159. Burmeister JJ, Arnold MA, Small G W. “Noninvasive blood glucose measurements by near infrared transmission spectroscopy across human tongues,” Diabetes Technol Ther **2,** 5-16 (2000)

160. Malin SF, Ruchti TL, Blank TB, et al. “The noninvasive measurement of glucose by near- infrareddiffuse reflectance spectroscopy,” Clin Chem **45,** 1651 (1999)

161 . I. Fine, B.Fikhte and L.D. Shvartsman. “Time dependent light transmission through blood (in vivo) and RBC suspensions (in vitro) accompanied by RBC Aggregation,” Bul. of American Physical Society, **45**, 1, 957-958 (2000)

162. L.D. Shvartsman, I. Fine. “RBC Aggregation Effects on Light Scattering from Blood,” SPIE Proc., **4162**, 120-129 (2000)

163. I. Fine, B.Fikhte and L.D. Shvartsman. “RBC aggregation assisted light transmission through blood and occlusion oximetry,” SPIE Proc. **4162**, 130-139 (2000)

164. L.D. Shvartsman, I. Fine. “Light Scattering Changes Caused by RBC Aggregation: Physical Basis for New Approach to Non-Invasive Blood Count,” SPIE Proceedings, **4263**, 131-142 (2001)

165. I. Fine, B. Fikhte, L.D. Shvartsman. “Occlusion spectroscopy as a new paradigm for noninvasive blood measurements,” SPIE. Proc. **4263**, 122-130 (2001)

166. Fine I, Shvartsman L. “Non-Invasive method and system of optical measurements for determining the concentration of a substance in blood,” US patent 6,400,972, Jun 4, 2002.

167. I. Fine, L.D. Shvartsman. "Method for non-invasive optical measurement of blood parameters,” US Patent 6,587,704, Jul 1, 2003

168. Shvartsman L, Fine I. “Optical Transmission of blood: effect of erythrocyte aggregation,” IEEE Trans Biomed Eng. **50**(8), 1026-1033 (2003)

169. V.Tuchin. “Light scattering study of tissues,” Physics —Uspekhi **40**, 5, 495 (1997)

170. A.V. Priezzhev, O.M. Ryaboshapka, N.N. Firsov, IV. Sirko. “Aggregation and disaggregation of erythrocytes in whole blood: Study by backscattering technique,” Journal of Biomed. Optics, **4**, 76-84 (1999)

171. Orna Amir et al. “Continuous Noninvasive Glucose Monitoring Technology Based on ‘Occlusion Spectroscopy’,” J Diabetes Sci Technol. **1**(4), 463–469 (2007)

172. I. Fine, “Non-invasive method and system of optical measurements for determining the concentration of a substance in blood,” US Patent 6400972,2002

173. Hanli Liu et al, “Dependence of tissue optical properties on solute-induced changes in refractive index and osmolarity,” Journal of Biomedical Optics, **1**(2), 200–211 (1996)

174. John S. Maier, Scott A. Walker, Sergio Fantini, Maria Angela Franceschini, and Enrico Gratton, “Possible correlation between blood glucose concentration and the reduced scattering coefficient of tissues in the near infrared,” Opt. Lett. **19**, 2062-2064 (1994)

175. O. Lutz, Z. Meraihi, J. Mura, A. Frey, G. Riess, and A. Bach, “Fat emulsion particle size: influence on the clearance rate and the tissue lipolytic activity,” Am J Clin Nutr **50**, 1370-1381 (1989)

176. D. Contini, H. Liszka, A. Sassaroli, and G. Zaccanti, “Imaging of highly

turbid media by the absorption method," Applied Optics, **35**, 2315-2324 (1996)

177. Prerana, M. R. Shenoy, and B. P. Pal, "Method to determine the optical properties of turbid media," Applied Optics, **47**, 3216-3220 (2008)

178. "Mie Scattering Calculator," http://omlc.ogi.edu/calc/mie_calc.html

179. A. Akkar, and R. H. Moler, "Formulation of intravenous Carbamazepine emulsions by SolEmuls®technology," European Journal of Pharmaceutics and Biopharmaceutics, **55**, 305-312 (2003)

Appendix

A.1 MATLAB code

A.1.1 PRSPC simulation

```
%%%%%%%%%%%%%%%%%%%%   Original_TPSF
r=6;
t=[100e-12:100e-12:12.8e-9];
mua=0.05;
musp=8;
D = 1/3/(mua + musp);
c=3e10/1.33;
Origin_TPSF = c*power(4*pi*D*c.*t,-1.5).*exp(-r^2/4/D/c./t-mua*c.*t);
%%%%%%%%%%%%%%%%%%%%     PRSPC
%%%%%%%%%%%%%%%%%%%%
load prbs1.mat;
prbs_dc=prbs;
for i=1:2046;
  if prbs_dc(i)<0;
    prbs_dc(i)=0;%prbs_dc contains dc value.
  end
end
prbs_repeat=[prbs_dc;prbs_dc;prbs_dc];
temp1=conv(prbs_repeat,Origin_TPSF);
response=temp1(2047:4092);
PhotonRate2=10/sum(response)/4.8876;
response_normalised=PhotonRate2*response;
PRSPC_Theoretical_TPSF=4.8876*1e6*xcorr([response_normalised;response_normalised],prbs);
LongPulse=zeros(204600,1);
PtPstLastRound=204600;
```

```
for n=1:4.8876*1e4;
    s=zeros(204600,1);
    mmm=find(rand(204600,1)<(repmat(response_normalised,100,1)));
    PhotonPositions=[PtPstLastRound-205100;mmm];
    i=1;
    while i<=length(PhotonPositions)
        xxx=find(abs(PhotonPositions-PhotonPositions(i))<500);
        if(isempty(xxx))
        else
        xxx(1)=[];
        PhotonPositions(xxx)=[];
        end
        i=i+1;
    end
    PhotonPositions(1)=[];
    PtPstLastRound=PhotonPositions(length(PhotonPositions));
    s(PhotonPositions)=1;
    LongPulse=LongPulse+s;
end
temp2=reshape(LongPulse,2046,100);
pulse=sum(temp2,2);
tpsf_prspc=xcorr([pulse;pulse],prbs);
factor1=sum(pulse)/sum(response)*2043;
tpsf_prspc=tpsf_prspc/factor1;
tpsfP=tpsf_prspc(4092:4219)-tpsf_prspc(4400:4527);
save Prspc.mat;
```

A.2 Labview code

A.2.1 Pressure display

Description:

This VI (virtual instrument) is used for real time display of the pressure applied to the finger tip during in-vivo blood glucose testing experiments.

Front panel:

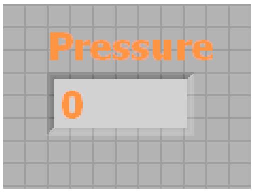

Block diagram:

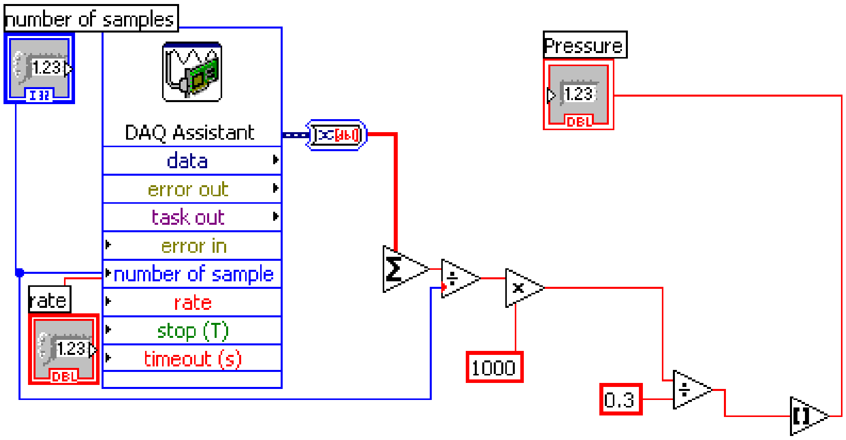

A.2.2 Single TPSF acquisition

Description:

This VI is used for acquisition of one TPSF. It can be integrated into a complex program as a sub-VI for multiple TPSF acquisition.

Front panel:

See Figure 4.15.

Block diagram:

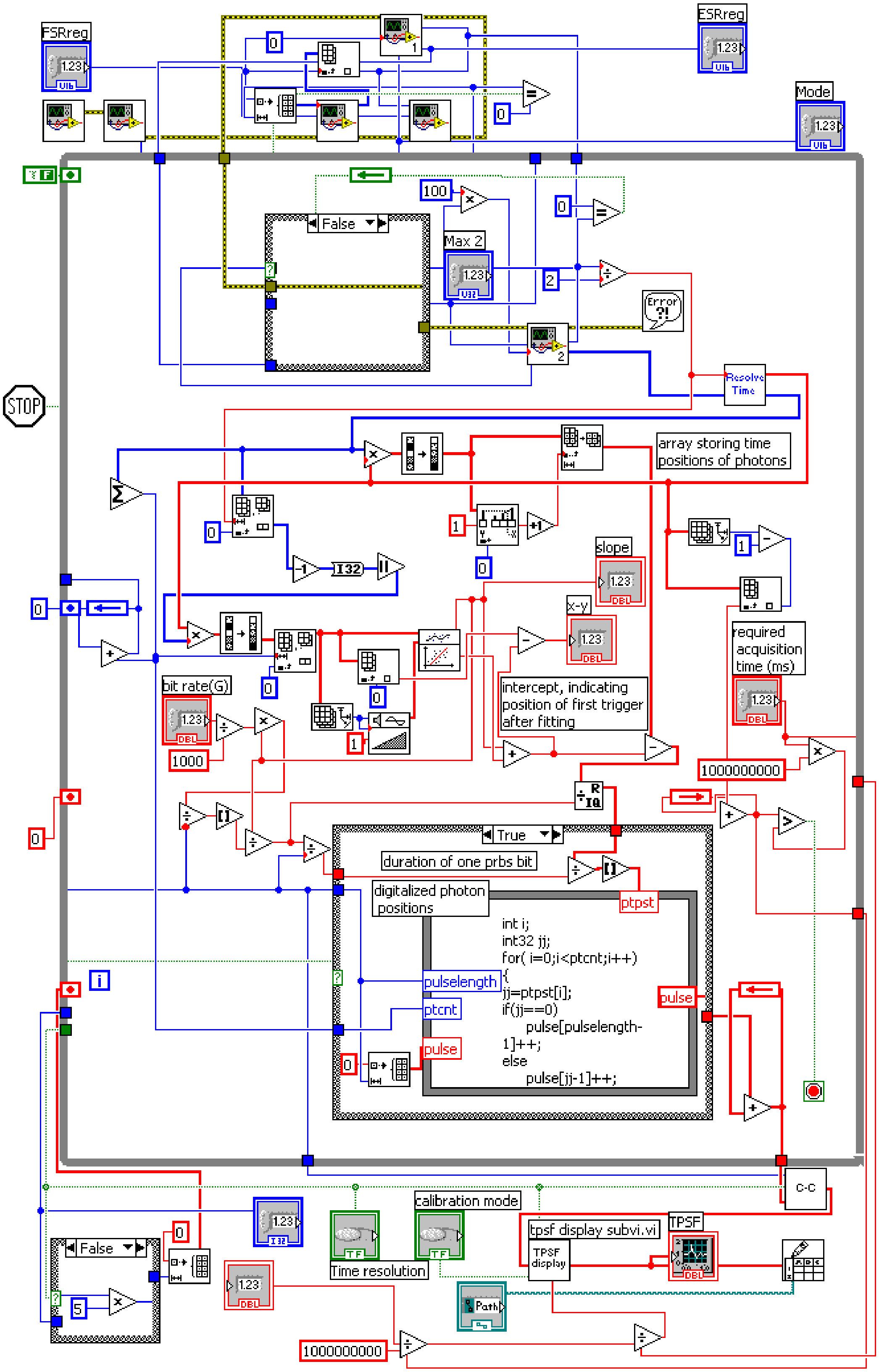

```
int i;
int32 jj;
for( i=0;i<ptcnt;i++)
{
jj=ptpst[i];
if(jj==0)
    pulse[pulselength-
1]++;
else
    pulse[jj-1]++;
```

List of key sub-VIs:

Tpsf display subvi.vi (A.2.2.1)

Cross correlation operation subvi.vi (A.2.2.2)

HRM_ResolvingTime.vi (A.2.2.3)

HRM_GetFifoData.vi

HRM_RunFifoTimeTagging.vi

A.2.2.1 TPSF display

Description:

This VI is used to retrieve and display the true TPSF from the cross-correlation result.

Front panel:

N/A.

Block diagram:

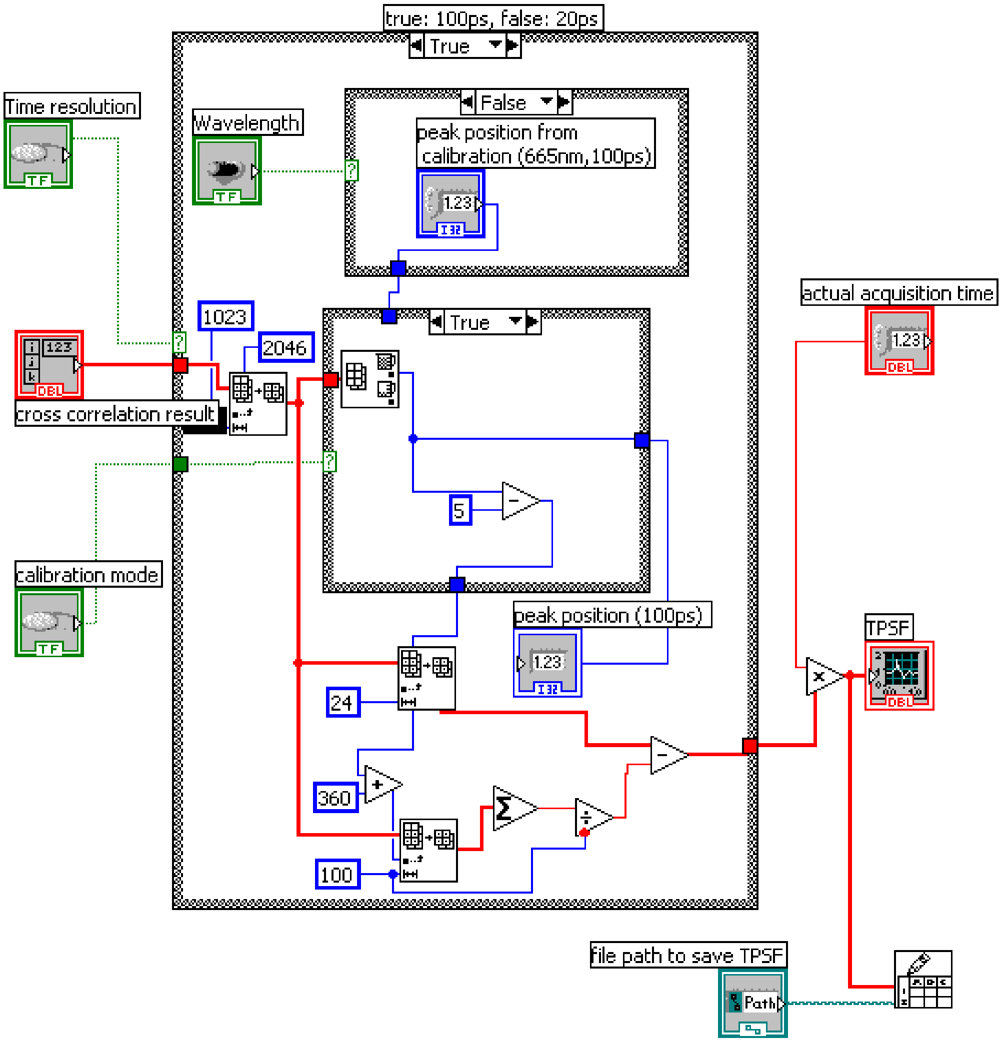

A.2.2.2 Cross-correlation operation

Description:

This VI is to load the PRBS from computer hard disk (the PRBS loaded is the same with that used for light source modulation) and use it to cross-correlate with the accumulated photon histogram by calling MATLAB code.

Front panel:

N/A.

Block diagram:

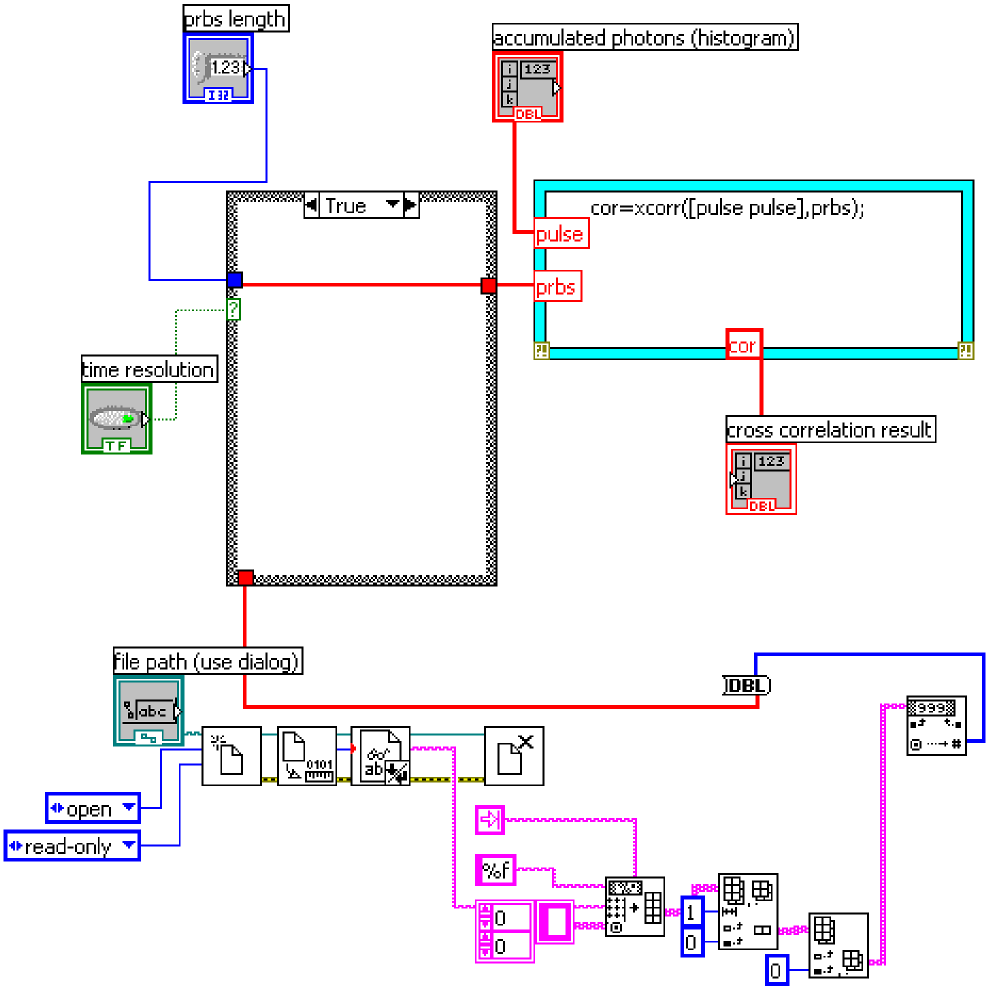

```
cor=xcorr([pulse pulse],prbs);
```

A.2.2.3 HRM_ResolvingTime

Description:

This VI is to read the output from the HRMTime timing module and resolve the readings into true time tags.

Front panel:

N/A.

Block diagram:

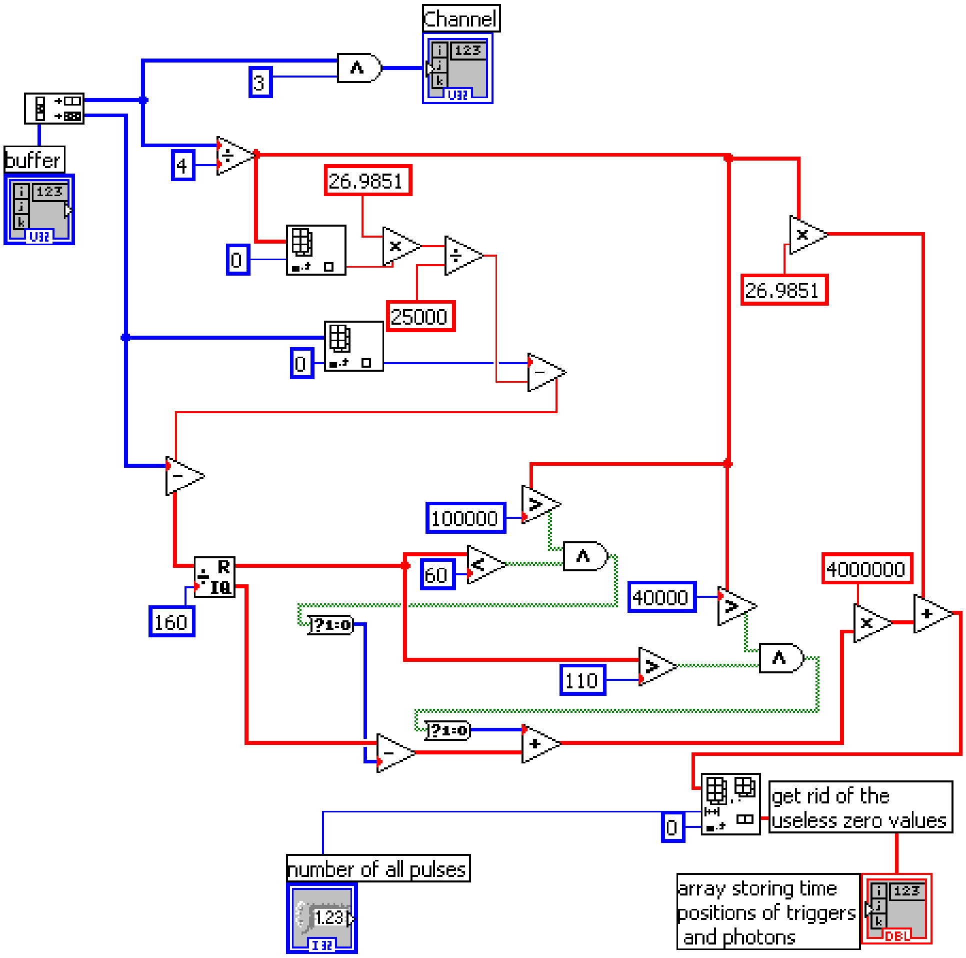
Channel
buffer
3
4
26.9851
0
25000
0
26.9851
100000
60
40000
4000000
160
110
?1:0
?1:0
0
get rid of the useless zero values
number of all pulses
array storing time positions of triggers and photons
U32
U32
I32
DBL
1.23

A.2.3 Data acquisition for in-vivo blood glucose testing experiments

Description:

This VI is used for data acquisition for the in-vivo blood glucose testing experiments. The program can acquire multiple TPSFs, switch light source between different wavelengths and save the data, all automatically according to user settings.

Front panel:

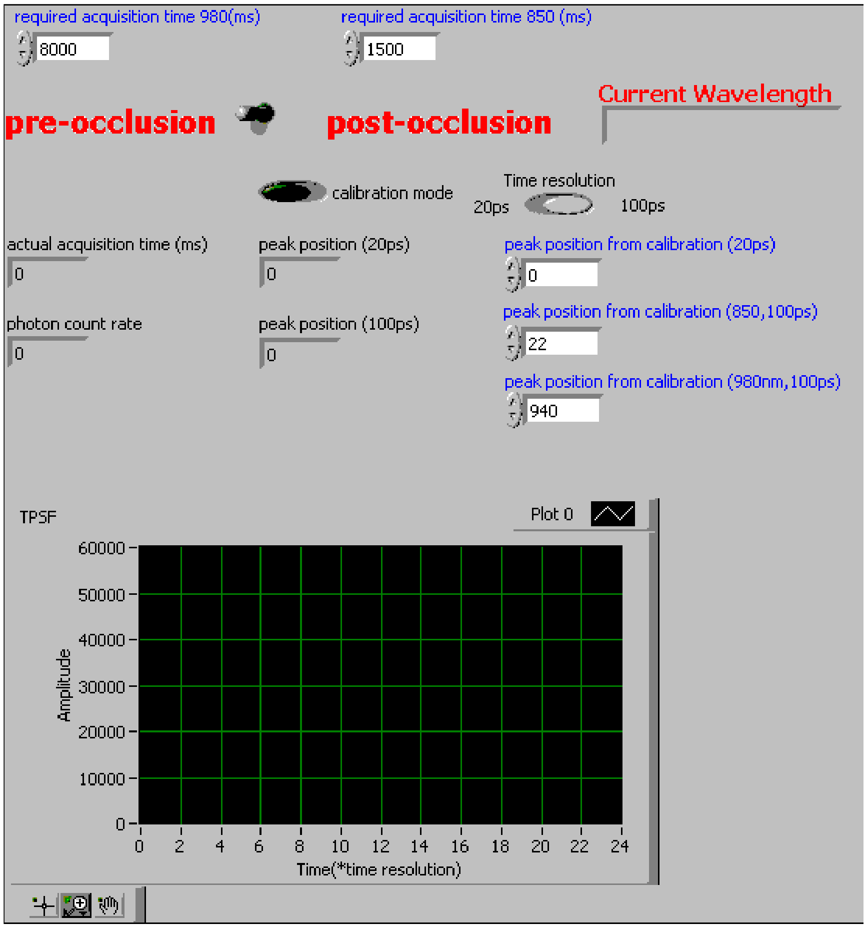

required acquisition time 980(ms): 8000

required acquisition time 850 (ms): 1500

pre-occlusion / post-occlusion

Current Wavelength

calibration mode

Time resolution: 20ps / 100ps

actual acquisition time (ms): 0

peak position (20ps): 0

peak position from calibration (20ps): 0

photon count rate: 0

peak position (100ps): 0

peak position from calibration (850,100ps): 22

peak position from calibration (980nm,100ps): 940

Block diagram:

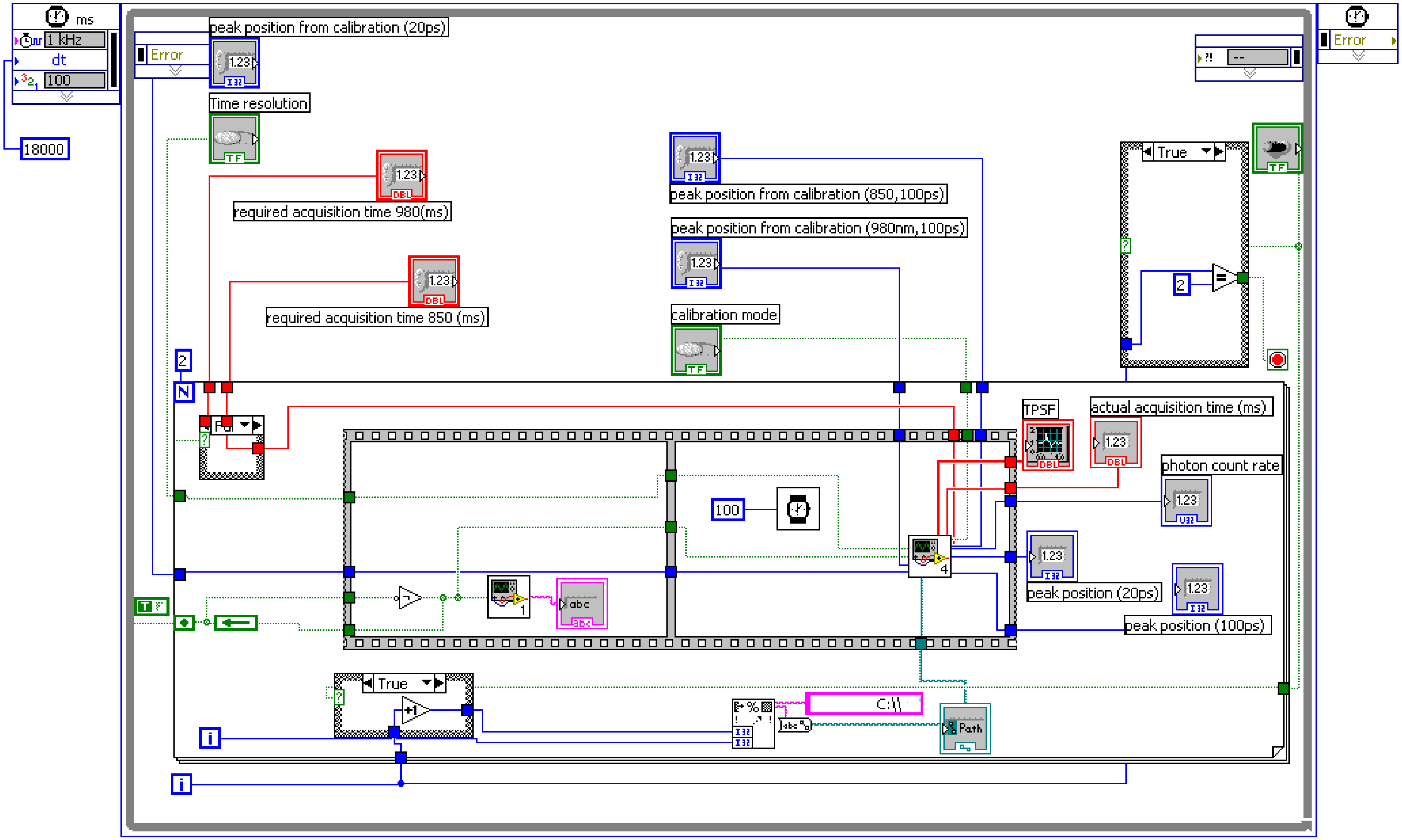
ms
1 kHz
dt
100
18000
Error
peak position from calibration (20ps)
1.23
I32
Time resolution
TF
1.23
DBL
required acquisition time 980(ms)
1.23
DBL
required acquisition time 850 (ms)
1.23
I32
peak position from calibration (850,100ps)
peak position from calibration (980nm,100ps)
1.23
I32
calibration mode
TF
True
2
=
TF
--
Error
2
N
TPSF
DBL
actual acquisition time (ms)
1.23
DBL
photon count rate
1.23
U32
100
4
1.23
I32
peak position (20ps)
1.23
I32
peak position (100ps)
TF
1
abc
True
+1
C:\\
Path
i
i

List of key sub-VIs:

Single TPSF acquisition.vi (A.2.2)

optical switch (once).vi (A.2.3.1)

A.2.3.1 Optical switch (once)

Description:

This VI is to switch the light source employed for sample illumination between two different wavelengths.

Front panel:

N/A.

Block diagram

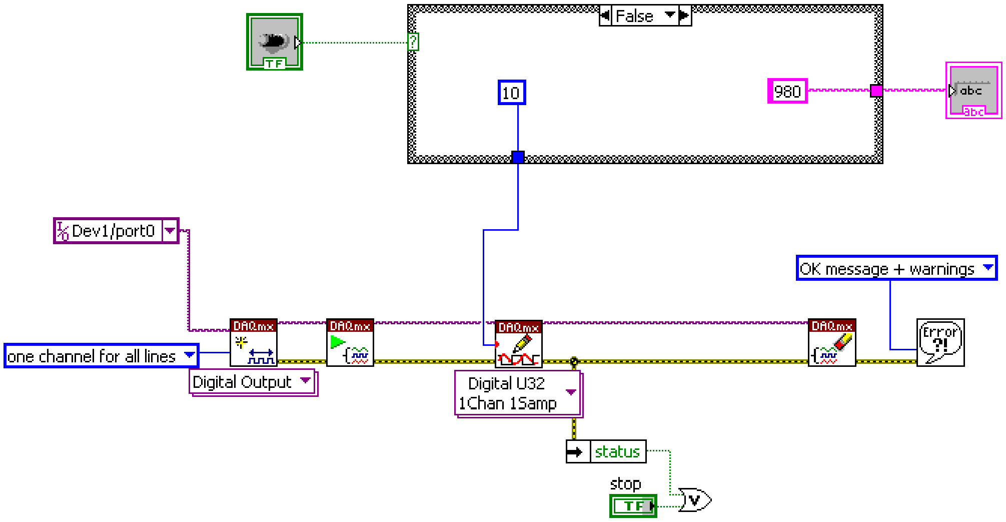

A.3 Phantom fabrication

A.3.1 Calculation of the μ_s' of liquid phantom (Lipofundin solution)

The Lipofundin emulsion used in this study is Lipofundin MCT/LCT 20% from B.Braun Melsungen AG, Germany. Every 1000 ml Lipofundin emulsion contains

- Soya oil 100.0 g
- Phospholipids: Egg Lecithin 12.0 g
- Isotonic substance: Glycerol 25.0 g
- Medium-chain Triglycerides: 100.0 g

The physical parameters are [175-177]:

- Particles size in 20% emulsion: ~ 265 um;
- Number of particles for 20% MCT: ~ 140 × 1015 /Liter.

To use Mie calculator [178], a real refractive index of 1.46 and an imaginary refractive index of 0 were selected for Lipofundin emulsion [179].

According to the calculation results shown in Table A.1, the isotropic scattering factor *g* is about 0.30, which gives a reduced scattering coefficient of:

$$
\begin{aligned}
\mu_s' &= (1-g) \times \mu_s \\
&= (1-0.30) \times 4.13\ \text{cm}^{-1} \\
&\sim 2.9\ \text{cm}^{-1}
\end{aligned}
$$

The overall absorption coefficient of the Lipofundin solution is solely contributed by distilled water, which is around 0.02 cm^{-1} for wavelength 850 nm under room temperature. These values were used in Chapter 5.

Table A.1 Calculation results using Mie scattering calculation

Parameters	**Value**	**Unit**
Sphere Diameter	0.265	micron
Refractive Index of Medium (20°C)	1.3316	1
Real Refractive Index of Sphere	1.46	1
Imaginary Refractive Index of Sphere	0.000016	1
Wavelength in Vacuum	0.850	micron
Concentration	0.42*	spheres/micron^3
Wavelength in Medium	0.63833	micron
Size Parameter	1.3042	1
Average Cosine of Phase Function	0.2957	1
Scattering Efficiency	0.010505	1
Extinction Efficiency	0.017834	1
Backscattering Efficiency	0.01038	1
Scattering Cross Section	0.00098363	micron^2
Extinction Cross Section	0.00098381	micron^2
Backscattering Cross Section	0.0005794	micron^2
Scattering Coefficient	0.41311	mm^{-1}
Total Attenuation Coefficient	0.41483	mm^{-1}

*0.3% Lipofundin solution × (140×10^{15}/liter) = 0.42 sphere/micron^3

A.3.2 Fabrication of solid phantom

A.3.2.1 The recipe

In Hebden's recipe [26], 330g of resin and 99 g of hardener were mixed with 1.4 g of titanium dioxide and 0.5 ml of 2% ink. Similar recipe was used in this research.

The dose of TiO_2 was assumed to be 0.325% of the total amount of resin and hardener, which is the fraction of TiO_2 in the total weight of ingredients, less ink:

$$\frac{1.4}{330+99+1.4} = 0.325\%$$

The 2% ink was first prepared using 98ml of distilled water and 2ml of Pelikan 4001 ink. The dose of ink used was also assumed to be relative to the fraction of volume of ink used over the total weight of the epoxy resin in the above recipe. For example, fraction of ink used = volume of ink used / total weight of ingredients less ink:

$$\frac{0.5}{330+99+1.4} = 0.1162\%$$

In this study, the elementary recipe contains 10 g epoxy resin, 6 g hardener, 0.04 g TiO_2 and 0.02 ml 2% ink. The Petri dishes (molds) that are used require a total volume of about 40 g (25 g resin, 15 g hardener). Thus the actual doses of each ingredient are:

Dose of TiO_2

$$= 0.325\% \times (\text{Total amount of epoxy resin used})$$

$$= 0.325\% \times (25 + 15)$$

$$= 0.13 \text{ g}$$

Fraction for ink used remains 0.1162% as the amount of ink remains unchanged.

Dose of 2% ink

= 0.1162% × (Total amount of epoxy resin used)

= 0.1162% × (25 + 15)

= 0.047 ml

Therefore the doses of ingredients for making the optical phantom slabs (disc) are:

- 25g resin (Epicote 1006 System, Wee Tee Tong Chemicals Pte Ltd, SG)
- 15g hardener (Epicote 1006 System, Wee Tee Tong Chemicals Pte Ltd, SG)
- 0.13 g titanium dioxide
- 47 µl 2% ink (Pelikan 4001 ink)

A.3.2.2 Fabrication procedure

1) Mix appropriate amounts of resin, ink well in glass beaker.
2) Add appropriate amount of TiO_2 in glass beaker and mix well.
3) Degas mixture in vacuum desiccators and repeat 3-4 times.
4) Add in 50% of the required dose of hardener and mix well.
5) Add another 50% of the required dose of hardener; mix well.
6) Degas again in desiccators as before, taking note of the viscosity/texture.
7) Remove from desiccators before it gets hot/ starts to react.
8) Pour mixture slowly into container/mold.

9) Let cure in hood (room temp.) or oven (higher temp.).

10) When hardened, machine into slabs.

A.4 Mechanical drawings

A.4.1 Rotation stage

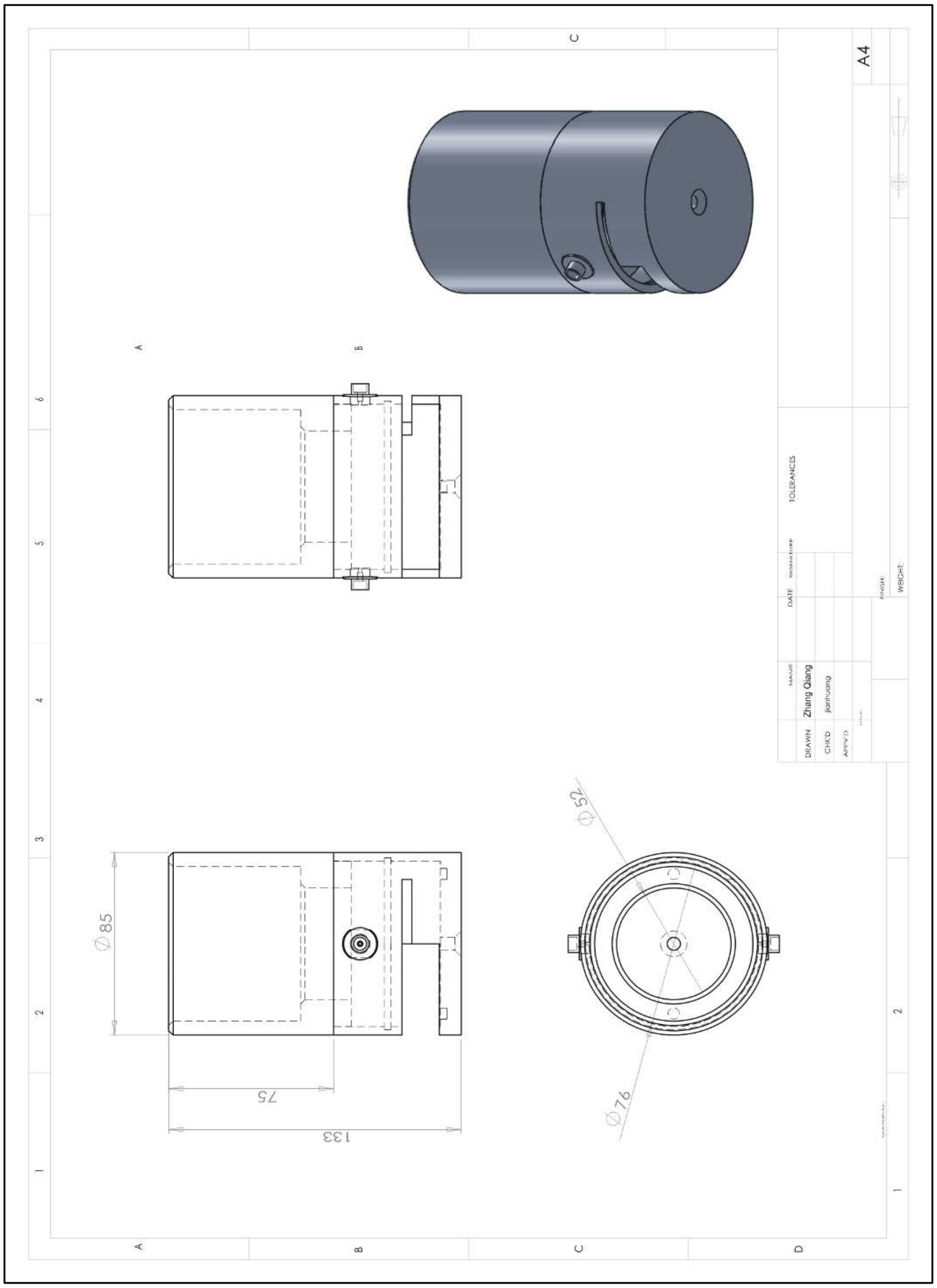

A.4.2 Finger holder

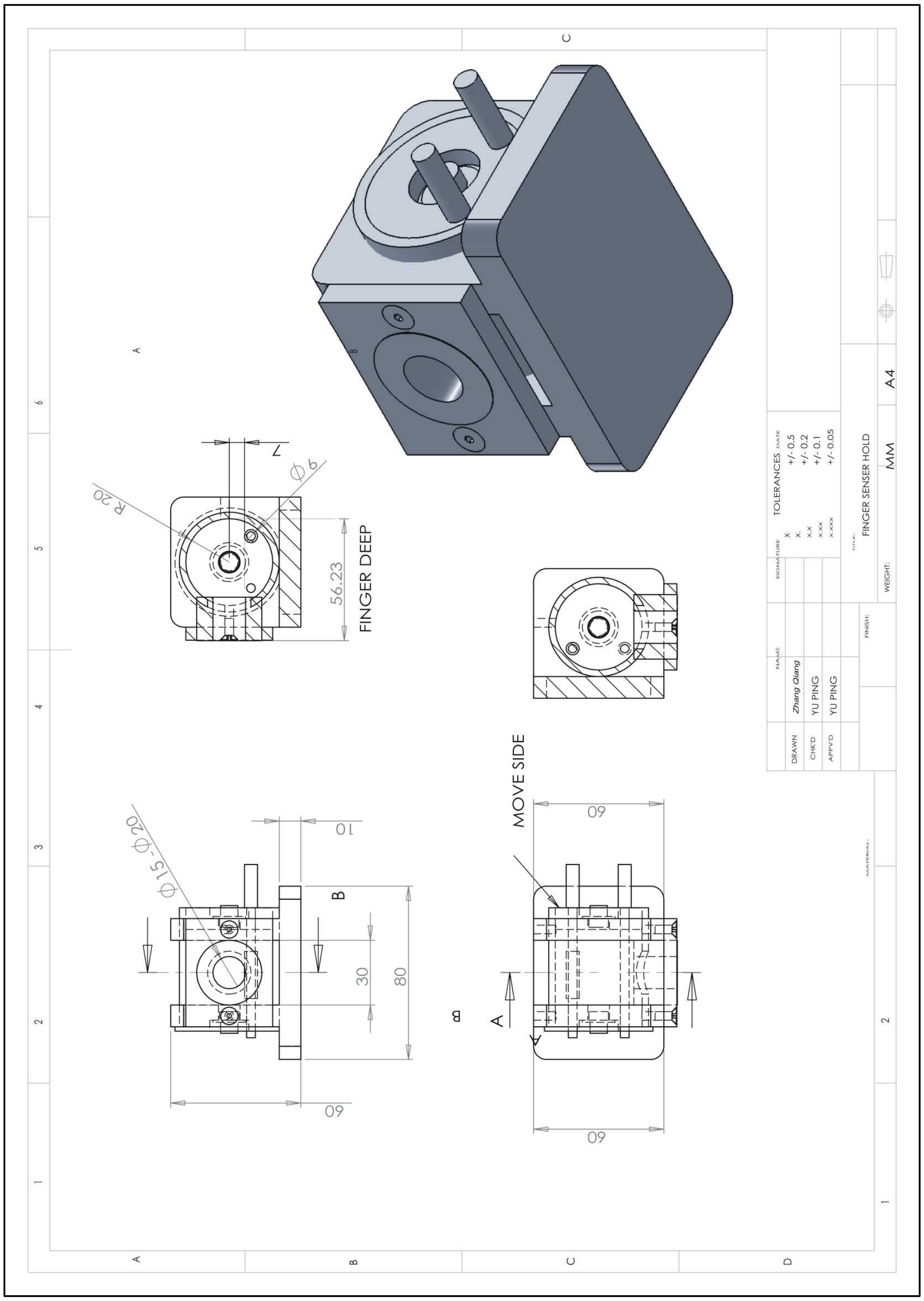

A.4.3 Pressure sensor (inside the finger holder)

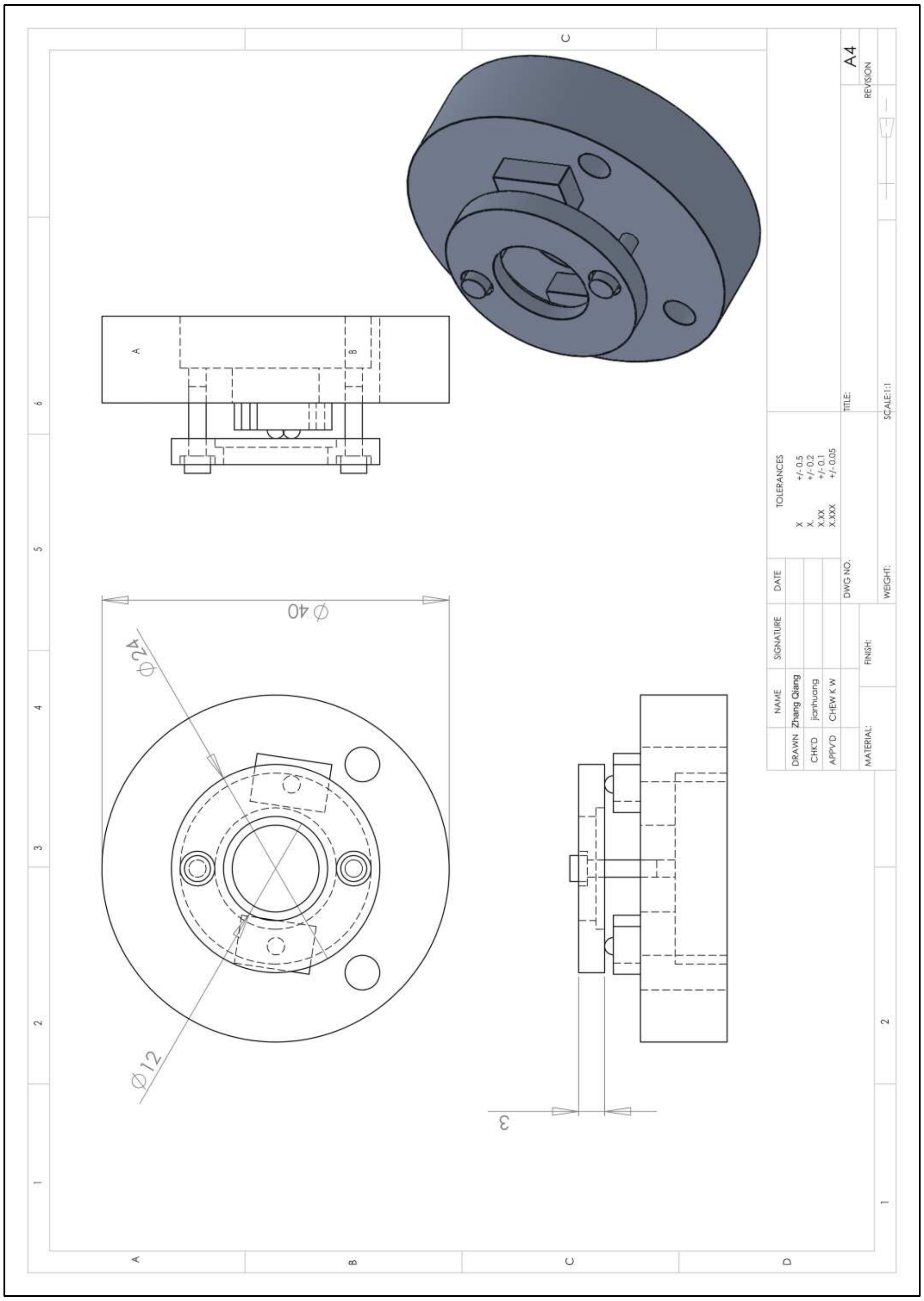

A.5 List of publications

Journal papers

[1]. **Q. Zhang**, H. W. Soon, H. T. Tian, S. D. Fernando, Y. Ha and N. Chen, “Pseudo Random Single Photon Counting for Time Resolved Optical Measurement,” Optics Express, **16** (17), 13233-13239 (2008).

[2]. H. T. Tian, F. Shakith, H. W. Soon, **Q. Zhang**, C. Zhang, Y. Ha and N. Chen, “Ultra Storage Efficient Time Digitizer for Pseudo Random Single Photon Counter Implemented on Field Programmable Gate Array,” IEEE Transactions on Biomedical Circuits and Systems, **4** (1), 1-10 (2010).

[3]. **Q. Zhang**, L. Chen and N. Chen, “Pseudo-random Single Photon Counting: A High-speed Implementation,” Biomedical Optics Express, **1**(1), 41 (2010).

Conference proceedings

[1]. **Q. Zhang** and N. Chen, “Pseudo-random single photon counting: the principle, simulation, and experimental results,” Proc. SPIE, **7170**, 71700L (2009), San Jose, U.S.A.

[2]. **Q. Zhang** and N. Chen, “High count rate pseudo-random single photon counting system for time-resolved diffuse optical imaging,” Proc. SPIE, **7556**, 755604 (2010), San Francisco, U.S.A. (oral presentation)

[3]. **Q. Zhang** and N. Chen, “Pseudo-random single-photon counting system: a high-speed implementation and its applications,” SPIE Photonics West, San Francisco, United States, Jan 2011 (oral presentation)

Abstracts

[1]. **Q. Zhang** and N. Chen, “Pseudo-random single photon counting: the principle, simulation, and experimental results,” European Conferences on Biomedical Optics, Munich, Germany, June 2009 (oral presentation)